UNDERSTANDING MULTI SCALE DEFECT FORMATION DURING SOLIDIFICATION OF ALLOYS BY INTEGRATED COMPUTATIONAL MODELING

by

Ghavam Azizi

A thesis submitted to the Faculty and the Board of Trustees of the Colorado School of Mines in partial fulfilment of the requirements for the degree of Doctor of Philosophy (Mechanical Engineering).

Golden, Colorado

Date_____

Signed: _____
Ghavam Azizi

Signed: _____
Dr. Mohsen Asle Zaeem
Thesis Advisor

Signed: _____
Dr. Brian Thomas
Thesis Co-Advisor

Golden, Colorado

Date_____

Signed: _____
Dr. Carl Frick
Professor and Department Head
Department of Mechanical Engineering

ABSTRACT

Solidification defects have a detrimental influence on mechanical and physical properties of metals and alloys. These defects can form in both macro and microscale inside the alloy or at the surface. In this Ph.D. research, by means of computational modeling, we aim to understand the formation mechanisms of surface defects that form during continuous casting of steels especially peritectic steels. To this end, we developed macro-scale computational framework based on finite element method to understand the effect of carbon on surface defect features of steels.

A finite element model including non-linear temperature-, phase-, and carbon-content-dependent elastic–viscoplastic constitutive equations is applied to study the effect of steel grade and interfacial heat flux on thermal distortion of a solidifying steel droplet. Due to thermal contraction, the bottom surface of the droplet bends away from the chill plate and a gap forms. It is shown that, regardless of the nature of the heat flux, the gap forms and grows the most very early during solidification (~0.1s) and remains almost unchanged afterward. The highest gap depths are predicted in ultra-low carbon (0.003%C) and peritectic steels (0.12%C), and agree both qualitatively and quantitatively with the experimental measurements. Thus, the current thermal-mechanical model, including its phase-dependent properties, captures the mechanism responsible for nonuniform solidification, depression sensitivity and surface defects affecting these steels. The findings of this fundamental model and gap formation mechanism have important implications for the formation of surface depressions and related defects in commercial steel continuous casting processes.

In this work we also investigated microsegregation and second phase formation mechanism in Al-Cu alloys with copper content ranging from 3 to 11 at% using a phase field model implemented in MICRESS program.

Our results show that the θ-phase fraction decreases with increasing the cooling rate, and this reduction is more drastic in alloys with a higher Cu content. Also, the microstructure features are influenced by the growth dynamics, where seaweed structure formation results in a more homogenous distribution of θ-phase and a finer microstructure. The results show that, irrespective of Cu content and cooling rate, the seaweed structure formation is halted at CM interfacial anisotropies larger than 0.005. As the anisotropy decreases, different seaweed structures can form regarding the constitutional supercooling. At low anisotropies (Al-3 and Al-8.4 at% Cu) and low supercooling (Al-3 at% Cu) fractal or degenerate seaweed is dominant while at high supercooling (Al-8.4 at% Cu) compact seaweed forms. This difference in supercooling stems from different solute atom transport rates. This is study is the first atomistic informed phase field simulation of pattern formation in Al-Cu alloys which is completely quantitative. The results of this study can be used for material selection and process design during solidification of Al-Cu alloys to control mechanical properties of solidified microstructure.

TABLE OF CONTENTS

LIST OF FIGURES

LIST OF TABLES

ACKNOWLEDGMENT

First, I would like to express my sincere gratitude to my advisors, Professor Mohsen Asle Zaeem and professor Brian Thomas, for allowing me to work with them and be part of their research groups. I am grateful for their patience, motivation, enthusiasm, immense knowledge, and continuous support of my Ph.D. study. their guidance helped me in all aspects of the research and writing of this thesis. I could not have imagined having a better advisors and mentors for my Ph.D. study.

In addition, I would like to thank the rest of my thesis committee: Prof. Amy Clarck, Prof. Cristian Ciobanu, and Prof. Craic Brice, for their encouragement, insightful comments, and challenging questions.

I thank my fellow lab mates in Computational Materials and Mechanics laboratory: Dr. Sepideh Kavousi, Dr. Hamed Nobarani, Amirreza Lotfolahpour, and William Huber, for scientific discussions, sharing knowledge, and for the sleepless nights working together before deadlines. Working with such dedicated and committed individuals made this journey fun and joyful.

Last but not least, I would like to thank my parents and my siblings for supporting me spiritually throughout all the ups and downs in my life.

CHAPTER 1

INTRODUCTION AND BACKGROUND

1.1 Solidification Defects

There is currently a great deal of interest in controlling all aspect of solidification characteristics include solidification microstructure and solidification defects. Controlling these features play a significant role in improvement of castability, improve mechanical and surface properties, and increase component integrity and reliability. Based on their scale solidification defects can be categorize in to main groups: macroscale and microscale defects. Macroscale defects include gas porosity formation [1], macro-segregation [2], shrinkage porosity (close shrinkage) [3], surface shrinkage (open shrinkage) [3], and macrocracks [4]. Microdefects include microcracks [5], micro-porosity [6] and microsegregation of alloying elements [7].

Macro-defects formation especially surface defects are one of the biggest concerns during continuous casting of steels which will be investigated in this study. Continuous casting technology is the primary method of producing semi-finished steel products, and over 96% of the world's steel is made using this process [8]. One of the most important features of continuously cast strands is their surface quality, which is mainly controlled by initial solidification at the meniscus [9-11]. In this region, the solidifying shell is subjected to complicated thermal and mechanical loading conditions [12] which may lead to formation of surface defects such as depressions [13], oscillation marks [14, 15], and cracks [16, 17].

Microsegregation which is the chemical inhomogeneity at the scale of a grain size or a dendrite arm, and is a result of non-equilibrium solidification of alloys is the main problem during solidification of Al-Cu alloys [18]. Solidification of hypoeutectic Al-Cu alloys leads to microstructures in which the α-dendrites are embedded into a eutectic interdendritic region of

α+Al_2Cu. Size and distribution of Al_2Cu particles have a crucial effect on mechanical properties of Al-Cu alloys [19]. The characteristics of this particles in a solidified microstructure are determined by solidification pattern [20].

In this study the underlying reason of surface defect formation during solidification of steels with a focus on the effect of carbon content will be investigated using finite element modeling and phase field modeling. Also, the effect of interfacial energy and its anisotropy on solidification pattern formation and eventually microsegregation in Al-Cu alloys will be investigated using phase field simulation.

1.2 Surface Shrinkage During Continuous Casting of Steels

The castability of high-quality steel depends on avoiding breakouts, cracks, and surface quality problems. The surface quality of steel products is mainly determined by the early stages of solidification in the meniscus region of the mold and steels which undergo the peritectic transition are the most difficult to cast [21-23]. This is attributed to the volume contraction (shrinkage) associated with the peritectic phase transformation. This shrinkage leads to the formation of deep air gap and oscillation marks, surface crack formation and large austenite grain size [24-27]. The automotive industry is increasingly utilizing steels with peritectic composition range (AHSS, HSLA etc.), to reduce vehicle weight. Therefore, there is a great need to produce these steels without defects [28].

Peritectic steel solidification occurs in two distinct stages: the peritectic reaction (L+ δ→γ) followed by the peritectic transformation (δ→γ), Figure 1.1 (a). During the peritectic reaction, an austenite layer grows along the L+δ interface, as pictured in the upper right frame of Figure 1.1 (b). After the liquid locally runs out, then the remaining δ-ferrite transforms to

austenite by solid state transformation. The peritectic transformation starts by thickening of the austenite (b) [29].

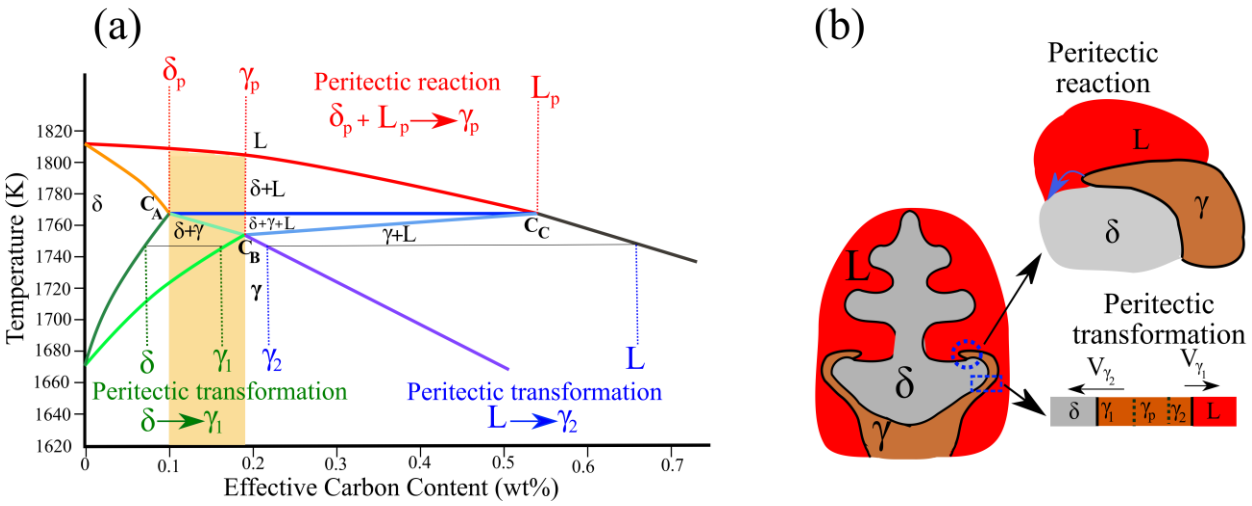

Figure 1.1. (a) Iron-carbon phase diagram showing peritectic steels (shaded) and their phase transformations; (b) schematics of the peritectic reaction and subsequent peritectic transformation.

1.2.1 Mechanism of Peritectic Solidification

Peritectic solidification has been investigated by many researchers [30-37] and different mechanisms have been proposed to explain the details of this phenomenon. These include thermal diffusion of solute atoms [35] and re-melting of delta ferrite [38] to explain the peritectic reaction and diffusion or massive transformation to explain the peritectic transformation [36, 37, 39-41]. Many models [30-33] assume that the peritectic reaction and transformation are both controlled by the diffusion of solute atoms. Some measurements, by diffusion-couple [34] and directional solidification experiments [40], agree with these diffusion-controlled models. However, other experimental studies [35, 38, 39, 41-43] have shown that the rates of the peritectic reaction and transformation are very fast, especially γ -austenite layer

growth along the liquid/δ -ferrite interface in the peritectic reaction. Recent phase field simulations suggest that these high rates can be explained by diffusion [44-46]. Other researchers claim that these observations cannot be explained by diffusion mechanism(s) alone, and have suggested other mechanisms, including micro-scale heat transfer and fluid mixing involving delta-ferrite re-melting [35, 38, 41], and massive transformation [38, 47-51].

1.2.2 Effects of Peritectic Solidification

Understanding peritectic solidification in steels is of great practical importance, because peritectic solidification causes many different problems during commercial casting processes such as continuous casting. These problems include the formation of deep oscillation marks, surface depressions and interfacial gaps in the mold that lead to lower heat flux, thinner, and nonuniform (rippled) solidified shell thickness and accompanying catastrophic breakouts, increased susceptibility to surface crack formation, and larger austenite grain size. During casting of steel, heat flux from the solidifying steel to the mold is a strong function of carbon content [21, 52], where the lowest heat transfer rate is measured for the peritectic 0.10 pct C steel.

The shell of the peritectic steel is thinner, as seen in the measurements in Figure 1.2 (a). This slower shell growth of peritectic steels is caused by the generally lower mold heat transfer.

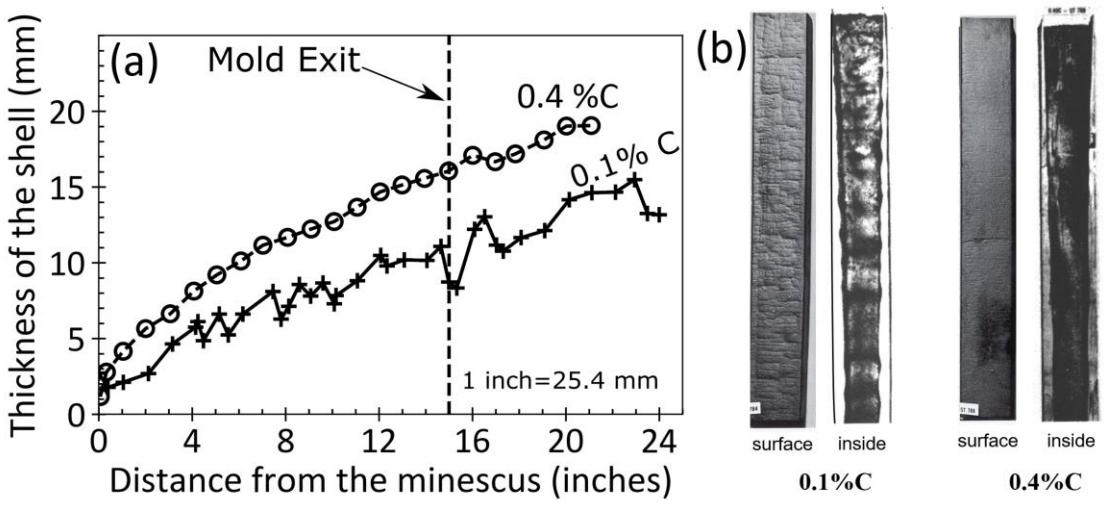

Figure 1.2. Steel shell growth profiles during continuous casting, comparing peritectic and non-peritectic steel grades, (b) Surface and cross section views of solidified shells of continuous-cast steel billets of peritectic steel and and non-peritectic steel grades [21].

More important than the thinner shell, however, is the jagged nature of the shell thickness profile for the peritectic steel, which indicates the much larger variability in shell growth of this steel grade. Figure 1.2 (b) compares the appearance of the surface and interior of peritectic and non-peritectic steels [21]. While non-peritectic (0.4 pct C) steels solidify with a relatively smooth interior, the peritectic steel (0.1 pct C) experiences severe ripples on the inside of the shell.

The root cause of the shrinkage peak in peritectic steels is the $\delta \rightarrow \gamma$ transformation from body-centered-cubic δ to face-centered-cubic γ, which decreases the molar volume by 2.5 - 3.0 pct [53]. Shrinkage calculations of a solidifying steel shell, such as given in Figure 1.3 shows that linear shrinkage increases with time for all steel grades [54].

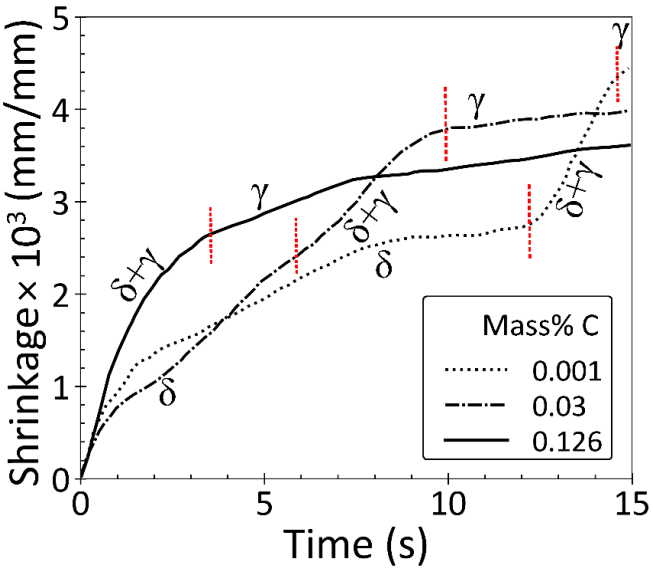

Figure 1.3. Calculated shrinkage of solidifying shell vs. time from the start of casting [24].

Peritectic solidification also is detrimental for high and medium temperature ductility. Metallurgical properties during solidification are shown schematically in Figure 1.4. Above the Zero Strength Temperature, (ZST), the steel behaves like liquid, and any applied tensile strain will simply pull apart the dendrites, and draw liquid in to fill the space. Between LIT and ZDT is a brittle temperature range that is susceptible to hot tearing [55]. In the critical temperature ranges, any applied tensile strain will open up a crack, which is filled by drawing in surrounding segregated liquid. In peritectic steels the δ→γ transformation takes place in brittle temperature range and consequently decreases hot ductility.

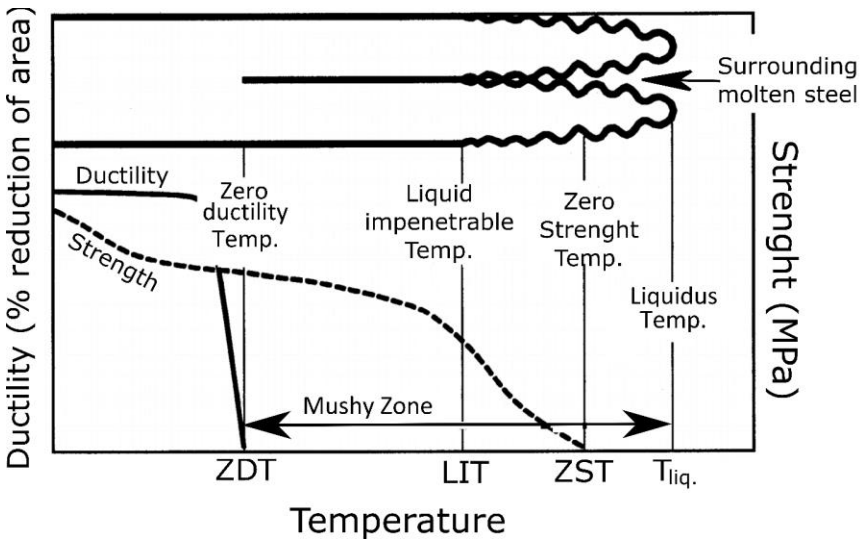

Figure 1.4. Schematic of temperatures relevant to high-temperature embrittlement and hot tearing cracks during steel solidification. Reprinted with permission from reference [55].

1.3 Microsegregation In Al-Cu Alloys: Solidification Pattern Effect

Microsegregation is defined as a chemical separation and concentration of alloying elements or impurities on small scales. Microsegregation develops as solute is rejected and trapped among microstructural elements formed by unstable interfaces, such as cells and dendrites. For example, the primary stem of a dendrite may be relatively low in solute compared to nearby interdendritic regions surrounded by the side branches that were the last to solidify. Microsegregation arises from the partitioning of solute between solid and liquid which is expressed by the equilibrium partition coefficient for the solute, $k=C_s/C_L$. where C_s and C_L are the solute concentrations in solid and liquid respectively. Under equilibrium solidification conditions where diffusion in solid and liquid is complete, the composition of both solid and liquid adjusts during cooling in accordance with the phase diagram so that the final solid has the composition of the original melt, and no microsegregation has developed. Under real conditions, diffusion in the solid is restricted, and the alloy after completion of solidification is

inhomogeneous in composition. In alloys which are nominally single phase, microsegregation can lead eventually to the precipitation of second phase from the solute-enriched liquid. A coarse second phase and the inhomogeneous microstructure arising from microsegregation, even after heat treatment, will result in poor mechanical properties, and particularly in reduced ductility.

In the assessment of the amount of microsegregation which occur during solidification, the morphology and scale of the dendrite structure are of crucial importance since they strongly influence the extent of solute diffusion. In other word, patterns created by the dendritic structure influence the distribution of secondary phases that form in the interdendritic regions in the late stages of solidification. Solidification pattern is controlled by processing condition (cooling rate and temperature gradient) and material properties (freezing range, diffusion coefficient, Crystal - melt (CM) interfacial energy and its anisotropy, etc.).

The crystal-melt (CM) interfacial energy is an intrinsic material property that plays a critical role in solidification pattern formation [56]. It influences the solidification microstructures in two ways; first, dendrites grow during solidification along the directions with the highest CM interfacial energy, and second, the instability of interface affecting the dendrite patterns, is controlled by the CM interfacial energy [57-59]. The CM interface energy has an anisotropic nature with respect to the crystallographic directions. Despite the unknown atomistic origin of interfacial energy anisotropy, the anisotropy is very small for most alloys which results in a negligible change in the interfacial energy in different crystallographic directions [56]. However, it governs the nucleation and growth kinetics [60-62], morphology [63-65], and crystallographic growth direction of the dendrites [66].

The instability of CM interface, which is influenced by the CM interfacial energy, controls microstructure evolution, dendrite arm spacing, and microsegregation patterns [58]. Coriell and

Sekerka [67] added surface tension and surface kinetic anisotropy effects into the perturbation linear stability analysis and showed that the capillary term, that contributes in interface stability, is direction dependent [64, 68, 69]. Trivedi [70] compared experimental results with linear and weakly nonlinear analyses of the planar interface stability and showed that when a material is directionally solidified beyond the threshold of planar stability condition [71], the anisotropy of interface properties not only affects the planar to cellular and cellular to dendritic transitions, but also causes tilting of cells and dendrites against the heat flow direction [72-74].

Besides dendritic microstructures, diverse types of morphologies can be formed during solidification of metallic alloys, including seaweed, dense-branched, fractal-like, and variations between these patterns [75-79]. These morphologies may result from interactive effects of thermal diffusion, mass diffusion, and inherent interfacial anisotropy on interface stability [77, 80, 81]. Experimental work performed by Akamatsu et al. on transparent alloys [77, 81] showed that the stability of dendritic patterns greatly depends on the strength of interfacial energy anisotropy. They proved that for crystal orientations corresponding to low interfacial anisotropy, dendritic pattern is unstable and seaweed structure forms. Numerical studies [76, 82] confirmed these results and proved sidebranching takes place for vanishing anisotropy which results in seaweed structure formation. Recent phase-field simulations show occurrence of transitions between solidification patterns by changing the chemical compositions and processing conditions. Amoorezaei et al. [83] showed that in a directionally solidified Mg alloy with low interfacial energy anisotropy, any change in processing condition considerably alters the solidification morphology. Their results indicated that at a low pulling velocity, seaweed structure is dominant, while at an increasing pulling velocity compacted seaweed is the main morphology. In another study, Xing et al. [84] investigated the dynamics of growing dendrites

and showed that the seaweed is the dominant morphology at weaker interfacial energy anisotropies, lower pulling velocities, and higher thermal gradients. It is believed that the instability at the tips, which stems from low surface energy anisotropy, is responsible for the formation of such a morphology [85, 86]. Chen et al. [87] showed that tip splitting takes place during the solidification of Al-4 wt% Cu with low interfacial energy anisotropy, which leads to seaweed structure. They argued that the seaweed regime is formed by morphological instability occurring when the cell/dendrite tip becomes too wide.

Despite their importance in predicting the microstructure, experimental measurements of the CM interfacial free energy and the anisotropy terms are very challenging and often not possible [88]. Because of the recent availability of reliable embedded interatomic potentials for metals, molecular dynamics (MD) has become a popular method for calculating the CM interface free energy. Among the two well-known methods, namely Cleavage [89] and the capillary fluctuation method (CFM) [90], the latter results in a more accurate anisotropy parameter calculations, which is used in this study. CFM has been extensively used for interface energy calculations of metals [91-96], compounds [97], and binary alloys [98, 99].

The interface energy for an alloy depends on the working temperature and alloy composition. There are different MD simulations that discuss how the change in chemical composition alters the interface free energy and its anisotropy. Becker et al. [100] used CFM to show that the CM interface energy in Ni-5at%Cu alloy is 7.4% less than pure Ni. Furthermore, the addition of 5 at% Cu decreases δ_1 (Fourfold anisotropy parameter) from 0.09 to 0.072 and increases δ_2 (Six-fold anisotropy parameter) from -0.011 to -0.007 [101]. Potter and Hoyt [102] applied the CFM to the Cu-rich Cu–Ag–Au system; they indicated that species with a high

enthalpy of mixing tend to destabilize the dendrites growing in the ⟨100⟩ direction and promote a transition to the growth of hyper-branched and ⟨110⟩ –oriented dendrites.

Some studies support the computationally-predicted change in the interface free energy and the corresponding anisotropy due to the change in alloy composition. Using experimental observation [103] and phase-field modeling [104], it was shown that in Al-Zn alloys (Zn<25 wt%) with high values of ϵ_1 (four-fold anisotropy parameter) and low values of $|\epsilon_2|$ (six-fold anisotropy parameter), ⟨100⟩-oriented dendrites are dominant. When Zn concentration is more than 55 wt%, the value of ϵ_1 is low and the absolute value of ϵ_2 is high. Under this condition, ⟨110⟩ is found to be the favorable growth direction. In the intermediate regions, surface energy anisotropy becomes very small and leads to the formation of seaweed structures or hyper-branched dendrites [105]. The same behavior was observed in Al-Ge system, where at Ge less than 20 wt% dendrite grows along ⟨100⟩ direction, and when Ge is more than 46 wt%, ⟨110⟩ is dominant growth direction [106]. Recently, Wang et al. [56] showed that in Al-Sm alloy system, increasing Sm content drastically reduces anisotropy strength while increasing the average interface energy (γ_0). The aforementioned studies indicate that chemical composition is the main factor that controls CM interfacial energy and its anisotropy. Also, it was shown that since the equilibrium composition at CM interface changes by temperature, its energy and anisotropy are functions of temperature [107-109].

In this thesis we will investigated multi scale defect formation in Fe-C and Al-Cu alloys using finite element modeling and phase field modeling, respectively. In Chapter 2, we represent a review of proposed mechanisms for peritectic solidification mechanisms and the effect of peritectic solidification on the defect formation during steel casting. In Chapter 3, we use a finite element modeling to simulate thermal distortion and air gap formation at the surface of a

solidifying steel droplet. In Chapter 4, using an atomistic informed phase field modeling we investigate solidification pattern formation and microsegregation in Al-Cu alloys. The last two chapters are the conclusions of this study and potential future works.

1.4 Objectives

Formation of defects in both macro and micro scale during solidification of alloys is detrimental to mechanical and physical properties. Steels and Al-Cu are among the alloys with highest demand and it is crucial to produce them without defects.

During solidification of steels surface defects form due to phase transformation of ferrite to austenite at early stage of solidification. The questions are how the steel grade with different carbon content can change the surface defect characteristics and what is the underlying mechanisms. Also, it is crucial to know how the heat flux change defect formation in different grades.

In Al-Cu alloys the size and distribution of the intermetallic phase (Al_2Cu or θ-phase) which forms in the interdendritic regions has a great effect on mechanical properties. The characteristics of θ-phase is mainly controlled by the solidification pattern which form during solidification. The questions are 1- how Cu content results in change of solidification pattern. Is Cu content the only parameter that change or it has effect on solid/liquid interfacial energy and its anisotropy. How interfacial energy properties interact with solute consternation to change solidification pattern. Which patterns results in more homogenous distribution of θ-phase.

Considering aforementioned questions, the objectives of this thesis are as follow:

1- proposed mechanisms of peritectic solidification are reviewed in detail and the effects of peritectic solidification on surface quality, austenite grain size, hot ductility, segregation, and crack formation of cast product is discussed.

2- During continuous casting of steels many transient phenomena take place in the mold and have effect on distortion of solidifying shell. Due to this condition it is almost impossible to single out the effect of phase transformation shrinkage on shell distortion. To this end, a finite element model including non-linear temperature-, phase-, and carbon-content-dependent elastic–viscoplastic constitutive equations to study the effect of steel grade and interfacial heat flux on shrinkage and thermal distortion of a solidifying steel droplet.

3- Performing an atomistic-informed phase-field study to investigate the microstructure evolution during solidification of Al-Cu binary alloys under different solidification conditions. First, MD simulations are performed to reveal the relationship between CM interfacial energy properties and Cu content. Subsequently, a multi-phase field model is utilized to explore how Cu concentration gradient ahead of growing dendrite (G_c) and CM interfacial anisotropy collaborate to generate different solidification patterns and consequently different solidification features, such as dendrite arm spacings, and θ-phase fraction and distribution.

CHAPTER 2
REVIEWOF PERITECTIC SOLIDIFICATION MECHANISMS AND EFFECTS IN STEEL CASTING

2.1 Abstract

Surface quality and castability of steels is controlled greatly by initial solidification. Peritectic steels suffer more from surface quality problems, including deep oscillation marks and depressions, crack formation and breakouts than other steels. This paper reviews current understanding of the fundamental mechanisms of initial solidification of peritectic steels that lead to these problems. First, different empirical relations to identify peritectic steel grades from their alloy compositions are summarized. Peritectic steels have equivalent carbon content that takes their solidification and cooling path between the point of maximum solubility in δ-ferrite and the triple point at the peritectic temperature. Surface defects are related more to the solid state peritectic transformation (δ-ferrite→γ-austenite) which occurs after the peritectic reaction (L+ δ→γ) during initial solidification. Some researchers believe that the peritectic reaction is controlled by diffusion of solute atoms from γ phase, through the liquid, to the δ phase while others believe that γ growth along the L/ δ interface involves microscale heat transfer and solute mixing due to local re-melting of δ-ferrite. There is also disagreement regarding the peritectic transformation. Some believe that peritectic transformation is diffusion controlled while others believe that massive transformation is responsible for this phenomenon. Alloying elements and cooling rate greatly affect these mechanisms.

2.2 Introduction

The castability of high-quality steel depends on avoiding breakouts, cracks, and surface quality problems. The surface quality of steel products is mainly determined by the early stages of solidification in the meniscus region of the mold [9, 11, 110-115]. Steels which undergo the

peritectic transition are the most difficult to cast [11, 116-121]. This is attributed to the volume contraction (shrinkage) associated with the peritectic phase transformation [24, 122, 123]. This shrinkage leads to the formation of an air gap between the steel shell and the mold during the CC process and decreases the heat flux. This leads to locally thinner and hotter regions of the solidified shell, which causes uneven shell growth that leads to surface depressions, deep oscillation marks, cracks, and breakouts [26, 124-129].

Steels within the peritectic composition range include High Strength Low Alloy (HSLA) Steels, and recently Advanced High Strength Steels (AHSS), which are all used extensively in different products due to their excellent mechanical properties, which include high strength and toughness [28, 130-132]. The automotive industry is increasingly utilizing steels with peritectic composition range (AHSS, HSLA etc.), to reduce vehicle weight. Peritectic steels are widely applied in pipelines, navy vessels and nuclear power plant components [132, 133]. Therefore, there is a great need to produce these steels without defects [28].

Peritectic steel solidification occurs in two distinct stages involving liquid (L), delta-ferrite (δ) and austenite (γ): the peritectic *reaction* (L+ δ→γ) followed by the peritectic *transformation* (δ→γ) [33, 38, 39, 134]. The peritectic reaction occurs just below the peritectic temperature, when liquid and delta-ferrite are in contact and react to form austenite. This corresponds to the L+δ+γ three-phase point in the binary phase diagram [135], or to the 3-phase region on sections through a multi-component phase diagram, such as shown in Figure 2.1(a). During the peritectic reaction, an austenite layer grows along the L+δ interface, as pictured in the upper right frame of Figure 2.1(b). After the liquid locally runs out, then the remaining δ-ferrite transforms to austenite by solid state transformation. The peritectic transformation starts by thickening of the austenite layer immediately behind the tip of this advancing γ platelet, as shown in Figure 2.1(b)

[29], where it proceeds on two fronts, growing into both the liquid on one side of the platelet and the delta interior on the other. Later, towards the center of the dendrite, the interior δ-γ interface has moved far away from the liquid, so further austenite growth into the delta ferrite involves only a single moving interface. Note that spatially, these different steps of peritectic solidification occur at different places, and proceed in different directions relative to the thermal gradient, which is oriented downwards in Figure 2.1(b).

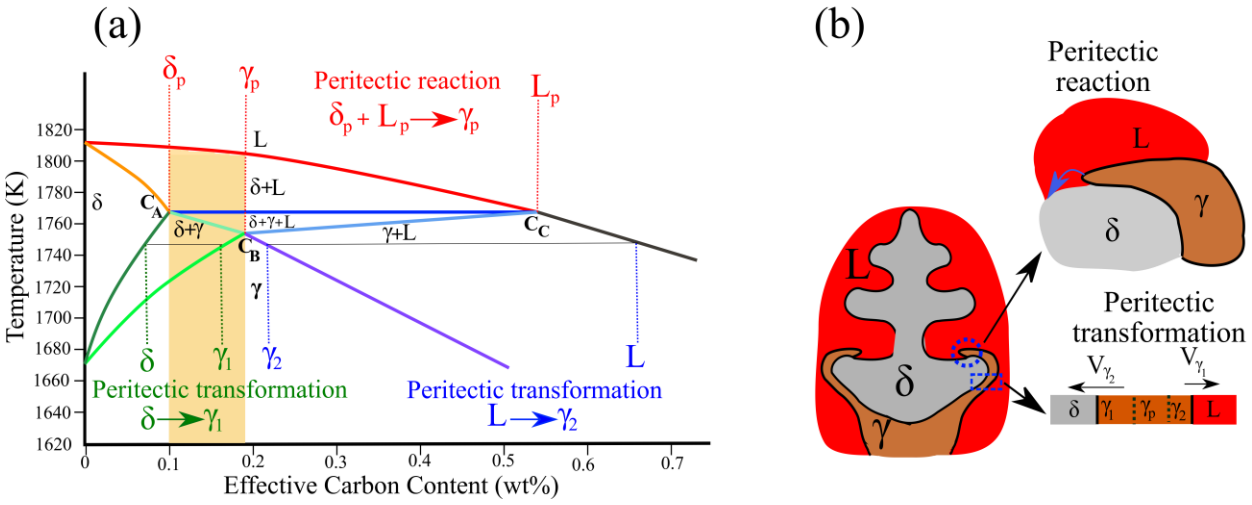

Figure 2.1. (a) Iron-carbon phase diagram showing peritectic steels (shaded) and their phase transformations; (b) schematics of the peritectic reaction and subsequent peritectic transformation.

In this paper, the proposed mechanisms of peritectic solidification are reviewed in detail and then the effects of peritectic solidification on surface quality, austenite grain size, hot ductility, segregation, and crack formation of cast product is discussed. But first, the different calculations used to identify peritectic steel grades from their compositions are summarized.

2.3 Identification of Peritectic Steels

As casting of peritectic steels is difficult, it is important to identify a peritectic steel from its composition. If a new grade of steel is predicted to be a peritectic, then appropriate actions can be taken at the caster, such as applying appropriate mold powders with high solidification temperature to lower the surface cooling rate [136-138], and / or casting at a lower speed [117] Low-alloy commercial steels can be characterized by their carbon content, with corrections according to the other alloying elements. Predicting the occurrence of the problematic peritectic transformation in high-alloy steels is more difficult, and involves the relative amounts of more than one other elements , (such as carbon, nickel, and chromium in stainless steels [139], or in AHSS [140, 141].)

In the Fe - C phase diagram for low-alloy steels, shown in Figure 2.1, four different solidification behaviors can be categorized according to their effective carbon content. These include range I, for effective carbon content less than point C_A, range II for carbon between C_A and C_B, range III for carbon between C_B and C_C, and range IV, for carbon above C_C. Steels in range II are known as peritectic steels and are the most difficult to cast because they experience transformation from δ to γ that coincides with the final stage of solidification. While in range I, δ to γ transformation starts and ends in the solid state. In range III, the transformation occurs in the presence of liquid and in range IV, the steel solidifies as austenite so the δ to γ transformation does not take place at all and there is no contraction.

The position of points C_A, C_B and C_C in the pseudo-binary phase diagram of Fe and effective carbon content have been defined in different ways in previous research. When carbon is the only significant alloying element, Point C_A is given between 0.088 wt. pct C* to 0.1 pct C point C_B ranges from 0.16 pct C to 0.18 pct C [141-143] and C_C is about 0.53 pct C [142]. The

position and temperature of points C_A, C_B and C_C change significantly according to the alloy content, however. Alloying elements change the effective carbon content, and are classified as either ferrite formers, which tend to shift the points to the right (higher carbon) or austenite formers, which have the opposite effect. Increasing alloy content also extends the ternary (L+ δ + γ) phase region in Figure 2.1 Different experiments [141, 144-148] have been conducted to determine if a steel exhibits peritectic behavior, and different empirical equations [149-154] have been proposed to predict this, as discussed in the next sections.*

2.3.1 Experimental Measurements

Differential scanning calorimeter (DSC) measurements can identify the temperatures of phase transformations in steels [155-160], based on detecting the accompanying small changes in enthalpy. This includes the ability to identify peritectic steel grades from the distinctive second peak in their enthalpy rate – temperature profile during cooling [145, 147, 148, 161]. Confocal microscopy, discussed in Section III can augment the DSC measurements by visualizing these phase transformations [161]. The ultimate test is behavior in the commercial caster, where peritectic steels experience more variations and defects than other steels, as discussed in Section IV.

All alloys show a large peak in the DSC curves at high temperature during the phase transformation between the molten steel and either delta-ferrite or austenite [145]. The peritectic reaction, when present, generates a significant second peak, at the lower "peritectic temperature" [145, 161] because it involves austenite forming at the expense of liquid, in addition to delta ferrite. This second peak may not appear in DSC cooling curves, however, if the cooling rate is

* All alloy compositions in this paper are given in weight pct

too high, for reasons discussed later [145, 161]. The solid-state transformation from delta ferrite to austenite has a small third peak [145, 161]. which is often difficult to detect.

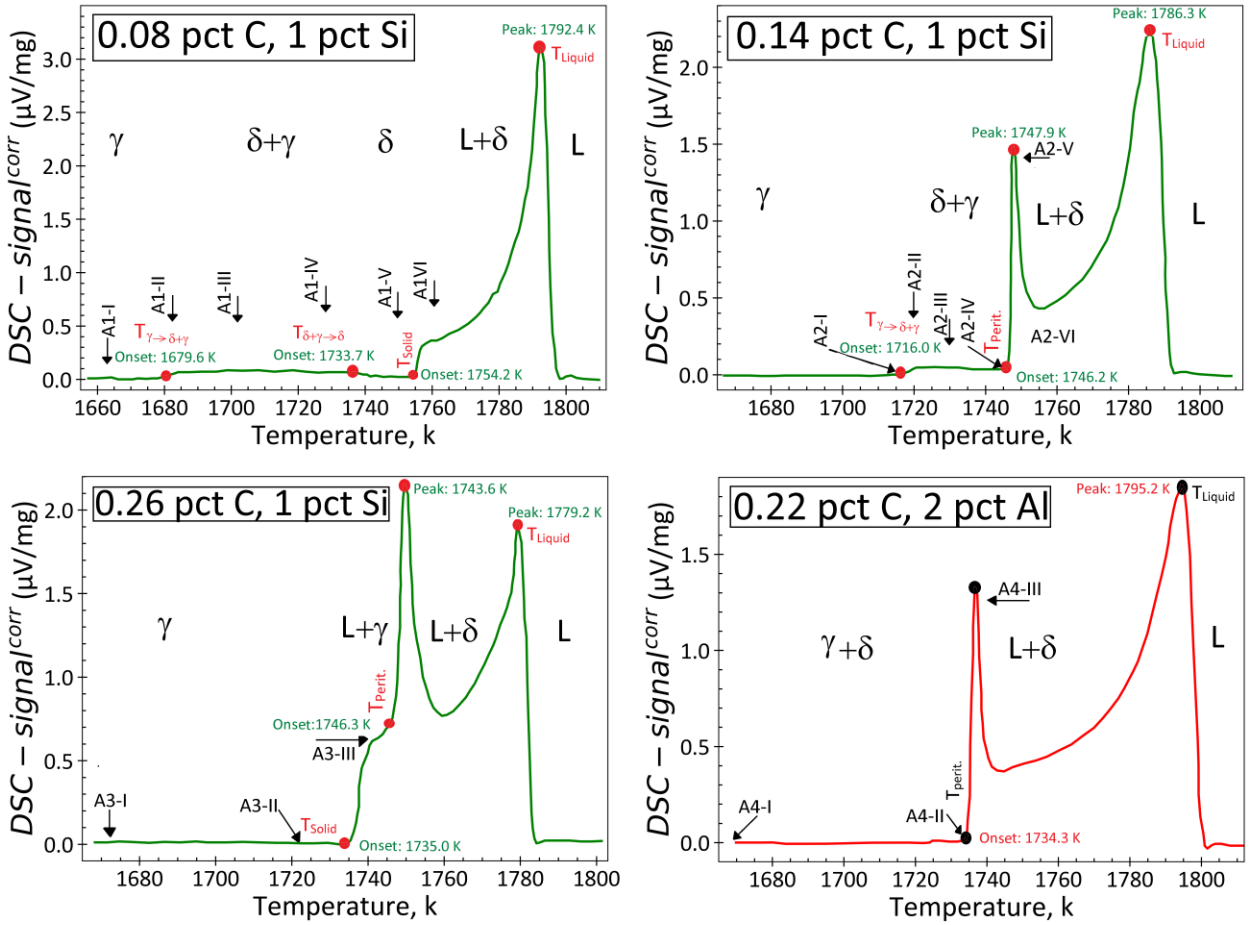

Figure 2.2. The DSC measurement of different steel grades. Reprinted with permission from reference [141].

As an example, Figure 2.2 shows typical DSC results for four steels [141], which are supported by high-temperature confocal laser scanning microscopy (HT-CLSM) observations. Figure 2.2 shows one heating curve for a typical non-peritectic steel, (top left frame with 0.08 pctC), so there is no significant enthalpy peak before melting. The other 3 frames in Figure 2.2

all show a second large, sharp peak due to the peritectic reaction, indicating that these are all peritectic steels. This includes a new advanced high-strength steel, (lower right frame with 2 pctAl), which is not correctly identified as being peritectic by current models, which are discussed in the next section.

2.3.2 Calculation Methods

Several different methodologies have been proposed to predict if a steel is a peritectic, based on its exhibiting adverse solidification behavior, such as susceptibility to depressions and cracks. These methods include empirical equations based on an equivalent carbon content range, alloy-dependent critical points, ferrite potential, and CALculation of PHAse Diagrams (CALPHD) methods. These are discussed in turn below.

2.3.3 Carbon Equivalent Range Method

Several different models have been proposed to predict if a steel exhibits peritectic behavior based on calculating the carbon equivalent (C_P) of the steel alloy. If the calculated carbon equivalent is between a critical range, such as falling between C_A= 0.09 pct C and C_B= 0.17 pct C (peritectic region in Figure 2.1) then the steel is considered to be peritectic and its sensitivity to depressions and cracks is high. Wolf [151] proposed the following equation for carbon equivalent.

$$C_P = [C] + 0.02[Mn] + 0.04[Ni] – 0.1[Si] – 0.04[Cr] – 0.1[Mo] \quad (2.1)$$

where brackets contain weight percent of alloying elements. Howe [162] proposed the following alternative.

$$C_P = [C] + 0.04[Mn] + 0.1[Ni] + 0.7[N] – 0.14[Si] – 0.04[Cr] – 0.1[Mo] – 0.24[Ti] \quad (2.2)$$

Xia et al [149] suggests the following equation for calculation of carbon equivalent.

$$C_P = [C] + 0.02[Mn] – 0.037[Si] + 0.023[Ni] – 0.0189[Mo] – 0.7[S] + 0.0414[P] + 0.003[Cu] – 0.0254[Cr] – 0.0267[Ti] + 0.7[N] \quad (2.3)$$

Normanton and other researchers at Trico Steel and British Steel [163] proposed two more equations for the calculation of carbon equivalent [163],

$$C_P = [C] + 0.01[Mn] + 0.009[Si] + 0.02[Ni] + 0.003[Cr] – 0.007\ [Mo] + 0.009\ [V] + 0.008[P] + 0.147[S] + 0.5[N] + 0.007[Cu] + 0.007[Ti] + 0.05\ [Al] + 0.04\ [Nb] \quad (2.4)$$

$$C_P = [C] + 0.043[Mn] – 0.14[Si] + 0.1[Ni] – 0.083[Cr] – 0.063\ [Mo] – 0.13\ [V] + 0.029[P] + 0.11[S] + 1.06[N] + 0.037[Cu] – 0.024[Ti] \quad (2.5)$$

As can be seen in Eqs. 1-5, the equivalent weight concentrations of austenite-forming elements (Mn, Ni, Cu, and N) are added to the C content and the ferrite-forming element Mo is subtracted, as expected. The elements P, Al, and Nb are ferrite-forming elements [164], yet their terms are added to the C content in several equations. The effects of Si, Cr, Ti, V, and S are not consistent between equations.

2.3.4 Alloy Dependent Critical Points Method

Blazek et al [165] proposed a different method, defining a steel as peritectic when its carbon content is between C_A and C_B, which change with alloy composition as follows:

$$C_A = 0.0896 + (0.0458 \times Al) – (0.0205 \times Mn) – (0.0077\times Si) + (0.0223 \times Al^2) – (0.0239\times Ni) + (0.0106 \times Mo) + (0.0134\times V) – (0.0032\times Cr) + (0.00059\times Cr^2) + (0.0197 \times W) \quad (2.6)$$

$$C_B = 0.1967 + (0.0036\times Al) - (0.0316\times Mn) - (0.0103\times Si) + (0.1411\times (Al)^2) + (0.05\times (Al\times Si)) – (0.0401\times Ni) + (0.03255\times Mo) + (0.0603\times V) + (0.0024\times Cr) + (0.00142\times(Cr^2) – (0.00059\times (Cr\times Ni)) + (0.0266\times W) \quad (2.7)$$

This relation, which was based on thermodynamic calculations with Thermocalc [166] is reported to be accurate for many steel grades [165], and has successfully been implemented into several steel plants to enable appropriate choice of mold powder and casting practice [165].

However, this relation may be inaccurate for steels with high Si content. The sign of the Si term in the effective carbon equations is negative (shift C_A to the left), which may be opposite to expectations, so this term is controversial. Other studies [152] have confirmed that increasing Mn shifts the peritectic range to the left and agree with Blazek [165] that Al shifts the peritectic range to the right. Those studies also found that S shifts the peritectic range to the left and P shifts it to the right [152]. Clearly, there is still some disagreement regarding the effects of several elements on peritectic formation.

2.3.5 Ferrite Potential

Wolf introduced the term, "ferrite potential" as a measure of the extent of peritectic behavior experienced with a given steel alloy [151]. "Ferrite potential" is also defined as the solid fraction of primary ferrite during solidification. Using the ferrite potential concept, steels can be categorized into depression-sensitive and sticker-sensitive grades. Peritectic steels are depression sensitive, owing to their greater shrinkage, and tend to suffer from deep oscillation marks and uneven shell growth, leading to surface cracks and other defects, as discussed in Section IV. Non-peritectic steels are more sticker-sensitive, tending to stick to the mold walls, which leads to a higher risk of sticker breakouts [167-169]. Although the ferrite potential is affected most by the carbon content, it is also affected by other alloying elements [151]. Some elements stabilize the austenite (Ni, Mn, Co, N and Cu) while others are believed to stabilize the ferrite (Cr, W, Mo, Al and Si)[164]. For low-alloy steels, the ferrite potential (FP) can be calculated as follow [151]:

$$FP = 1.25 - 2.5 \times [C_P] \quad (2.8)$$

Here C_P is carbon equivalent and is calculated using Eq. 2.1, where $0<FP<1$, indicates that the peritectic reaction takes place during solidification. When FP is in the range of 0.85–1.05

(peritectic behavior range), the tendency for depressions, crack formation and uneven shell growth is high. Steels in this range are depression-sensitive grades (steel type A) and steels outside this range (FP < 0.85 or FP > 1.05) are sticker-sensitive grades (steel type B) [151]. The effect of ferrite potential on the tendency of depression formation is shown in Figure 2.3.

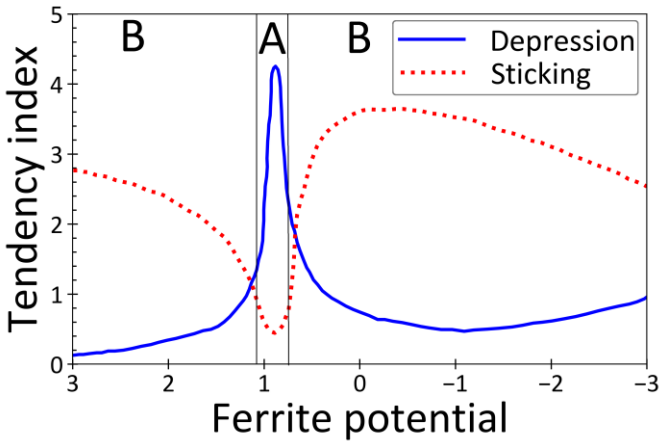

Figure 2.3. Ferrite potential indicator of peritectic steel behavior showing sensitivity of these (type A) steels to depressions, contrasted with sticking tendency of other (type B) steels. Redrawn with permission from reference [151].

Sarkar et al [154] generalized the Wolf ferrite potential for peritectic solidification by including the effects of alloying elements on the C_A, C_B and C_C points, as follows:

$$C_A = 0.0927 + (0.0471\times Mn) - (0.0859\times Si) - (0.0237\times Ni) - (0.5429\times S) - (0.3553\times N) - (0.0361\times Ti) - (0.0136\times Nb) + (0.0106\times V) + (0.1097\times Mn\times Si) - (5.6239\times Mn\times S) - (0.0165\times Mn^2) \quad (2.9)$$

$$C_B = 0.1716 - (0.0589\times Mn) - (0.1776\times Si) - (0.0053\times Cr) - (0.0410\times Ni) + (0.0473\times Al) - (0.9453\times S) - (0.0160\times P) - (0.6884\times N) + (0.0283\times Ti) - (0.0147\times Nb) + (0.0285\times V) + (0.2342\times Mn\times Si) \quad (2.10)$$

$$C_C = 0.5274 - (0.0124\times Mn) - (0.1424\times Si) - (0.0154\times Cr) - (0.0981\times Ni) + (0.0934\times Al) - (0.3871\times S) - (0.0533\times P) - (2.0916\times N) + (0.1226\times V) + (0.2363\times Mn\times Si) + (0.0729\times Mn\times P) - (0.0729\times Mn^2) \quad (2.11)$$

Using the same form as Wolf [151], they [154] redefined ferrite potential as follows:

$$FP = \frac{C_C - [C]}{C_C - C_A} \tag{2.12}$$

where [C] is the carbon weight percentage. When $\frac{C_C - C_B}{C_C - C_A} < FP < 1$ the steel is a depression-sensitive, or "peritectic", grade and when $0 < FP < \frac{C_C - C_B}{C_C - C_A}$ or $FP > 1$ the steel is a sticking-sensitive grade. This new ferrite potential criterion [154] has same critical range to define peritectic behavior as the Blazek method, C_A < [C] < C_B. This equation also matches the Wolf ferrite potential equation, for low alloy steels containing Mn, Si, Ni, Cr, and Mo, without considering Sulfur.

2.3.6 Calphd Method

Calculation of multicomponent phase diagrams using commercial thermodynamics-based software like ThermoCalc [170] is an important tool for help in identification of peritectic steels. Such modeling tools are better suited for high alloy steels than the pseudo-binary assumption inherent in the empirical models presented in the previous sections. However, the accuracy of these software tools depends on their databases, which have been developed only for a limited set of conditions. Furthermore, reliable criteria are still needed to infer peritectic behavior from the phase diagram predictions. To do this, fundamental understanding of peritectic behavior is needed, which is reviewed next.

2.4 Mechanisms of Peritectic Solidification

Peritectic solidification has been investigated by many researchers [30-37] and different mechanisms have been proposed to explain the details of this phenomenon. These include thermal diffusion of solute atoms [35], and / or re-melting of delta ferrite [38], to explain the peritectic reaction and diffusion or massive transformation to explain the peritectic

transformation [36, 37, 39-41]. Many models [30-33] assume that the peritectic reaction and transformation are both controlled by the diffusion of solute atoms, especially carbon in plain-carbon steel and nickel in alloy steels. Some measurements, by diffusion-couple [34] and directional solidification experiments [40], agree with these diffusion-controlled models. However, other experimental studies [35, 38, 39, 41-43] have shown that the rates of the peritectic reaction and transformation are very fast, especially γ -austenite layer growth along the liquid/δ -ferrite interface in the peritectic reaction, and especially under realistic, non-equilibrium conditions. Recent phase field simulations suggest that these high rates can be explained by diffusion [44-46]. Other researchers claim that these observations cannot be explained by diffusion mechanism(s) alone, and have suggested other mechanisms, including micro-scale heat transfer and fluid mixing involving delta-ferrite re-melting [35, 38, 41], and massive transformation [38, 47-51]. In the following sections, different proposed mechanisms for the peritectic reaction and peritectic transformation in steels are discussed in turn, after introducing the experimental methodologies used to obtain supporting measurements for these mechanisms and their models.

2.4.1 Experimental Methods for Studying Peritectic Solidification

Four experimental methods have been widely used to study peritectic solidification, including the solid/liquid diffusion couple experiment, high-temperature confocal laser scanning microscopy (HT- CLSM), X-ray imaging, and directional solidification.

In the solid/liquid diffusion couple experiment [34, 171-175], a steel alloy is melted in a crucible and then is slowly cooled down to a specific temperature (for example 1696 K) to crystallize a small amount of the austenite, leaving residual liquid with an equilibrium carbon content at peritectic point. Then, a sample of a different steel alloy (δ-ferrite) from a lower

temperature furnace is positioned just above the alloy already in the crucible. The two alloys are then brought into contact with each other for a preset length of time, forming a diffusion couple, before rapidly dropping into ice water. A longitudinal cross section is etched to reveal the solidification microstructure, and the thickness of the austenite formed between the regions formerly containing δ-ferrite and liquid, as well as measuring the carbon distribution. Although it is a powerful technique to investigate solidification under isothermal conditions [176, 177], other methods are needed for realistic high cooling rates.

High-temperature confocal laser scanning microscopy (HT-CLSM) [141, 155], is a powerful improvement to the conventional optical microscope that focusses a laser beam into a small area on the surface of a high-temperature sample of molten steel [39, 41, 161, 178-180]. While carefully cooling at a desired rate, solidification on the liquid surface can be observed by building up images pixel-by-pixel from photons emitted from the fluorophores. The different solid and liquid phases can be distinguished due to their emissivity differences. HT-CLSM can operate at high temperatures (over 1800 ˚C), has controllable depth of field [181, 182] and high resolution (0.15 μm) [183]. It can record high-frequency images in real time for realistic cooling rates (eg 3000˚C/min)[183] and sample sizes (eg. 8 mm) [183]. Even though only the surface can be seen, the ability of HT-CLSM to visualize peritectic solidification in-situ and in real time is revolutionizing our understanding of the phenomenon.

Time-resolved X-ray imaging has recently been applied to investigate solidification of steels [43, 184-186]. In a synchrotron radiation facility, hard X-rays with photon energy ranging from 10 to 100 keV can penetrate through the bulk metallic material to obtain X-ray images. These systems feature high contrast, high-resolution images due to monochromatic light, high coherency, and high brightness. X-ray imaging has the big advantage over HT-CLSM of being

able to observe the real three-dimensional microstructure evolution inside the bulk volume of the sample [185].

Finally, directional solidification is a laboratory process in which molten metal is drawn downward at a controlled withdrawal speed, *V*, through a controlled temperature gradient, *G* [187-189]. Heating block temperatures beside the sample path are controlled to maintain steady-state conditions in the moving sample in the frame of reference of the laboratory, with a stationary solidification front located between the hot zone towards the top of the apparatus and the cold zone below. This continuous process enables controlled conditions for experimental measurements of solidification, which include the concentration and microstructure profiles. Although the thermal field tends to stabilize the process, the concentration field may produce fluid flow and morphological instabilities near the solidification front, depending on how the liquid density varies with solute concentration [190]. These opposing effects may cause instabilities that equilibrate in amplitude, making this system an excellent vehicle for the careful study of phase transformation dynamics [191]. Due to its ability to control the local casting conditions, which may enable high thermal gradients [192] and deep supercooling [193-195], this technique is good for fundamental study of solidification behavior, especially when combined with X-ray imaging to observe the in-situ microstructure evolution [196, 197].

2.4.2 Diffusion Control Mechanism for Peritectic Reaction

Many modeling and experimental investigations of the peritectic reaction in steel have concluded that it is controlled by the diffusion of solute atoms, especially carbon [34, 41, 48, 171, 179, 198]. According to the equilibrium Fe - C phase diagram (Figure 2.1), at the peritectic temperature, delta-ferrite at only 0.1 pct C is in equilibrium with austenite at 0.18 pct C and liquid at 0.52 pct C. Growth of the austenite plate thus requires the rejection of solute (carbon)

into the liquid, which is proposed by many to be limited by the rate of solute diffusion through the liquid away from the region, specifically carbon in this case. As this peritectic solidification phenomenon occurs at high temperatures (1495℃ in Fe - C binary alloys), early experimental investigations were rare. Thus, early studies of peritectic solidification applied analytical models based on diffusion laws to study the peritectic reaction of steel [30-33].

Many models of the peritectic reaction have been developed to predict the growth rate of the austenite layer along the δ-ferrite / liquid interface during the peritectic reaction, which are based on solving Fick's second law for the diffusion of solute atoms through the austenite phase and mass balances on solute transport across the interfaces [30, 31]. One analytical solution for the γ-platelet growth rate, V_γ [32] in a hypothetical binary Fe - m system, includes the effects of tip radius on the interfacial diffusion:

$$V_\gamma = \left(\frac{9}{8\pi}\right)\left(\frac{D_m^L}{\rho}\right)\omega^2 \qquad (2.13)$$

$$\omega = \frac{\Omega}{1-\frac{2\Omega}{\pi}-\frac{\Omega^2}{2\pi}} \qquad (2.14)$$

$$\Omega = \frac{\left(C_m^{L/\gamma}-C_m^{L/\delta}\right)}{\left(C_m^{L/\gamma}-C_m^{\gamma/L}\right)} \qquad (2\text{-}15)$$

where D_m^L is the diffusion coefficient in the melt of the solute, m such as carbon [39] or nickel [198], through the liquid steel, ρ is the tip radius of the edge of the growing austenite plate along the δ / L interface, (Figure 2.1(b)); Ω is relative dimensionless supersaturation of solute atoms in the liquid above equilibrium at the two interfaces; $C_m^{L/\gamma}$ and $C_m^{L/\delta}$ are the solute atom concentrations in the liquid in equilibrium with the γ and δ phases respectively; and $C_m^{\gamma/L}$ is carbon concentration in the γ in equilibrium with the liquid. These diffusion models typically assume no barrier to γ-phase nucleation upon reaching the peritectic temperature [31]. This

model was extended to better consider surface tension and the capillarity (Gibbs-Thompson) effect between γ austenite and δ ferrite [32]:

$$V_\gamma = \frac{27 D^L R\, T\left(k_{fe}^{\gamma/L} - k_m^{\gamma/L}\right)\left(C_m^{L/\gamma} - C_m^{L/\delta}\right)}{128\, \pi \sigma^{\delta/\gamma} V_m^L} \left(\frac{\Omega}{\omega}\right)^3 \quad (2.16)$$

where R is the gas constant; $k_{fe}^{\gamma/L}$ and $k_m^{\gamma/L}$ are the partition coefficients of iron and solute respectively at the L/γ interface; $\sigma^{\delta/\gamma}$ is the surface tension between δ and γ and is equal to the interface elastic strain energy per unit area at the interface between δ and γ; and $V_{\mathrm{m}}^{\mathrm{L}}$ is the molar volume of the liquid steel. Lateral growth rate is strongly dependent on Ω, which determines by the shape of the phase diagram just below the peritectic temperature. The above calculations were conducted for an Fe - Ni binary system for different Ω values and the calculated growth rates agree reasonably well with measured growth rates [41].

The peritectic reaction has been studied at different temperatures [34] using the method proposed by Ueshima et al [48]. The results showed that decreasing temperature increases the peritectic reaction rate [34]. This is suggested to be due to the significant increase in carbon concentration gradient in the interfaces of austenite with liquid and δ ferrite caused by decreasing temperature. The accompanying decrease in the diffusion coefficient is too small to offset the increase in concentration gradient [34].

Images in Figure 2.4 from a HT-CLSM study of a hyper-peritectic alloy with 5.1 pct Ni [41], show that austenite appears at the triple point formed by the boundaries of two planar δ grains with the liquid. This austenite platelet grows very fast with lateral movement along the L/δ interface, and thickens as it simultaneously grows slowly into both the liquid and the δ ferrite. The measured lateral growth rate (peritectic reaction) increases from 30 to 145 μm/s with increasing cooling rate [41]. This sequence of peritectic reaction steps has been reported for

hyper-peritectic carbon steel (Fe - 0.42 pct C) [39] and for Fe - Ni systems [198]. Lateral growth (peritectic reaction) was much faster (2970 μm/s) in the Fe - C alloy than in the Fe - Ni alloy. This was attributed to the higher diffusion rate of carbon in Fe - C liquid than Ni in Fe - Ni liquid [39].

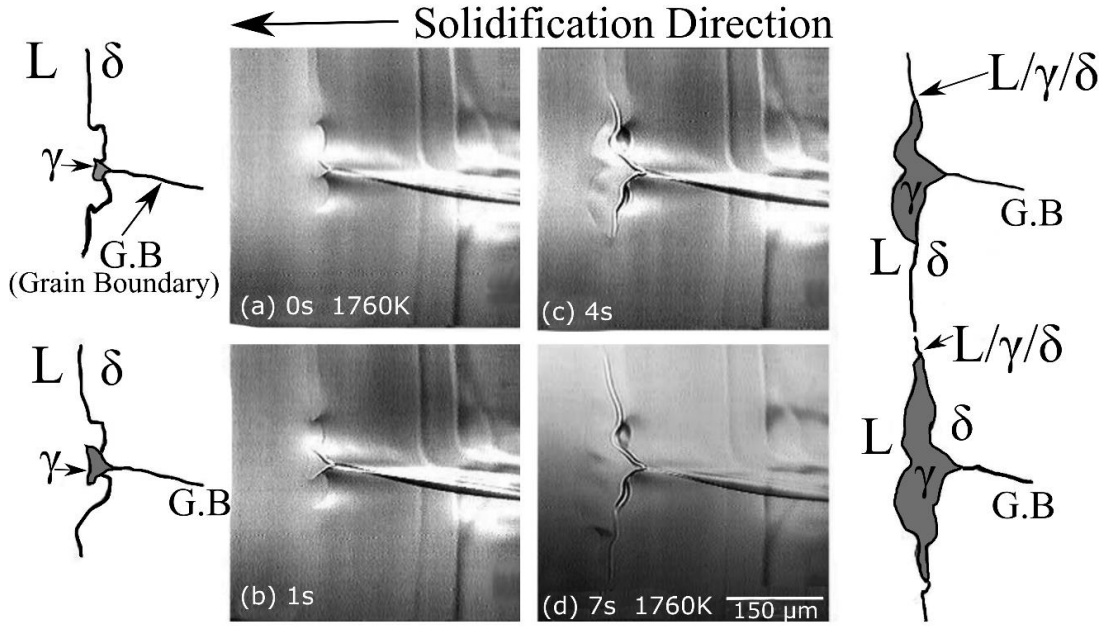

Figure 2.4. Lateral growth of γ at L/ δ interface in the early stages of the peritectic reaction of Fe - 4.86 pct Ni alloy. Reprinted with permission from reference [41].

In another experimental study on Fe - 4.7 pct Ni [179] observing the growth rate of austenite platelets during the peritectic reaction, it was concluded that the nickel diffusion field controlled the growing austenite plates, which is greatly influenced by the tip radius at the edge of the plate. Three regimes were observed for austenite growth along the δ-ferrite/liquid interface: (1) constant tip shape and velocity of two austenite platelets growing towards each other, while their diffusion fields are independent, (2) flattening tip shape and decreasing

velocity, when the plates approach each other, and their diffusion fields likely begin to interact; and (3) sudden distortion of the platelet tips, and increasing velocity, when the adjacent growing austenite tips interfere, indicating that their diffusion fields have drastically changed [179].

2.4.3 Delta-Ferrite Re-Melting Mechanism for The Peritectic Reaction

Based on experimental observations, several researchers have concluded that the peritectic reaction velocity is very fast and thus cannot be controlled only by diffusion of carbon through the γ phase [35, 38, 41]. The re-melting of ferrite ahead of advancing γ phase during the peritectic reaction has been proposed by Hillert [199] as an important mechanism that controls the peritectic reaction. This phenomenon has been confirmed by experimental observations [35, 38] and phase field simulations which include both diffusion and microscale heat transfer [46, 200] and are discussed in the following paragraphs.

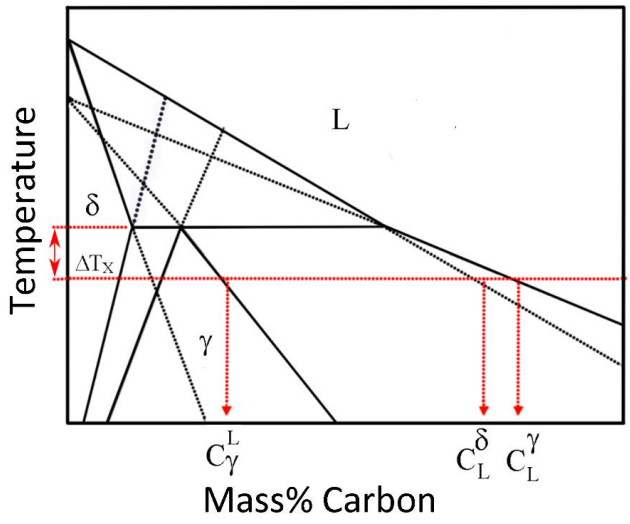

Figure 2.5. Linearized Fe–C phase diagram showing phase compositions at different interfaces. (Solid black lines show equilibrium; dashed black lines show metastable extensions, and thick dashed red lines show undercooled conditions where peritectic reaction actually occurs). Reprinted with permission from reference [35].

Hillert [199] proposed that re-melting of the δ-ferrite interface occurs near the δ / γ /L triple point near the edge of the growing austenite platelet tip. Furthermore, this re-melting was proposed as evidence for a new mechanism for control of the peritectic reaction rate. During cooling from above the peritectic reaction temperature, the formation of austenite with composition of C_{γ}^{L} causes the rejection of carbon into the liquid ahead of austenite plate which is growing along the L/δ interface.

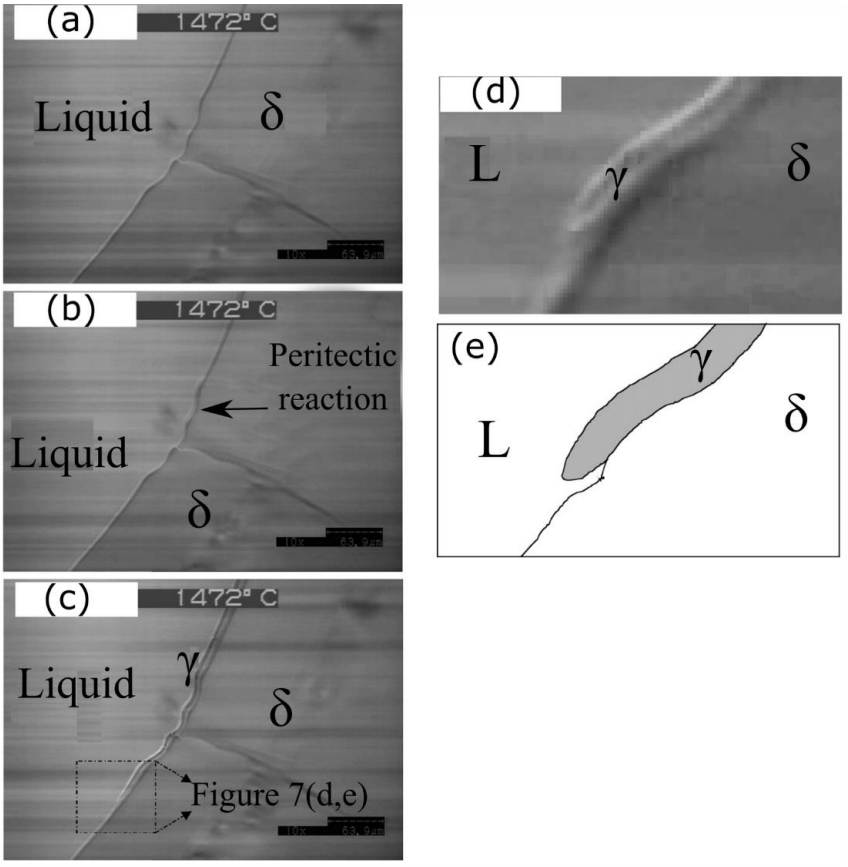

Figure 2.6. HT-CLSM images of the peritectic reaction in Fe – 0.18 pct C, (a) start of peritectic reaction, (b) initiation of austenite layer at liquid/δ-ferrite interface, (c) growth of austenite layer along that interface, (d) close-up of austenite layer showing re-melting of delta-ferrite ahead of its growing edge, (e) schematic of previous frame. Reprinted with permission from reference [35].

In this situation, the carbon concentration at the L/γ interface (C_L^{γ}) is higher than the carbon concentration at the L/δ interface (C_L^{δ}), as shown in Figure 2.5. The δ ferrite is in contact with liquid which is enriched with carbon (above the equilibrium concentration) so it leads to some re-melting of ferrite.

Recent experiments [35] by in-situ HT-CLSM observation (Figure 2.6) obtained visual evidence of this proposed mechanism for the peritectic reaction, in which a thin austenite plate grows along the interface and re-melting of ferrite takes place at the edge of the growing austenite platelet. This landmark experimental observation revealed that the tip velocity at the edge of the growing austenite layer is in the range of 1.4×10^3 μm/s to 12.5×10^3 μm/s. These researchers argued that this rate is higher than that can be explained by diffusion of carbon alone, and that the rate limiting step in the peritectic reaction is dissipation of the latent heat of transformation, rather than carbon diffusion [201]. Although these experimental observations are very clear, other mechanisms cannot be dismissed, because surface phenomena might affect the behavior being visualized on the surface in these microscope images, relative to that in the bulk volume interior of the sample and the real process.

The analytical model in Eq. 2.13-2.15 was used to calculate the growing velocity of an austenite plate [35] due to carbon diffusion, and even for a very low tip radius of 0.15 μm, the predicted tip velocity was much lower than the experimentally observed rate in an Fe - C system [35] of 400 - 12500 μm/s at high undercooling. Thus, it was concluded that the peritectic reaction is not controlled by carbon diffusion alone [35].

Considering the latent heat of transformation, the re-melting of delta-ferrite was proposed to improve the prediction of the reaction rate. Growth rates were calculated using the following equation for directional solidification [202]:

$$V_{max} = \frac{K_s G_s}{\rho L} \tag{2.17}$$

where K_s is the thermal conductivity, taken for δ ferrite, G_s is the thermal gradient in the solid (K/m), ρ is density, and L is the latent heat of fusion, taken to be 62.8 kJ/kg for peritectic transformation in this 0.18 pct C alloy, The calculated growth rates of the austenite platelet with and without considering re-melting are compared in Figure 2.7. Without considering re-melting, the tip velocities are 19 to 855 μm/s for thermal gradients of 1 to 45 K/mm, which are considerably lower than the measured velocities. Including 50 kJ/kg of latent heat released by austenite formation to remelt some of the delta-ferrite, the calculated reaction velocity increased to 315-12500 μm/s, which is in the range of the measurements.

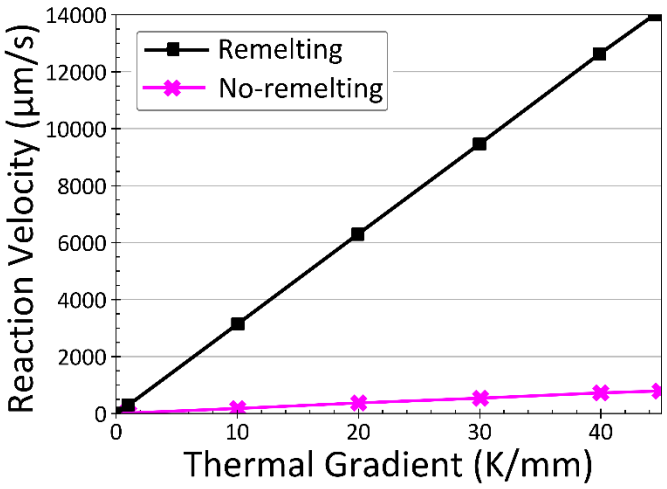

Figure 2.7. Calculated growth rates of an austenite platelet along the liquid/delta-ferrite interface with and without consideration of delta-ferrite re-melting. Reprinted with permission from reference [35].

Based on these findings, an alternative mechanism for the peritectic reaction was proposed. Some of the latent heat released by the austenite formation could remelt some nearby ferrite. Then, instead of requiring diffusion to transport carbon away from the solidifying austenite tip, the remelted delta ferrite (0.1 pct C) mixing with the enriched liquid (0.52 pct C) ahead of the austenite tip (0.18 pct C) could produce liquid at roughly the required composition for the solid austenite. The austenite tip therefore can grow into liquid at about the same composition, without the need for much carbon diffusion. This would enable the high austenite growth rates observed.

The re-melting phenomenon has also been observed by other HT-CLSM experiments [38]. A sequence of events during intermittent austenite growth in a Fe - 0.43 pct C alloy near equilibrium is shown in Figure 2.8, with a schematic illustrating the expected temperature evolution provided below.

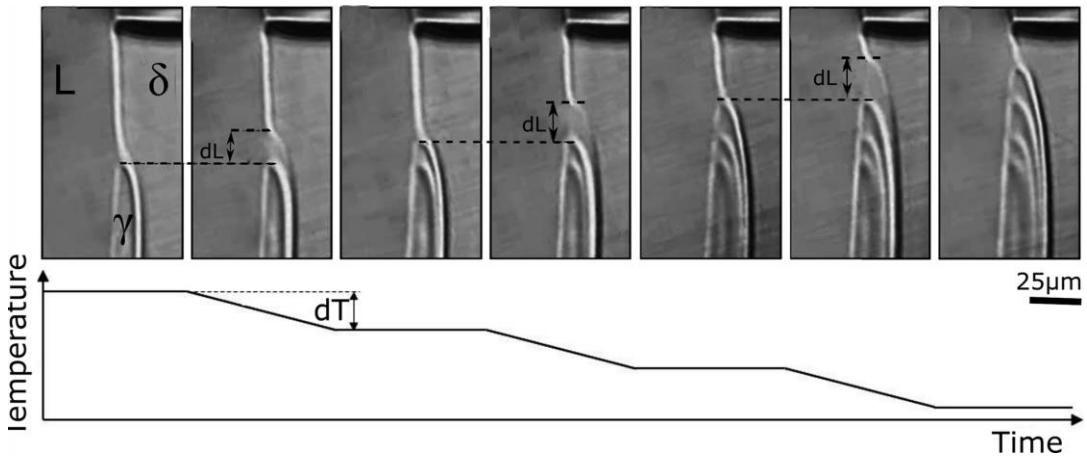

Figure 2.8. Sequence of events during incremental growth of γ in a Fe - 0.43 pct C alloy, showing temperature and microstructure at different times. Reprinted with permission from reference [38].

To explain the discontinuous growth in this figure, these authors argue that the re-melting of δ –phase occurs first and causes the sudden γ plate growth. When temperature is relatively constant, all three phases are proposed to be in equilibrium and no diffusion takes place (Figure 2.8 top frames 1,3,5, and 7). Decreasing temperature creates a driving force for diffusion. In both Fe - C and Fe - Ni systems, this driving force is much higher for the solute atoms than for the iron atoms. Thus, the partitioning of solute atoms occurs first and causes re-melting of some δ–ferrite phase (Figure 2.8 top frames 2,4,6 with dashed lines and temperature drops). After a certain amount (length *dL)* of δ has re-melted, the γ phase grows into the re-melted region.

This mechanism agrees with Hillert [199] but contrasts with Phelan et al [35] who believe that the re-melting of δ ferrite takes place due to the dissipation of latent heat released during the growth of the γ. The re-melting phenomenon has been also reported in peritectic solidification of Fe - Ni alloys [41].

The δ-ferrite re-melting phenomenon has been confirmed by several phase field modeling studies [45, 203-205]. For example, Figure 2.9 shows how the δ/γ/L triple point and associated interfaces move during γ growth at different undercoolings [46]. In addition to a sharper tip radius, increasing undercooling causes the δ / L interface near this junction to move toward the δ phase, which indicates some re-melting of the delta region.

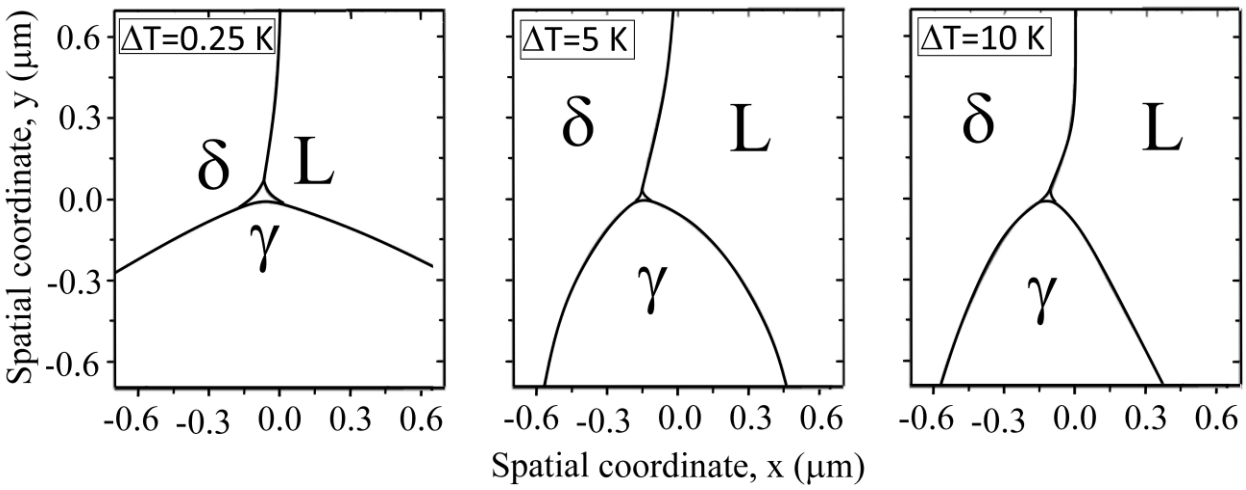

Figure 2.9. Shape of interfaces calculated near the triple-point junction during the peritectic reaction at different undercoolings. Reprinted with permission from reference [46].

In another phase-field modeling study [200] of the peritectic reaction focusing on the L/δ/γ triple point, the liquid region expands towards the δ ferrite, as shown in Figure 2.10, again indicating melting of the δ-phase in front of the growing γ platelet. This melting reduces the local supersaturation, which enhances growth of the γ platelet. Thus, it appears that the peritectic reaction is controlled by a complex mechanism that involves microscale heat transfer that causes some re-melting of δ ferrite near the tip of the advancing γ platelet, and mixing of solute in the liquid phase, in addition to solute diffusion.

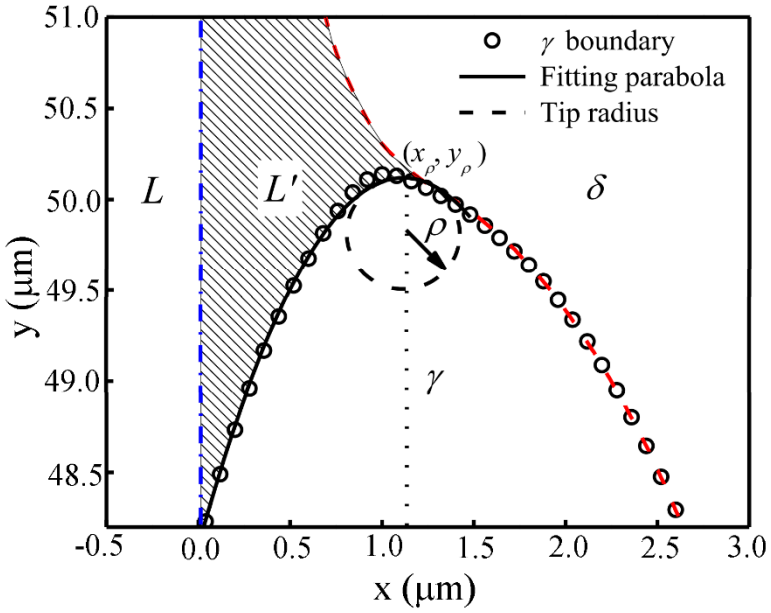

Figure 2.10. Phase field simulation of tip region of the growing γ platelet, where *L* represents the original liquid region, and *L*́ represents the liquid region formed by melting some δ phase. Reprinted with permission from reference [200].

2.4.4 Diffusion Control Mechanism for Peritectic Transformation

Many researchers have proposed that the peritectic transformation in steel is controlled by diffusion [32-34, 38, 206, 207]. The austenite layer initially grows laterally along the L/δ solidification front, and locally replaces the L/δ interface with a thin layer of austenite, which is the peritectic reaction discussed in the previous sections. After the *L/δ/γ* triple-point junction has moved past, the remaining γ layer thickens by growing into both the solid δ and into the liquid. This transformation of the delta ferrite and liquid to austenite, which takes place by solid state phase transformation on one side of this layer (δ→ γ), and the direct solidification of austenite on the other side (L→ γ), is referred to as the peritectic transformation. In the mechanism discussed in this section, the growth of both sides of the austenite layer is controlled by diffusion.

Fredriksson and Nylén [33] proposed that the peritectic transformation is controlled by diffusion of solute from the melt to the δ ferrite through the γ austenite layer. They derived a theoretical model for the thickening rate of γ during the peritectic transformation (F-N model) assuming that (1) the peritectic transformation is controlled by diffusion and proceeds at a low undercooling; (2) the interface concentrations are in equilibrium; (3) the concentration gradients are linear in all three phase regions:

$$\frac{\partial d_{\delta/\gamma}}{\partial t} = \frac{D_\gamma}{d_\gamma}\left(\frac{C_m^{\gamma/L} - C_m^{L/\gamma}}{C_m^{\gamma/\delta} - C_m^{\delta/\gamma}}\right) \tag{2.18}$$

$$\frac{\partial d_{L/\gamma}}{\partial t} = \frac{D_\gamma}{d_\gamma}\left(\frac{C_m^{\gamma/L} - C_m^{\gamma/\delta}}{C_m^{L/\gamma} - C_m^{\gamma/L}}\right) \tag{2.19}$$

where $\frac{\partial d_{\delta/\gamma}}{\partial t}$ and $\frac{\partial d_{L/\gamma}}{\partial t}$ are the growth rates of γ toward δ and toward the melt, respectively; d_γ is the instantaneous γ layer thickness; D_γ is the diffusion coefficient in γ; $C_m^{\gamma/L}$ and $C_m^{L/\gamma}$ are the equilibrium concentrations of solute m in γ and in the melt at the L/γ interface, respectively, and $C_m^{\gamma/\delta}$ and $C_m^{\delta/\gamma}$ are the corresponding equilibrium concentrations in γ and in the δ ferrite at the δ/γ interface. Other researchers [206, 208-211] proposed similar analytical diffusion-based models for describing peritectic transformation in different alloys.

The F-N model was used [207] to calculate γ platelet growth due to carbon diffusion during the peritectic transformation in Fe - C systems. At an undercooling of 5°C below the peritectic temperature, and a cooling rate of 1℃/min, the calculated growth rate with this model agreed well with experimentally-observed growth rates for Fe-0.42 pct C, as shown in Figure 2.11 [207]. Although the F-N model agrees reasonably well with measurements at low undercoolings for Fe - C alloys,[38] at high undercooling the F-N model predicts considerably slower growth rates than measured.[34, 171]

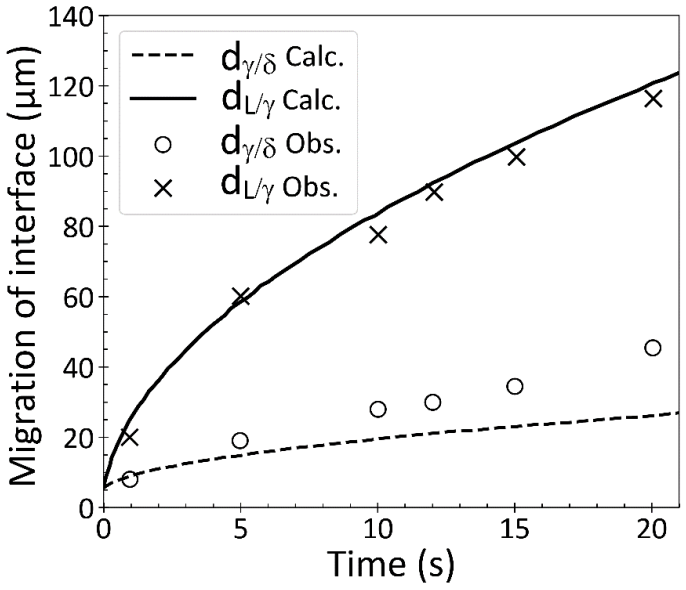

Figure 2.11. Calculated and observed migration of the γ layer toward δ and toward the melt during the peritectic transformation of Fe - 0.42 pct C alloy. Reprinted with permission from reference [207].

In the F-N model it is assumed that there is complete mixing of solute in both the primary liquid and in the δ phase. This assumption may be reasonable for isothermal conditions or low cooling rates. However, when the cooling rate is fast, there is a substantial solute buildup in the liquid ahead of the γ/L interface, creating a solute gradient in the liquid. A diffusion controlled analytical model of isothermal peritectic transformation was developed that considers solute diffusion in all three phases including this liquid solute gradient and reported good agreement with measurements [212].

Experiments using the solid/liquid diffusion coupled method measured [34] austenite plate thickness growth, based on etching to resolve the prior L/γ and γ/δ interfaces. The measured growth of the austenite plates with time, while holding at 1696 K is shown in Figure 2.12.

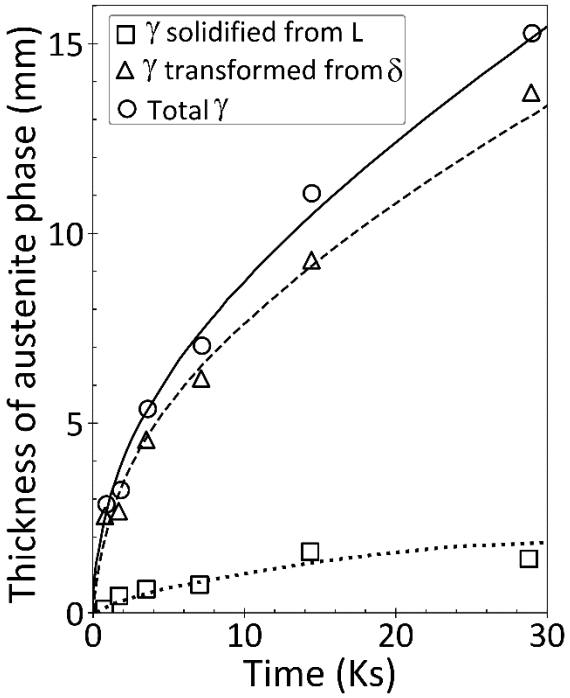

Figure 2.12. Growth process of austenite phase at 1696 K. Reprinted with permission from reference [34].

The increase in measured thickness, x, fits roughly with the theoretical exponent of 0.5 for diffusional growth:

$$x_{\gamma/\mathrm{L}} = 5.4t^{0.57} \tag{2.20}$$

$$x_{\gamma/\delta} = 80t^{0.5} \tag{2-.21}$$

$$x_t = 85.7t^{0.5} \tag{2.22}$$

where t is time (s), $x_{\gamma/\mathrm{L}}$ and $x_{\gamma/\delta}$ are the thickness (μm) of the γ-phase solidified from the liquid phase and transformed from the δ-phase, respectively, and x_t is the total thickness of the γ platelet. The measured growth rates in this experiment match the calculated growth rates, based on the diffusion-controlled mechanism [32].

These curve-fits of measured results show that during peritectic transformation, the γ/δ interface does not move until carbon concentration at this interface increases, according to the

solid-state partitioning observed between the solvus lines in the phase diagram (Figure 2.1). This solute buildup requires carbon atoms to diffuse from the liquid phase through the γ-phase to this γ/δ interface. As shown in Figure 2.13, when carbon concentration in the ferrite is less than 0.09 pct C, the interface moves very slowly until carbon concentration reaches saturation (equilibrium) at the interface. The growth rate then follows the classic parabolic growth (0.5 exponent function) expected for diffusion-controlled systems.

Other investigations of this peritectic transformation have confirmed this growth relationship with the square root of time using measurements based on HT-CLSM observations [38, 47]. The rate constant, 85.7 μm/$\sqrt{s}$ in Eq. 2.22, actually depends on the diffusion coefficient of carbon in austenite, and the difference of carbon concentration at the δ/γ and γ /L interfaces.

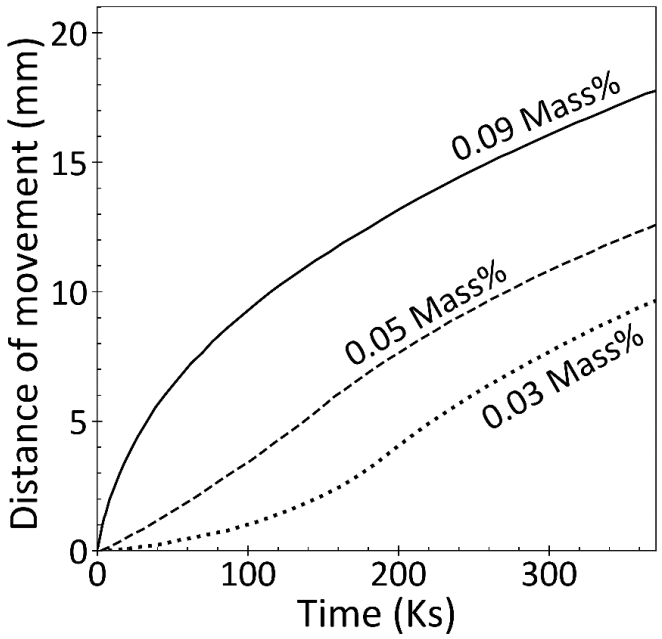

Figure 2.13. Measured movement of the γ/δ interface during the peritectic transformation at 1763 K for various initial carbon contents in the δ-phase. Reprinted with permission from reference [34].

HT-CLSM has also been used to measure isothermal peritectic reaction rates in Fe - Ni systems and compared with model predictions [198]. Observations showed that increasing undercooling caused increasing reaction rates. With low undercooling, the diffusion coefficient is high, so the driving force due to undercooling controls the reaction rate [198]. At high undercooling, however, the reaction rate decreases due to decreasing diffusion coefficient, which comprises a diffusion-controlled regime. These trends were confirmed by calculations with another diffusion model [30] but that model considerably underpredicted the measurements. This was attributed to inaccurate diffusion coefficients in the molten metal and the neglect of diffusion in the solid.

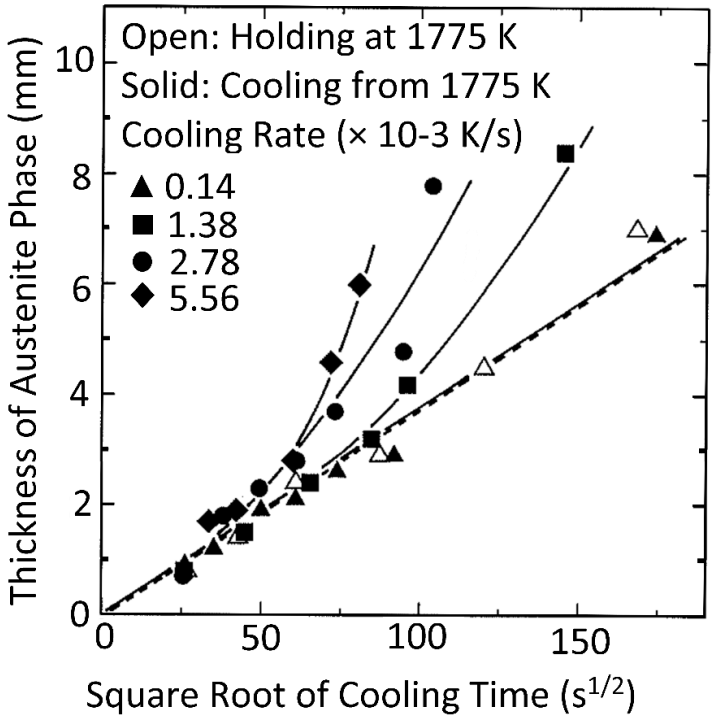

Figure 2.14. Effect of cooling rate on the relationship between total austenite platelet thickness and square root of cooling time. Reprinted with permission from reference [213].

Diffusion couple experiments showed that [213, 214] increasing cooling rate increased the migration rate of both δ/γ and L/γ interfaces. For all cooling rates, the δ/γ interface moved much faster than the L/γ interface [34]. This has been attributed to the smaller difference in carbon concentration at the δ/γ interface. Figure 2.14 shows that at higher cooling rates, the total austenite thickness growth rates exceed the square root of cooling time relationship expected from simple diffusion.

It has been experimentally shown that the peritectic transformation in steel can be very fast and thus difficult to explain by diffusion alone [36, 39]. This implies that the peritectic transformation might be controlled by other mechanisms. Many researchers have used phase-field modeling to investigate these possibilities.

Phase-field models have become an efficient method to simulate phase boundary evolution during phase transformations [215-219]. Phase-field models are based on minimizing total free energy everywhere in a highly refined computational grid of a representative solidifying domain, including bulk free energy, interfacial energy, and elastic strain energy. Its advantages over other methods include its ability to calculate the microstructure morphology, without needing to track the location of assumed interfaces, and to include the diffusion of multiple solute elements [215].

Earlier works [34] found that the δ/γ interface moves faster than the L/γ interface, as already mentioned. But phase-field simulations predict that increasing cooling rate from 10 to 100 K/min should cause this trend to reverse [49, 201], so at 100 K/min the L/γ interface moves faster. This is due to changes in the solute profile in the liquid, as shown in Figure 2.15. A flatter solute profile is predicted at 10 K/min than at 100 K/min. According to the diffusion mechanism, the carbon flux from austenite to the liquid depends on the carbon diffusion coefficient and the

concentration gradient in the liquid, as per Fick's Law. Early researchers ignored this change of carbon concentration in the liquid so do not predict this reversal in the growth rate trend.

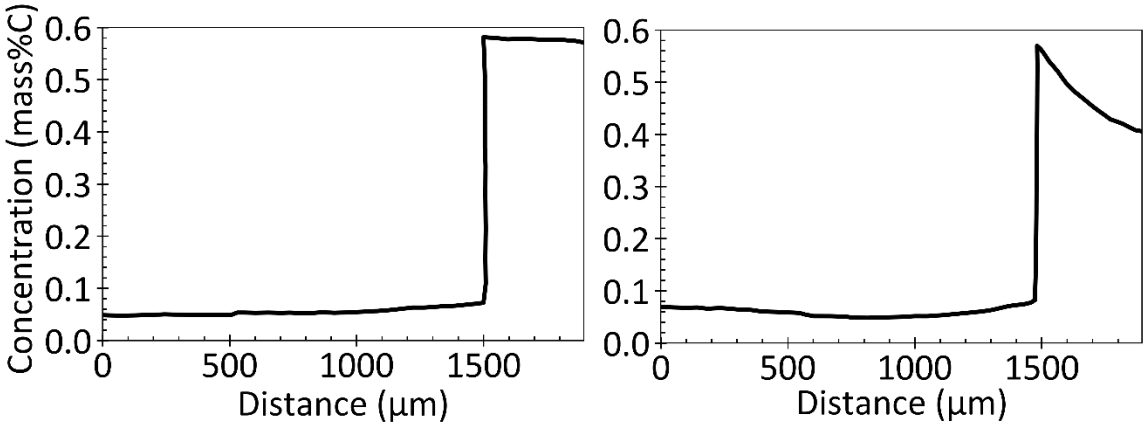

Figure 2.15. Comparison of simulated solute profiles at cooling rates of 10 K/min (left) and 100 K/min (right), in an Fe- 0.18 pct C alloy, under a temperature gradient of 200 K/cm, at the initiation of the peritectic transformation. Reprinted with permission from reference [201].

Peritectic solidification was simulated [44] using another phase-field model which showed that growth rates of the γ phase follow parabolic growth kinetics by focusing on the dependencies of the peritectic transformation on the values of the partition coefficient and solid diffusivities [220]. The distance travelled by each interface is governed by a parabolic law $x_{ij} = a_{ij}t^{1/2}$ in which a_{ij} is a "parabolic" rate constant. The dependence of this parabolic rate constant on the partition coefficient ($k_{\delta\gamma}$) is shown in Figure 2.16. $a_{L\gamma}$ is almost independent of partition coefficient, but $a_{\delta\gamma}$ decreases considerably as the partition coefficient increases. This is because the concentration difference at the γ/δ interface increases with increasing of $k_{\delta\gamma}$, while the value of $k_{L\gamma}$ has no effect on the concentration difference at γ/δ interface. By raising concentration

difference at the γ/δ interface, the amount of solute that must diffuse for δ/γ transformation increases, and consequently the migration distance of the γ/δ interface decreases.

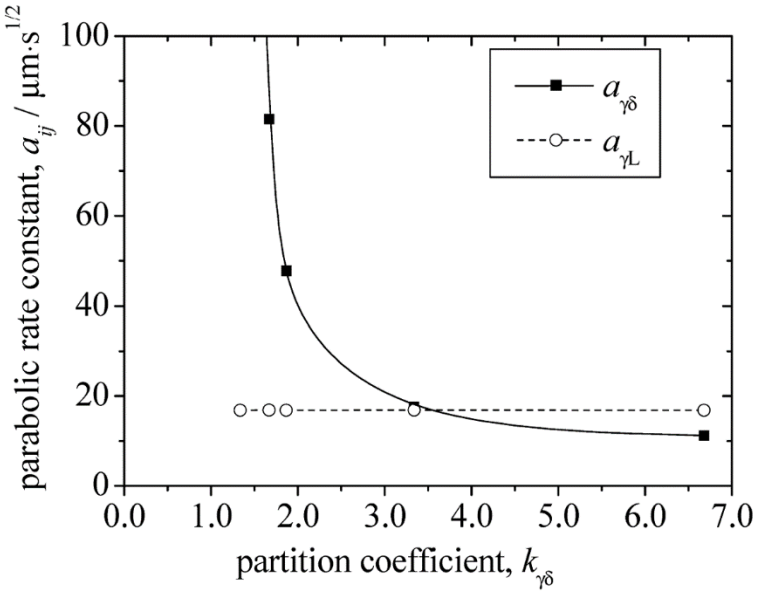

Figure 2.16. Dependence of parabolic rate constant, a_{ij}, on partition coefficient, $k_{\gamma\delta}$. Reprinted with permission from reference [220].

The relationship between parabolic rate constant and diffusion coefficient is shown in Figure 2.17. The rate constant at the γ/L interface is independent of solid diffusivity but the constant rate at the γ/δ interface decreases with decreasing solid diffusivity. Migration of the γ/δ interface was more sensitive to D_δ than to D_γ, due to the larger concentration gradient in the γ phase than in the δ phase. When the solid diffusivities are too small, the peritectic transformation rate is determined only by γ solidification. These authors conclude that the peritectic transformation is initially controlled by solid-solid transformation, and when the solid-solid interface velocity decreases, austenite plate thickens by direct solidification.

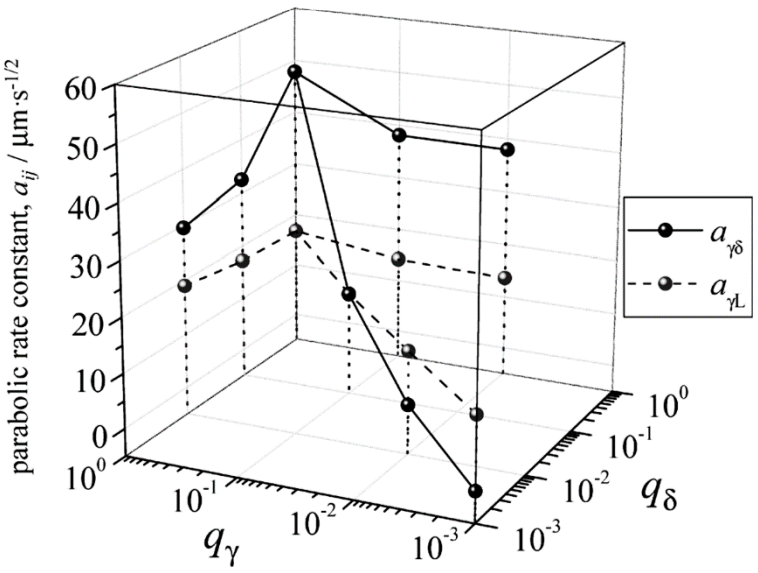

Figure 2.17. Dependence of parabolic rate constant on the diffusion coefficient. The diffusion coefficients, D_δ and D_γ, were defined as $D_\delta = q_\delta \cdot D_\delta^i$ and $D_\gamma = q_\gamma \cdot D_\gamma^i$, respectively, with $D_\delta^i = 4\times 10^{-9}$ and $D_\gamma^i = 6.0\times 10^{-10}$ m^2/s. Reprinted with permission from reference [220].

Additionally, isothermal peritectic transformation has been simulated for dilute Fe - C alloys, by focusing on a single γ-platelet growing into the *L*- and δ-phases [200, 212]. The interfaces were assumed to be in quasi-equilibrium and peritectic transformation governed by diffusion. The results matched expectations that by increasing undercooling, the tip growth velocity of platelet increases considerably, as seen in Figure 2.18. At the same time, the platelet thickness decreases. Experimental data for a Fe - 0.43 pct C alloy [36] are also included in this figure. Phase-field simulation of peritectic reaction and transformation in an Fe - Mn system [221] again indicated that diffusion was rate controlling.

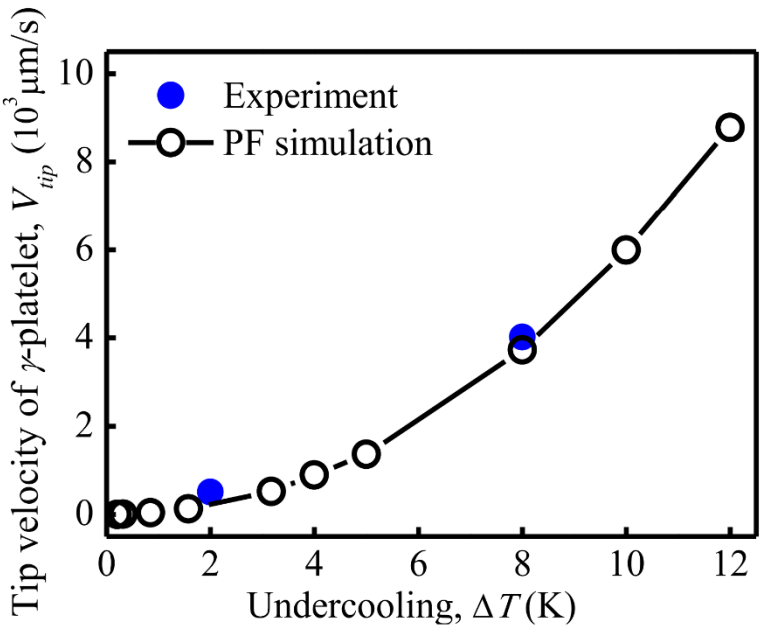

Figure 2.18. Tip velocity of platelet as a function of undercooling. Reprinted with permission from reference [200].

2.4.5 Massive Transformation Mechanism for The Peritectic Transformation

Massive transformation has been proposed as another explanation of the high velocities observed for the peritectic transformation [39, 41-43, 50, 222]. Massive transformation involves a change in crystal structure on an atomic scale without compositional partitioning or solute diffusion, and typically occur during rapid cooling [223, 224]. Massive transformations are observed when the competing equilibrium transformations involving solute diffusion are prevented (constrained), such as the austenite to alpha-ferrite transformation in steel at high cooling rates [225, 226]. Massive transformations are thermally activated, meaning that they proceed when a particular temperature is reached, more according to when the volume free energy of the new product phase is lower than the parent phase, more than when a certain diffusion-controlled compositional requirement is achieved. They require nucleation of the new phase and growth, due to the random migration of individual atoms across the interphase

boundary [227, 228]. and they involve length scales that are so short range that diffusion effects are very small [228]. Once nucleation takes place, the new phase grows at high velocities (up to 1 to 2 cm/s) with approximately the same rate in all directions. The rate of massive transformation is between diffusional transformation rates (nm/sec) and the diffusionless martensitic transformation, which occurs at a velocity near to the speed of sound (~10^3 m/s) [164].

As discussed in earlier sections, the rate of peritectic solidification of steel in undercooled conditions is very high, and is claimed by some researchers not to be explained by the diffusion models discussed previously [39, 41-43, 50, 222]. The observed high transformation rates have been attributed to massive phase transformation from δ to γ or to direct solidification of γ from liquid. In fact, non-equilibrium conditions were proposed to constrain the nucleation of γ phase until considerable undercooling below the peritectic temperature and then upon nucleation, growth proceeds extremely fast. Different nucleation constraints and transformation mechanisms have been proposed and are discussed in the next sections.

Peritectic solidification in Fe - 0.14 pct C alloys was measured [39] to be very fast (3.64 to 5.45 mm/s) for the peritectic transformation (thickening of γ austenite to ferrite and liquid). The thickening rate of austenite is between 3.64 to 5.54 mm/s. Also the migration rate of the γ/δ interface was measured to be faster than the migration rate of the L/γ interface during the peritectic transformation. In Fe - 0.14 pct C the peritectic transformation was believed to be too fast to be controlled by diffusion [47], which was instead attributed to massive transformation. On the other hand, in Fe - 0.42 pct C, the peritectic transformation was believed to be controlled by diffusion [47]. No explanation was provided to explain the difference between these two alloys.

Others researchers [41] used HT-CLSM to study peritectic solidification in an Fe - 5.1 pct Ni system. Again, high peritectic transformation rates were observed and attributed to massive transformation. This was attributed to the primary δ-ferrite being a metastable phase which transformed massively to γ.

Peritectic solidification in a medium-alloy steel [42] has been studied using directional solidification and thermal analysis. Segregation of chromium which was measured by EPMA appeared to cause direct solidification of austenite from liquid without a peritectic reaction [229]. Based on the alloy segregation pattern and presence of lattice defects and thermal analysis, these authors argue that the peritectic transformation where austenite precipitates directly from δ ferrite is a diffusionless transformation, which started at 5 K undercooling [42]. This transformation caused an observed sudden rise in temperature, followed by diffusion-controlled transformation.

Yasuda et al [43] investigated peritectic solidification in a Fe - 0.45 pct C- 0.6 pct Mn- 0.3 pct Si using a synchrotron radiation X-ray system. Two different mechanisms were proposed for solidification of this alloy according to the cooling rate. At 10 K/min, the first δ dendrite grows and later transforms to γ austenite, proceeding from the root to the tip of the dendrites, as illustrated in Figures 2.19(a) and (b). This transformation occurs in the mushy region and is essentially conventional, diffusion-controlled peritectic solidification.

At a higher cooling rate of 50 K/min, however, the specimen initially solidified without γ phase formation and later after complete solidification, the δ grains all transform into γ phase in the solid state suddenly, within 1s. This transformation occurred 100 K below the liquidus temperature. Because the δ/γ phase transformation occurred in the single γ phase region, these researchers argued that solute redistribution was not required. The relatively large undercooling

suggested that γ nucleation was difficult, so the eventual peritectic transformation from δ to γ was governed by a massive transformation. Furthermore, the volume shrinkage of this transformation was suggested to induce melt flow to explain the white grooves in the specimen in Figure 2.19(d).

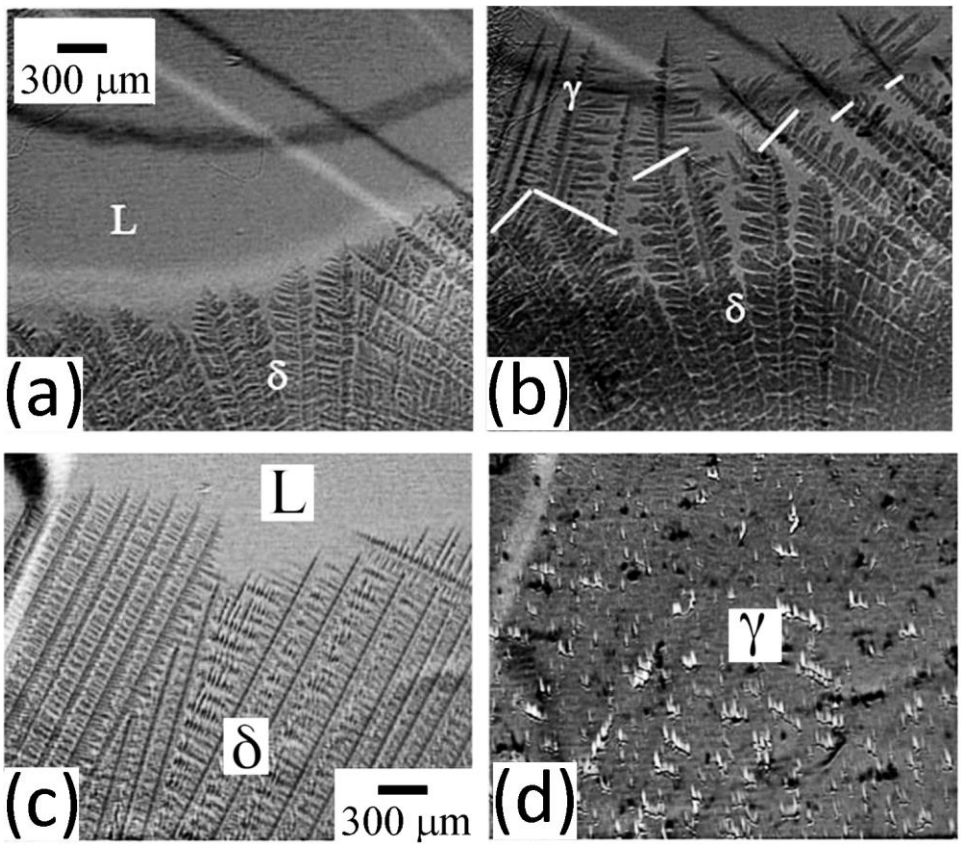

Figure 2.19. X-Ray images of Fe - 0.45 pct C alloy solidification suggesting diffusion-controlled peritectic reaction at 10K/min (a) early time and (b) later time; and massive δ/γ transformation at 50K/min (c) early time and (d) later time. Reprinted with permission from reference [43].

2.4.6 Nucleation Constrained Peritectic Solidification Mechanism

As discussed above, massive transformation may occur when diffusional transformations are constrained, which may occur with high cooling rates and undercoolings. In this situation, the

delay of nucleation of the peritectic reaction step is proposed to combine it with the peritectic transformation step into a single massive transformation mechanism for peritectic solidification [41-43, 229]. Two different mechanisms have been proposed to constrain γ nucleation, to enable massive *δ/γ* transformation, which are discussed in the following subsections.

1- Nucleation constraint due to high δ/γ interface energy

Several researchers have recently proposed that massive transformation is the mechanism for peritectic solidification, due to the delay of γ nucleation in δ ferrite sufficiently to prevent the peritectic reaction, owing to high δ/γ interfacial energy [43, 222]. In-situ observations of peritectic solidification using synchrotron radiation X-ray imaging in Fe - 0.45 pct C- 0.6 pct Mn- 0.3 pct Si alloy were used to explain absence of a conventional peritectic reaction. Instead, at cooling rates above 0.3 K/s, very fast solid state δ/γ transformation was observed [43]. The δ/γ massive transformation needs much higher undercooling than the peritectic reaction, which suggests that difficulty with γ nucleation was responsible for this undercooling. This nucleation difficulty was attributed to poor lattice matching between BCC δ ferrite and FCC austenite [230]. Due to the high nucleation energy of 0.41 J/m^2 needed to create the δ/γ interface [222], the peritectic reaction to form γ was prevented until high undercooling. Then, once the first austenite nucleus formed, the next nuclei of austenite grains form simultaneously.

To investigate the δ-γ massive phase transformation mechanism, the nucleation of γ phase on various interfaces was investigated using phase-field modeling [222]. The simulation results showed that after the first austenite nucleus forms on the δ/γ interface, the driving force (energy barrier) needed to form each additional nucleus drops by half. This suggests the eventual possibility of athermal nucleation, where there is no need for thermal activation. Heterogeneous nucleation onto existing γ phase is much easier than forming new nuclei. This is termed

concurrent γ phase nucleation, as sketched in Figure 2.20 [222]. Following initial nucleation at δ/δ grain boundaries, subsequent nuclei form onto the initial nuclei, where the energy barrier is lower, and later at triple junctions. These predictions agree with in-situ observations of δ/γ massive transformation which measured average δ/γ interface velocities of 200 mm/s [51]. This accelerated nucleation mechanism deserves further study, including investigation of the role of solute redistribution, in order to clarify this massive transformation mechanism to explain peritectic solidification.

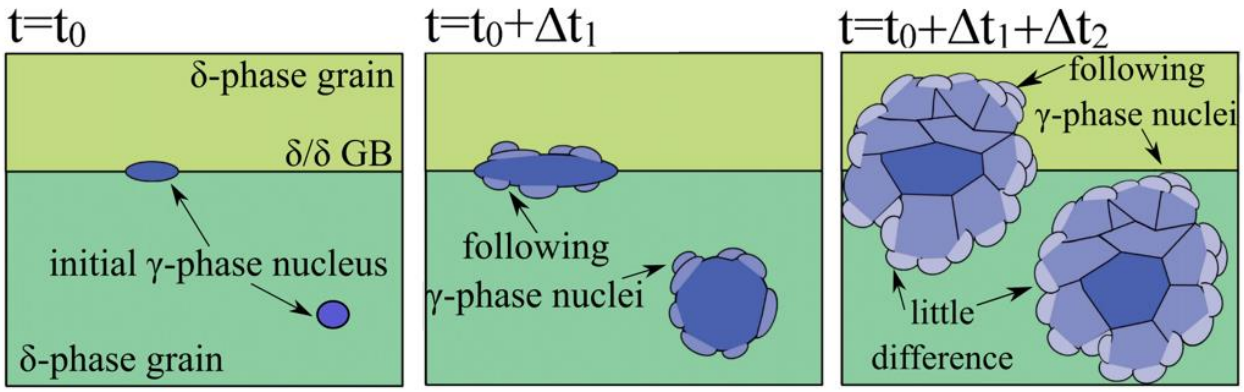

Figure 2.20. Concurrent γ-phase nucleation as a possible mechanism of δ to γ massive phase transformation in carbon steel showing austenite nuclei at different times. Reprinted with permission from reference [222].

2- Nucleation constraint due to solute diffusion

Many experimental studies have reported considerable undercooling for nucleation of austenite in peritectic solidification, and propose that delta to austenite transformation takes place by massive transformation, due to atomic diffusion through the solute field at the L/δ interface [36, 46, 231].

At non-equilibrium solidification conditions, there is a large solute gradient between liquid and δ ferrite. Prior to nucleation, clusters of atoms with an FCC crystal structure (austenite) are proposed to form within the solute diffusion field from liquid to δ ferrite and as solute atoms pass through these clusters, the rates of attachment and dissolution of atoms to the clusters differ. This flux of solute atoms through the cluster is proposed to increase its Gibbs free energy for γ nucleation, which increases the undercooling required for nucleation [50].

This mechanism to explain the high undercooling for γ nucleation was investigated using a HT-CLSM coupled with a concentric solidification technique [50]. Fe - C and Fe - Ni alloys were examined for the same conditions and cooling rates ($7\ ℃/s$) and it was observed that even though the concentration gradient of nickel was ~10 X higher than that of carbon, the higher diffusivity of carbon (D_C^{δ}=5×10-9 m^2/s) led to a much higher flux J_C^{δ}=0.15 μm/s of carbon atoms compared to the flux J_{Ni}^{δ}=0.007 μm/s of nickel atoms (D_{Ni}^{δ}=2.1×10-11 m^2/s). Measurements have shown that the necessary undercooling for δ/γ phase transformation in Fe - C alloy is 8 K, whereas in the Fe - Ni alloy this undercooling is only 1 K, so peritectic solidification takes place by massive transformation and diffusion of solute atoms, respectively [50].

The solidification of steels with 0.1 pct C, 0.18 pct C and 0.43 pct C was investigated using HT-CLSM [36], which noted the decrease in primary δ fraction with increasing C content.

Which leads to different solute gradients at the δ/γ interface and different undercoolings observed for γ nucleation. As shown in Figure 2.21, three different morphologies of peritectic transition were observed for the three steels, which were classified into three different solidification modes. In 0.43 pct C steel, the peritectic reaction takes place near equilibrium conditions at 63 μm/s, with a planar morphology, so is proposed to be diffusion controlled. For

0.18 pct C, the peritectic transformation proceeded with 3K undercooling at 6000 μm/s followed by cellular/dendritic growth. Finally, in 0.1 pct C steel, massive transformation of δ into γ occurred within a fraction of a second with 22K undercooling below the equilibrium peritectic temperature. These results were confirmed by other researchers [231].

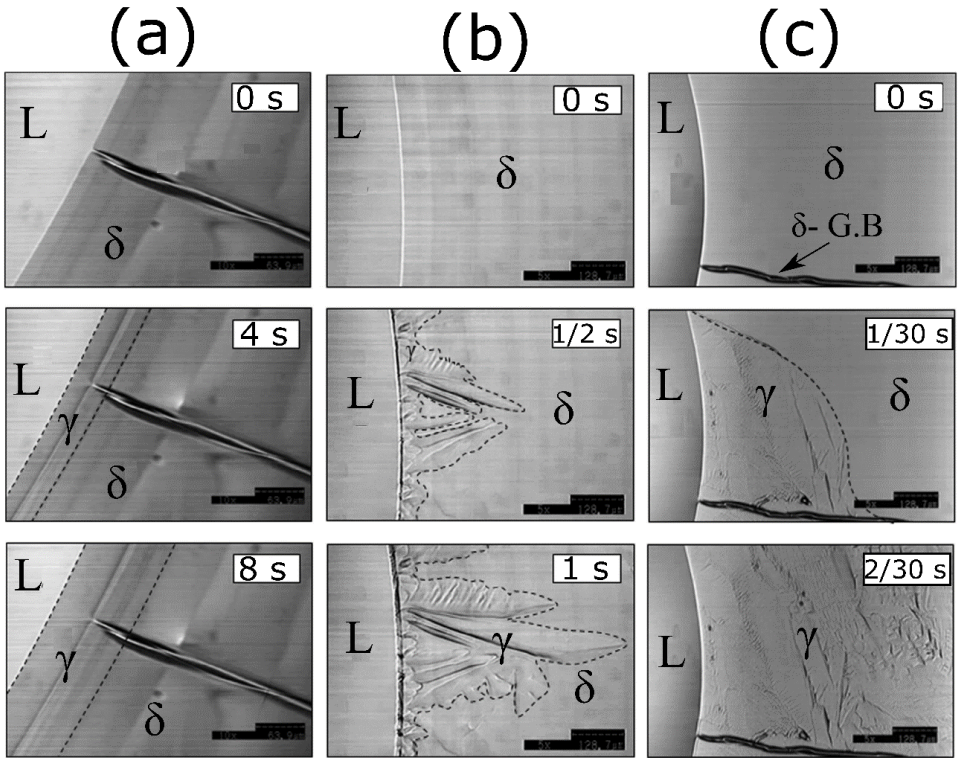

Figure 2.21. Three different modes of the peritectic phase transition observed during concentric solidification in a HT-CLSM: (a) planar (diffusion-controlled), (b) coarse cellular/dendritic (diffusion-controlled) and (c) fine cellular/dendritic (massive transformation). Reprinted with permission from reference [36].

2.5 Effects of Peritectic Solidification

Understanding peritectic solidification in steels is of great practical importance, because peritectic solidification causes many different problems during commercial casting processes

such as continuous casting. These problems include the formation of deep oscillation marks, surface depressions and interfacial gaps in the mold that lead to lower heat flux, thinner, and nonuniform (rippled) solidified shell thickness and accompanying catastrophic breakouts, increased susceptibility to surface crack formation and accompanying oxide slivers, larger austenite grain size leading to lower hot ductility, and consequently more defects in the final product, including internal cracks and accompanying macrosegregation. The following sections explore current understanding of these effects of peritectic solidification.

2.5.1 Mold Heat Transfer and Shell Growth

During casting of steel, heat flux from the solidifying steel to the mold is a strong function of carbon content [116, 127], as seen in Figure 2.22, where the lowest heat transfer rate is measured for the peritectic 0.10 pct C steel. This landmark observation was first published by Singh and Blazek [116], based on continuous casting of 83 x 83 mm square billets on a laboratory caster at 21 mm/s. The corresponding shell thickness profiles were also measured for different steel grades, by inducing breakouts during operation. The measured shell growth profiles roughly follow the parabolic relation [232],

$$s = kt^{0.5} \tag{2.23}$$

where *s* is solidified shell thickness, t is solidification time below the meniscus in the mold, and k is the solidification constant. The shell of the peritectic steel is thinner, as seen in the measurements in Figure 2.23, so the solidification constant in Eq. 2.23 is only 22 mm/$\sqrt{min}$ for the peritectic (0.1 pct C) steel, compared with over 25 mm/$\sqrt{min}$ for low-carbon (0.05 pct C) and for high-carbon (> 0.2 pct C) steel. Although the difference is small, it is very consistent and very significant to steel quality, as explained later. This slower shell growth of peritectic steels is caused by the generally lower mold heat transfer, shown in Figure 2.22, and was suggested to be

caused by shrinkage differences related to the solid-state transformation from δ-ferrite to γ, which is discussed in Section C [116].

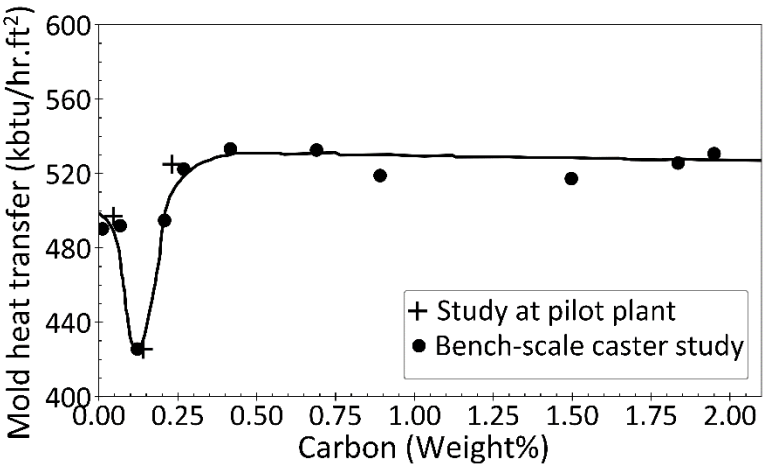

Figure 2.22. Effect of carbon content on mold heat-transfer rate during continuous casting. Reprinted with permission from reference [116].

More important than the thinner shell, however, is the jagged nature of the shell thickness profile for the peritectic steel, which indicates the much larger variability in shell growth of this steel grade. Figure 2.24 compares the appearance of the surface and interior of peritectic and non-peritectic steels [116]. While non-peritectic (0.4 pct C) steels solidify with a relatively smooth interior, the peritectic steel (0.1 pct C) experiences severe ripples on the inside of the shell. In commercial casters, these ripples, which represent local thin, hot, and weak regions in the solidifying shell, are extremely detrimental because they often lead to dangerous and costly breakouts, which are more common in peritectic steels [233].

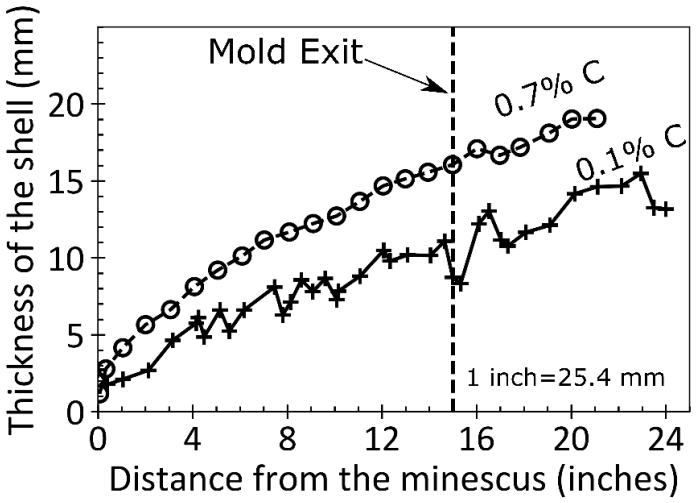

Figure 2.23. Steel shell growth profiles during continuous casting, comparing peritectic (0.10 pct C) and non-peritectic (0.7 pct C) steel grades. Reprinted with permission from reference [116].

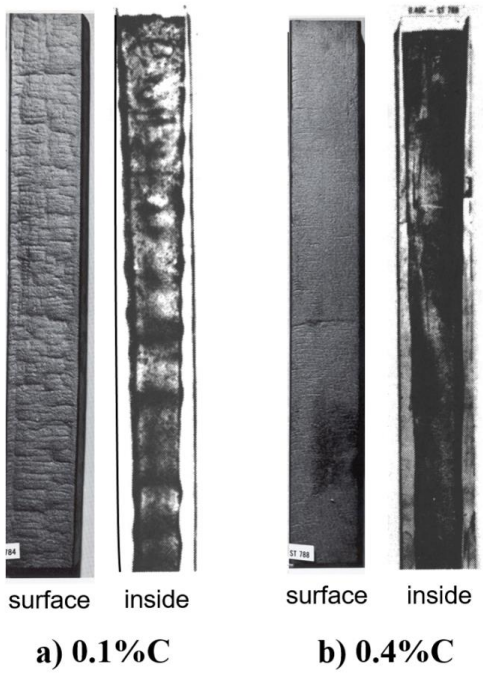

Figure 2.24. Surface and cross section views of solidified shells of continuous-cast steel billets, comparing (a) peritectic steel and (b) and non-peritectic steel. Reprinted with permission from reference [116].

These ripples and thin spots in peritectic steel shells are caused by corresponding deep depressions on the shell surface. Figure 2.24 also clearly shows the rough surface of the peritectic steel billet which contains many depressions [116]. In contrast, the high-carbon (0.4 pct C) steel which has a smooth shell thickness profile also has a very smooth surface. A close-up of a breakout shell in Figure 2.25 shows that each oscillation mark or depression on the shell surface causes a thin region in the shell, in proportion to its severity [234]. The cause of the surface depressions is not due to variations in oscillation of the mold, because the mold in this study was not oscillated [116].

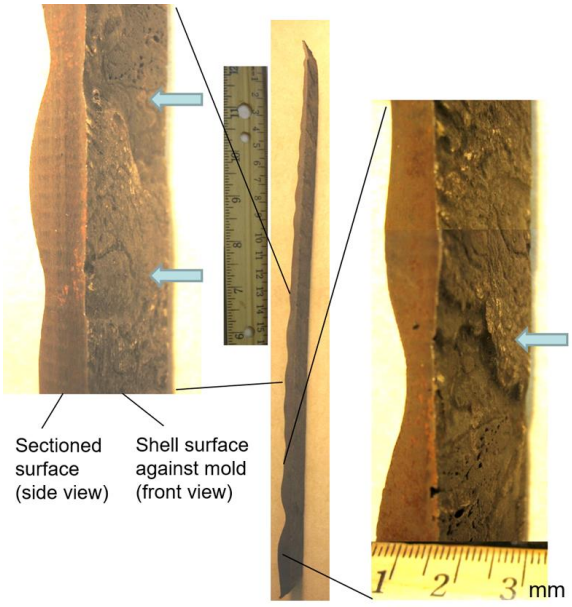

Figure 2.25. Close-up of steel breakout shell showing local thin regions caused by corresponding deep surface depressions. Reprinted with permission from reference [234].

2.5.2 Surface Depression and Air Gap Formation

Depressions and oscillation marks in the as-cast shell surface can be characterized by the surface roughness, which during initial solidification corresponds to deeper interfacial gaps

between the shell and the mold. Measurements of commercial-cast steel show that peritectic steels and ultra-low carbon (ULC) steels experience much more surface roughness problems than other steel grades, as shown for example in Figure 2.26 [24]. This figure is clearly the inverse of Figure 2.22, (with the addition of data points for ULC steel), which indicates that the rougher surface increases the thermal resistance of the interface between the mold and shell, which directly causes lower heat transfer. Many other studies have confirmed that peritectic steels experience deeper air gaps and rougher as-cast surfaces [26, 126, 235-237].

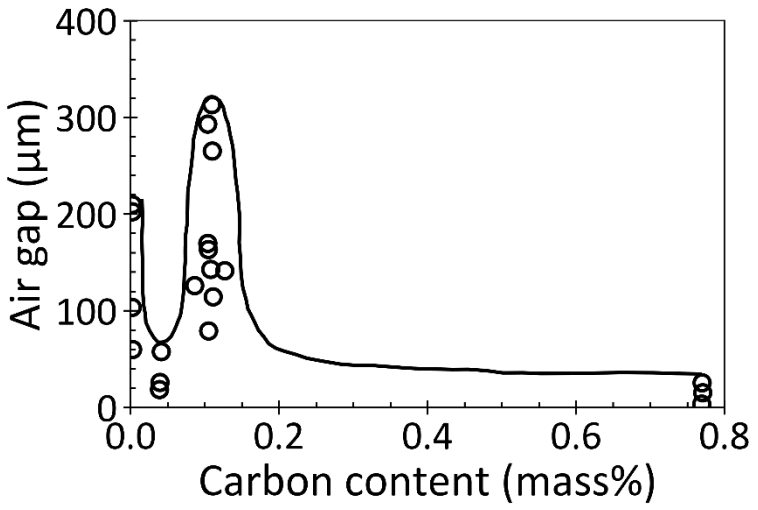

Figure 2.26. Effect of carbon content on the surface roughness of the solidified shell. Reprinted with permission from reference [24].

Fundamental experimental investigation of this behavior can be obtained from the study of free deformation of a solidifying droplet, which was measured for different steels by Dong [238]. Steel droplets solidified onto a chill plate exhibit a curved bottom shape, with a curvature that varies strongly with carbon content. The greatest curvature, indicating lift-off from the plate, was observed with near to pure iron (or “ultra-low” carbon steel) and with near to 0.1 pct C (peritectic steel). Both plain low-carbon hypo-peritectic steel (eg. 0.05 pct C) and higher-carbon

hyper-peritectic steel (eg. 0.2 pct C) show much less curvature (flatter surface) and consequently less gap formation and depression-related problems.

2.5.3 Steel Shrinkage Behavior

A direct measurement of the effect of carbon content on solidification shrinkage with time in a steel ingot casting is shown in Figure 2.27 [239]. A peak in shrinkage is observed for the peritectic steel (0.1pct C). Note that this peak arises very early during solidification. The increase in shrinkage relative to other grades is about 0.3 mm, which remains constant during subsequent solidification [239].

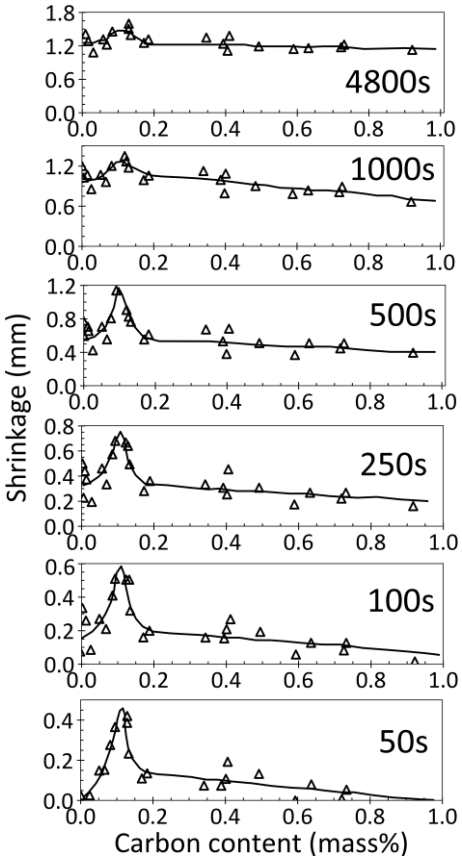

Figure 2.27. Influence of carbon content on shrinkage of steel ingots at various times. Reprinted with permission from reference [239].

Measurements of thermal contraction in binary alloys [240] naturally show a peak for peritectic steels (0.1 pct C), as shown in Figure 2.28. Shrinkage contraction during the solidification of steels with 0.05 - 0.2 pct C has been measured [241, 242]. Peritectic steels (0.1 and 0.13 pct C) achieved their maximum contraction within a few seconds of solidification, perhaps explaining their propensity for surface depressions. In low carbon steels, the maximum contraction arises after solidification is complete [241, 242].

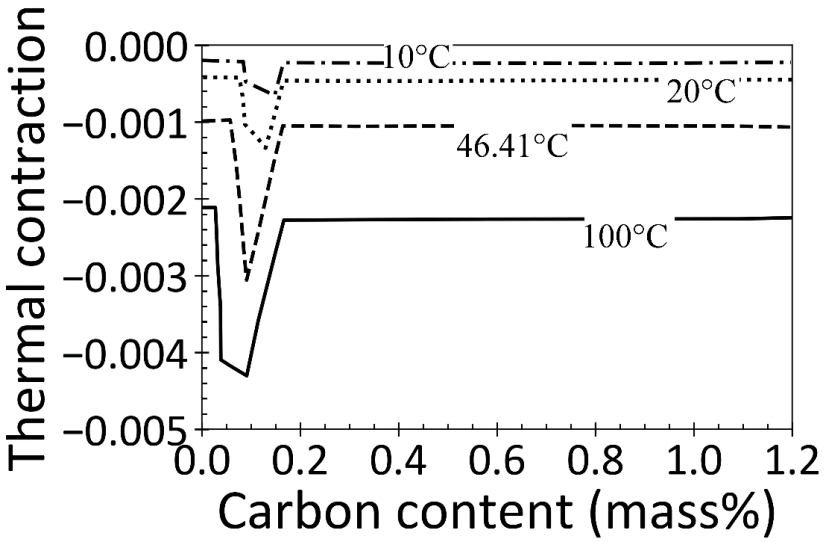

Figure 2.28. Influence of carbon content on thermal contraction of iron-carbon alloys at different temperature intervals below solidus temperature. Reprinted with permission from reference [240].

The root cause of the shrinkage peak in peritectic steels is the δ→γ transformation from body-centered-cubic δ to face-centered-cubic γ, which decreases the molar volume by 2.5 - 3.0 pct [53]. Shrinkage calculations of a solidifying steel shell, such as given in Figure 2.29, show that linear shrinkage increases with time for all steel grades [54]. For peritectic steel (0.126 pct C), the shrinkage is considerably larger, especially near the start of solidification. With low

carbon steels, the δ to γ transformation occurs somewhat later, after the solidified shell is thick enough to withstand the shrinkage, so perhaps is the reason for less bending deformation due to shrinkage in these grades [54].

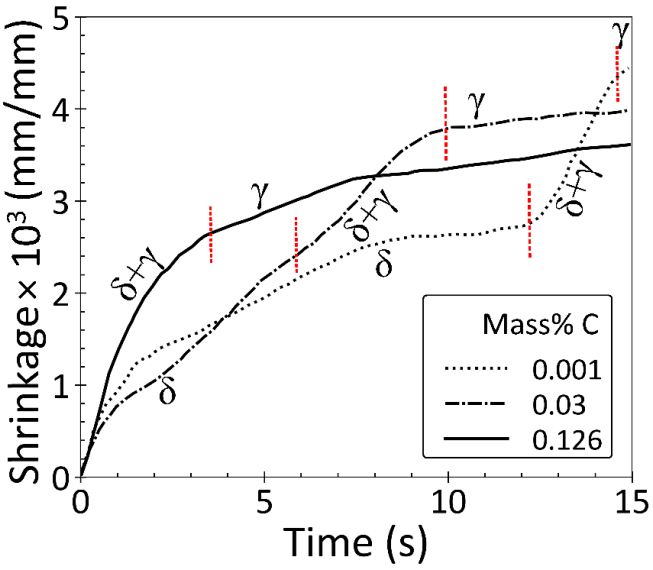

Figure 2.29. Calculated shrinkage of solidifying shell vs. time from the start of casting. Reprinted with permission from reference [24].

Another study of shrinkage behavior with steel grade [243] noted that in low-carbon (0.05 – 0.09 pct C) steel, the temperature range of the δ/γ transformation is 12 - 40 K , while for ultra-low carbon (0.003 pct C) and peritectic steel (0.18 pct C) this transformation theoretically occurs at a unique temperature. Thus, they concluded that ULC and peritectic steels should experience more severe shrinkage problems, owing to the narrow temperature range and accompanying high rate of δ/γ transformation. In contrast, the δ/γ transformation is much slower in low-carbon steels, so the shrinkage is presumably less [243]. In a hyper-peritectic steel containing 0.45 pct C or more, all of the δ ferrite transforms to γ while liquid is still present, leaving γ to solidify

directly from the residual molten steel after the peritectic reaction is completed. Thus, the volume shrinkage accompanying the δ/γ transformation can be accommodated by liquid infiltration and does not lead to shrinkage problems, which require relative shrinkage between two solid (or nearly solid) phases. The rate of δ/γ transformation is suggested to play an important role on the formation of shrinkage depressions and their consequences of air gap formation and cracks [243].

Other researchers [26] explored the reason for more uneven shell growth in ULC and peritectic steels (relative to low-carbon and hyper-peritectic steels), building on that the idea that the rate of the δ/γ transformation is faster in ULC and peritectic steels. A "stress index" was proposed by simply calculating the product of the shrinkage volume occurring for solid fraction from 0.7 to 1.0, and the estimated δ/γ transformation rate. This index is shown in Figure 2.30 as a function of carbon content [26]. The agreement of this index with measured trends suggests that uneven shell growth may worsen with increased cooling rate [243].

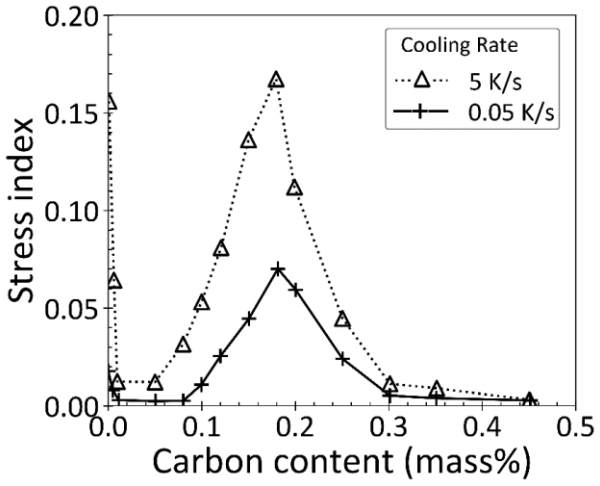

Figure 2.30. Effect of carbon content on stress index, (product of solidification volume and δ/γ transformation rate). Reprinted with permission from reference [26].

Another index of solidification shrinkage was also proposed as a criterion for crack susceptibility, R_v, as follow [27],

$$R_v = \Delta V\,(1-L) \qquad (2.24)$$

Where L is the mass fraction of liquid remaining after peritectic solidification estimated from the lever rule on the Fe-C phase diagram, and ΔV is the volume shrinkage of peritectic solidification, calculated from:

$$\Delta V = \frac{\frac{1}{\rho_1} - \frac{1}{\rho_2}}{\frac{1}{\rho_1}} \qquad (2.25)$$

Where ρ_1 is the density of (L+ δ), and ρ_2 is the density of γ, (L+ γ) or (δ +γ), using measured steel density at different temperatures and phase fractions [27]. This R_v index is shown in Figure 2.31 to reach a peak for peritectic steels as expected, and again suggests that solidification shrinkage due to the δ/γ volume change is the main reason for depression problems in these grades. This figure also suggests that the peak moves to higher carbon contents with segregation and non-equilibrium cooling conditions.

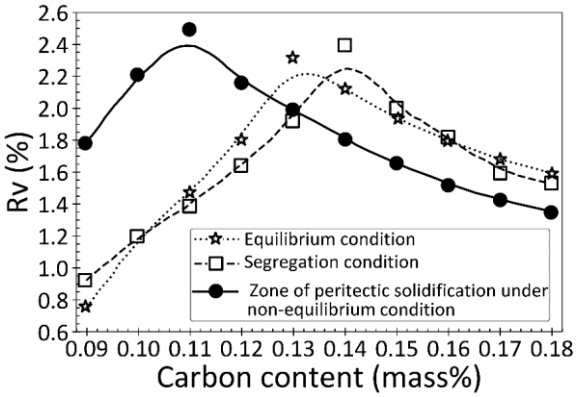

Figure 2.31. R_v shrinkage index variation with carbon content for different cooling conditions. Reprinted with permission from reference [27].

To explain how δ/γ shrinkage leads to depressions, it is important to note that bending to form a depression is more complex than simple linear shrinkage. Temperature gradients leading to shrinkage gradients is one mechanism to explain this behavior. Wolf and others have proposed another mechanism, that microstructure nonuniformities during the peritectic transformation may also contribute: Figure 2.32 suggests two different possible scenarios [244]. At high cooling rates, or with peritectic steels which may have insufficient carbon diffusion to the interior of the dendrites, Figure 2.32(a) illustrates how austenite might nucleate first on the dendrite exterior, with mainly transverse movement of the γ/δ interface inwards, leaving δ ferrite along the center of each dendrite. When that δ ferrite eventually transforms to γ, the shrinkage would be mainly transverse (perpendicular to the solidification direction), leading directly to bending strain (and depressions) or to interdendritic hot-tear cracks, if the bending were constrained. At low cooling rates, or with higher carbon content, Figure 2.32(b) depicts how the δ/γ interface might propagate from the dendrite tip to its root, following the isotherms under equilibrium conditions. This would lead to axial shrinkage of the dendrite length in the solidification direction, which would not tend to cause any bending or tensile stress across the interdendritic region. Such microstructural effects should be explored as a potential mechanism for the increased bending and cracks observed in peritectic steels.

In addition to the importance of increased shrinkage on the behavior of peritectic steels, many researchers have noted that austenite is much stronger than delta-ferrite at a given temperature [119, 245, 246]. Advanced thermal-mechanical computational models have been applied to investigate the effect of steel alloy (carbon content) on thermal distortion of the bottom of solidifying steel droplets [247]. and on deflection of the tip of the solidifying steel shell during a level drop in a continuous casting machine near the meniscus [119, 245].

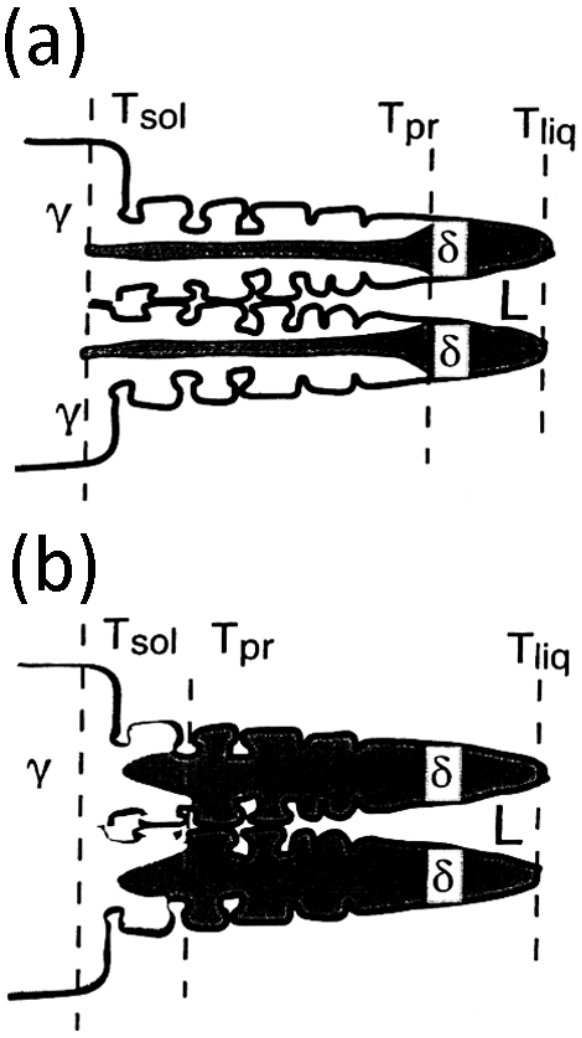

Figure 2.32. Schematic of different directions of the peritectic transformation, (a) transverse shrinkage at high cooling rates or carbon starved (peritectic), which leads to depressions and cracks; (b) axial shrinkage at low cooling rates or high carbon, C> 0.2 pct which leads no problems [244].

These models include the temperature, phase fraction, and composition dependency of both the steel density (and corresponding shrinkage) and the strength, using an elastic-viscoplastic constitutive relation. The predictions of these models match the observed trends of increased bending deformation in ULC and peritectic steels. Sample results, shown in Figure 2.33, reveal

that these steels experience deeper depressions, which become much more severe with level fluctuations [119, 245].

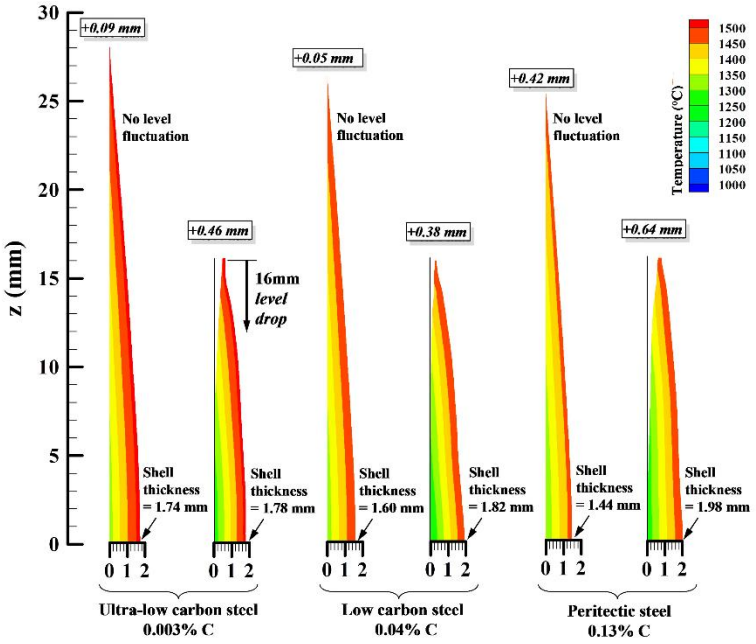

Figure 2.33. Simulated shell tip distortion for three steel grades with and without level fluctuations, showing increased depressions in ULC and peritectic steels. Reprinted with permission from reference [119].

2.5.4 High Temperature Ductility and Hot Tearing

Cracks form during commercial casting processes due to a combination of metallurgical embrittlement and tensile stress. Most longitudinal surface cracks and internal cracks are caused by a hot tearing mechanism during initial solidification that involves severe embrittlement and failure strains of only about 1 pct. Steel composition plays a critical role, in part because it controls the high-temperature ductility. Many studies have been conducted on steel ductility, as reviewed elsewhere [248-250], so only a few points relevant to peritectic steels are emphasized here.

Metallurgical properties during solidification are shown schematically in Figure 2.34. Above the Zero Strength Temperature, (ZST), the steel behaves like liquid, and any applied tensile strain will simply pull apart the dendrites, and draw liquid in to fill the space. Below the Liquid Impenetrable Temperature (LIT), the feeding of bulk liquid is prevented by the dendrite network. Below the Zero Ductility Temperature, (ZDT) or non-equilibrium solidus temperature, solidification is sufficiently complete that the solid can withstand significant load and ductility is high. Between LIT and ZDT is a brittle temperature range that is susceptible to hot tearing. Others suggest a brittle temperature range between the Zero Strength Temperature (ZST) and ZDT [251]. In these critical temperature ranges, strength is low due to the liquid matrix, so any applied tensile strain will open up a crack, which is filled by drawing in surrounding segregated liquid. Strain sources include mechanical deformation, thermal contraction and the δ/γ phase transformation. The typical solid fraction between LIT and ZDT is 0.9 to 0.99, which extends with increasing cooling rate, to below the equilibrium solidus temperature [120, 252].

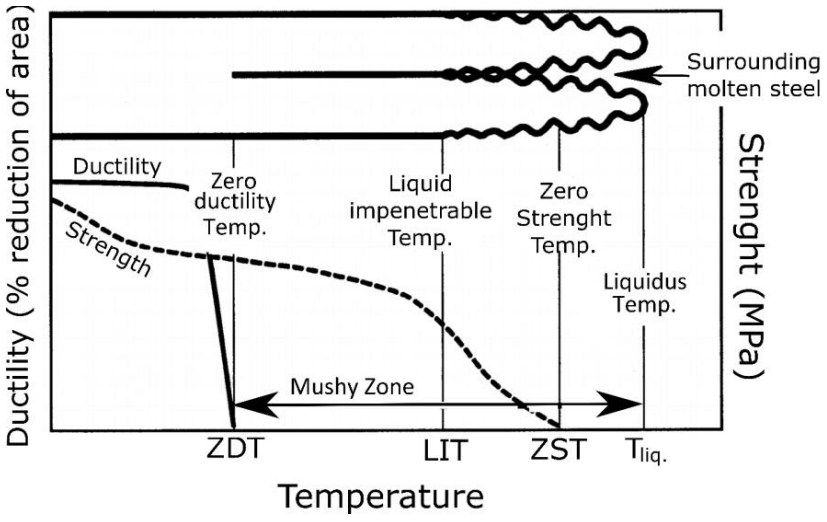

Figure 2.34. Schematic of temperatures relevant to high-temperature embrittlement and hot tearing cracks during steel solidification. Reprinted with permission from reference [55].

Many researchers have investigated the important effect of alloying elements on high-temperature steel ductility [55, 253-259]. Residual impurity elements, such as S, P, Cu, Sn, Sb, and Zn, are well known to be detrimental because they segregate into the interdendritic liquid, lowering the ZDT and thereby decreasing the failure strain [55, 250]. Many of these elements have low partition coefficients, leading them to concentrate in the austenite phase [11]. Phosphorus, for example, segregates during solidification to austenite over 10 times more than when solidifying to ferrite [11]. Alloys which undergo the peritectic reaction, change their solidification mode from ferritic to austenitic, leading to more segregation, lower ZDT, and lower high-temperature ductility.

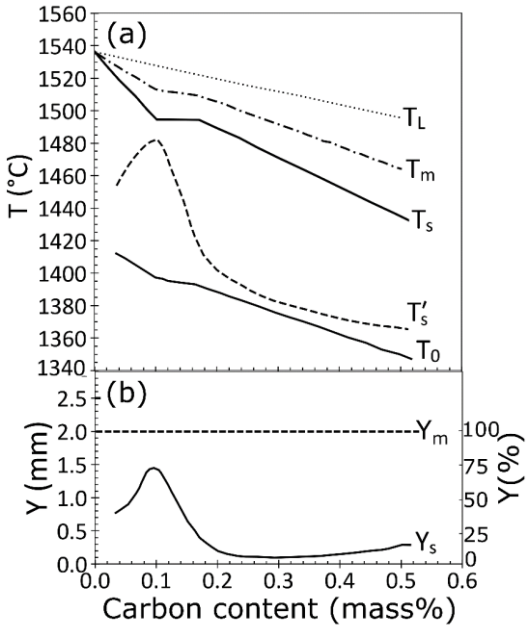

Figure 2.35. Influence of C-content on (a) characteristic temperatures in the strand shell and (b) assumed constant planar interface position, Y_m, and effective shell thickness, Y_s, considering P-segregation. Reprinted with permission from reference [11].

Alloys with higher segregation have lower non-equilibrium solidus temperature ($T_s^{'}$) and consequently have thinner effective shell thickness, that is completely solid with mechanical strength. Figure 2.35 shows that the peritectic steels (0.1 pct C) have the highest effective shell thickness, while high carbon steels suffer the most embrittlement and are thus more prone to hot tear cracks [11]. However, the thicker effective shell of the peritectic steels experiences more bending and being stronger, can support a higher ferrostatic pressure, thus leading to deeper surface depressions. Consequently, increased interfacial gap resistance, leading to lower heat flux in the mold decreases the shell growth locally and creates hot spots, so increases the risk of surface crack formation and breakouts [26, 110, 118, 120, 124, 125].

2.5.5 Internal Cracks

Internal cracks are one the most important problems affecting commercial steel casting processes, such as continuous casting. These cracks form due to hot tearing as a result of tensile stresses which are induced by mechanical deformation, thermal contraction and phase transformation, combined with the loss of hot ductility near the solidus temperature discussed in the previous section. They are generally not actually cracks, because interdendritic liquid is drawn in between the separating dendrites to prevent an actual void. However, this results in a region of macrosegregation in the shape of the crack. This macrosegregation is a worse product defect than a void, because it cannot be closed or otherwise removed by rolling or other subsequent operations. It is important to note that during initial solidification, the mushy zone is at the surface of the steel strand, so surface cracks, especially longitudinal surface cracks, can initiate at the meniscus due to the same high-temperature embrittlement and hot tearing mechanism as internal cracks.

Many investigations on cracks due to hot tearing during casting of steel alloys have been conducted and are discussed in this section. Different criteria for hot-tear crack formation have been proposed, including critical strain [55, 251, 260-264] and critical fracture stress [265, 266]. Critical strain for internal crack formation have been reported to range from 0.5 to 3.8 pct [251, 262, 267, 268], or from 1.6 to 2 pct [269, 270], depending on the steel composition. One critical strain criterion for peritectic steel (0.14 pct C) suggests a critical temperature range of $T_a - 30 <$ T(K) < T_a where T_a is the 0.85 solid-fraction temperature [262]. Increasing strain rate is reported to decrease the critical failure strain [271], perhaps because it lessens the time available for liquid feeding [55] Won suggests the following critical strain criterion for hot tear cracking of plain carbon steels, based on an empirical fit of many measurements [55]:

$$\varepsilon_c = \frac{0.02821}{\dot{\varepsilon}_C{}^{0.3131} \Delta T_B^{0.8638}} \tag{2.26}$$

Where ε_c is the critical strain which when exceeded locally causes a hot tear; $\dot{\varepsilon}_C$is the local strain rate; and ΔT_B is the critical temperature range for the alloy, corresponding to the solid fraction range of 0.9 to 0.99 pct solid, which equals LIT - ZDT. Because strain and strain rate are tensors with different components which accumulate with time, attention should be paid to their directions, which could differ [272]. It should be noted that this criterion predicts that high carbon and high alloy steels with high solidification temperature ranges (and large ΔT_B) experience smaller critical strains, so are easier to crack. In contrast, peritectic steels experience smaller solidification temperature ranges and smaller ΔT_B, so have higher critical strains, which agrees with the high-temperature hot ductility findings discussed in the previous section [55]. Higher strain rate also decreases the critical strain and makes cracks more likely, but is difficult to quantify.

Other researchers have suggested critical fracture stress in the mushy zone as a criterion for crack formation [128, 273-276]. The fracture stress of solidifying shell has been measured using submerged split chill tension testing method [265, 277]. According to this criterion, hot-tear cracks form in the mushy zone when the maximum principal stress exceeds the local tensile strength of the steel at that temperature [278]. Other researchers [279] using tensile testing at elevated temperature found that steels which undergo the peritectic reaction are more susceptible to crack formation, especially when the solidification experiences massive transformation, owing to the fast shrinkage contraction.

Another crack criterion is based on the difference of deformation energy in the brittle temperature range and is shown in Figure 2.36 as function of carbon content, along with an experimentally measured crack index [55]. Peritectic steels (0.12 pct C) are predicted to experience the largest tendency for cracking. This was attributed to the large δ/γ transformation strain during solidification leading to higher strain rates. High strain rates also decrease the critical strain for crack formation. These results have been confirmed by Bernhard et al [280]. These predictions agree with other research that suggests that steels with carbon content of 0.1 pct C to 0.14 pct C are more susceptible to internal cracking [121, 281, 282].

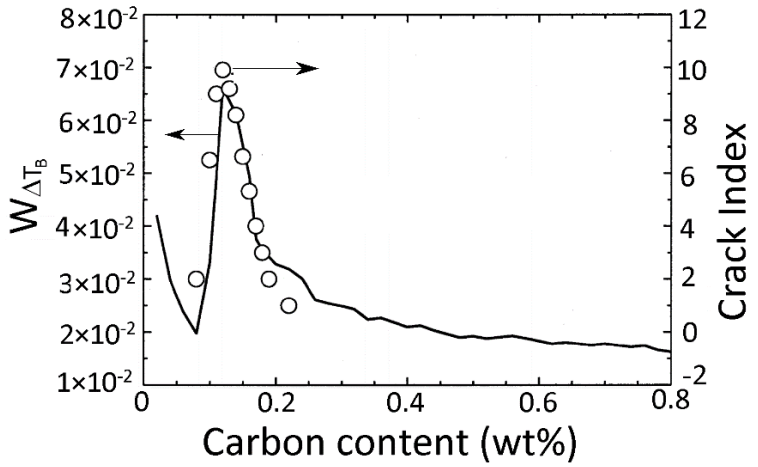

Figure 2.36. Effect of carbon content on experimentally-measured crack index and on difference of deformation energy in the brittle temperature range. Reprinted with permission from reference [55].

However, they appear to disagree with some of the critical strain predictions discussed earlier. This disagreement between different cracking criteria suggests that simple empirical relations are not easy to apply and that phenomena such as local shell thinning and strain concentration must be considered when predicting crack formation, as discussed in the next section.

2.5.6 Longitudinal Surface Cracks

Many studies [116, 127, 283, 284] have found carbon content to be the most critical factor which affects the formation of longitudinal surface cracks. Because they usually initiate during initial solidification near the meniscus, longitudinal surface cracks are governed by the same high-temperature ductility properties that govern internal cracks. In addition, they are greatly influenced by surface depressions, where strain can concentrate in the thin shell beneath them. Longitudinal surface cracks are formed most in the range of 0.09 - 0.18 pct C (hypo-peritectic range), as shown in Figure 2.37 [285].

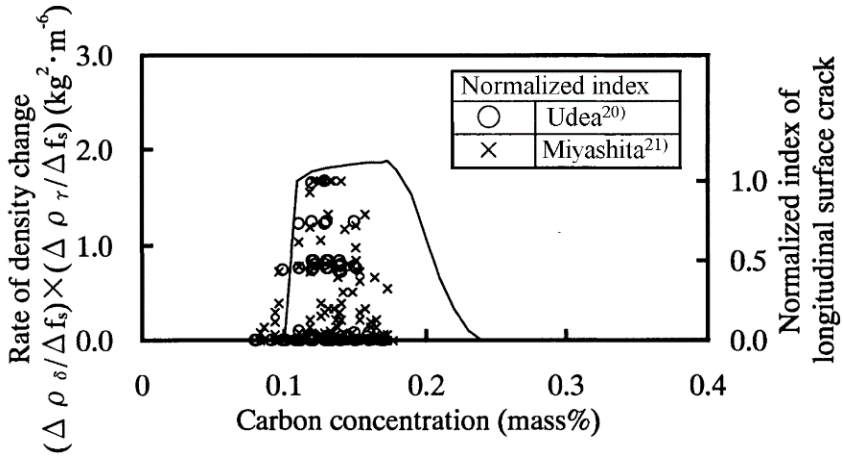

Figure 2.37. Effect of carbon content on longitudinal surface crack index. Reprinted with permission from reference [285].

This was attributed to the higher rate of shrinkage accompanying the δ/γ transformation, which can be represented by the corresponding density increase [285]. Despite having high shrinkage, longitudinal cracks do not formed as much above 0.18 pct C. This was suggested to be due to more liquid feeding available to compensate the shrinkage in these hyper-peritectic steels.

Other researchers [129] have investigated critical strain for crack formation in different steel grades using tensile and bending tests, and found that critical strain in peritectic steel is almost two times that of non-peritectic steels (Figure 2.38). Thus, the longitudinal surface cracks which form during the continuous casting of peritectic steels are not caused by higher intrinsic crack sensitivity of these steels, but rather by the hot spots at the base of depressions caused by the δ to γ phase transformation in the early stages of solidification.

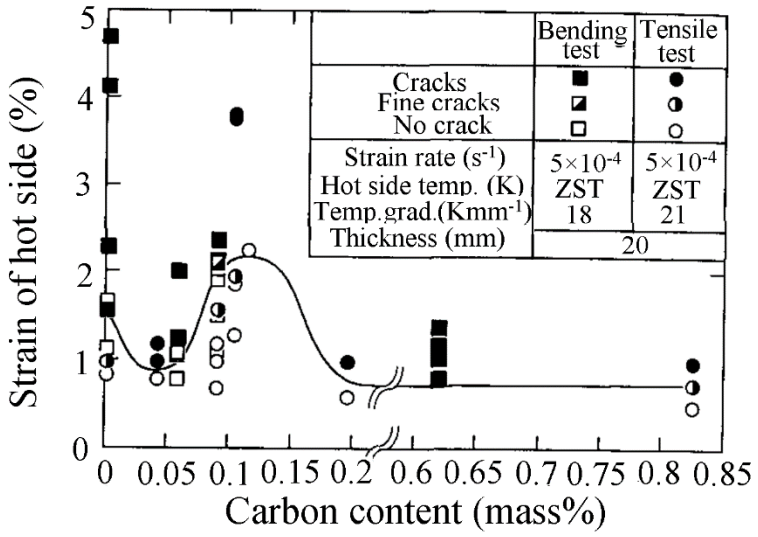

Figure 2.38. Effect of carbon content on the critical strain for crack formation. Reprinted with permission from reference [129].

2.5.7 Intermediate Temperature Ductility Drop, Austenite Grain Size, and Transverse Cracks

Many surface cracks, especially transverse cracks, arise due to tensile stress and embrittlement of the austenite grain boundaries at intermediate temperatures. A significant drop of ductility of steel at intermediate temperatures, from ~ 700 to above 900℃, has been the subject of many studies, reviewed elsewhere [254]. This ductility drop or "trough" is due to the formation of precipitates, including sulfides and nitrides, which weaken the austenite grain boundaries, especially when soft and weak primary ferrite nucleates on the boundaries to form ferrite films or networks. Embrittlement is much more severe when the austenite (γ) grains are very large, because any applied tensile strain concentrates within a small number of grain boundaries [259, 286-290]. Intermediate temperature ductility loss is important to transverse surface cracks, because they tend to form due to axial and unbending strain low in a continuous

casting machine, when surface temperatures often fall within the critical temperature range for the intermediate-temperature ductility trough.

It has been widely reported that transverse cracks form only in the presence of abnormally large austenite grains, where a film of ferrite or precipitate form along the boundaries [291-293]. These abnormally large grains are sometimes referred to as “blown grains”. Peritectic steels are reported to experience larger austenite grain size than steels with either lower or higher carbon content [294]. Austenite grain size increases rapidly with increasing temperature, due to grain growth, as shown in Figure 2.39 [293]. This figure also shows that near-peritectic steel (0.16 pct C) experiences grain growth earlier and eventually attains a larger size.

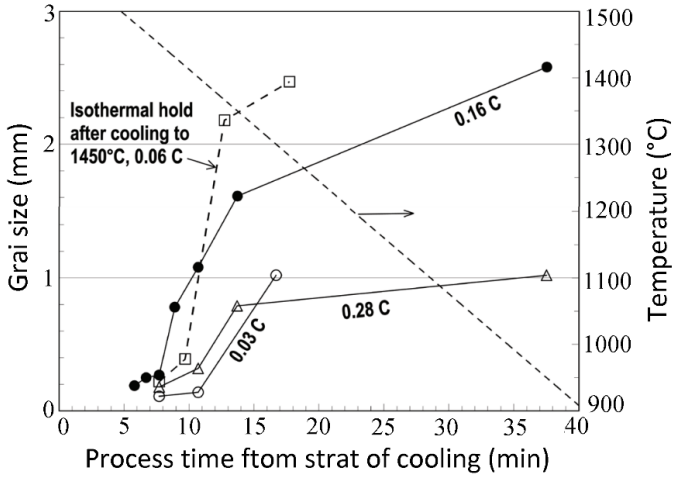

Figure 2.39. Austenite grain growth with temperature and carbon content (in-situ melted and cooled from 1580℃ to test temperature at 16.8℃/min). Reprinted with permission from reference [293].

Other researchers have confirmed that near-peritectic steels, such as 0.17 pct C, have larger austenite grain size than other steels, as shown in Figure 2.40 [287, 295]. It is suggested that [296] because liquid and delta ferrite hinder the growth of γ grains [297], austenite grains start to

grow immediately after transformation into the single phase γ region [297, 298]. Adding phosphorus to 0.1 pct C steel has been shown to decrease the primary austenite grain size [299, 300]. This was attributed to delaying the δ/γ transformation to a lower temperature range.

Austenite grain size can be predicted by:[301]

$$\overline{D} = 9.1 \times T^{\gamma} - 3152\left[\frac{e^{\dot{T}}}{1+e^{\dot{T}}}\right] - 9044 \tag{2.27}$$

where $\overline{D}$ is the final austenite grain size in μm; T^{γ} is the highest temperature of the totally austenitic region for the steel composition (℃), and $\dot{T}$ is the local cooling cooling rate ($℃/s$).

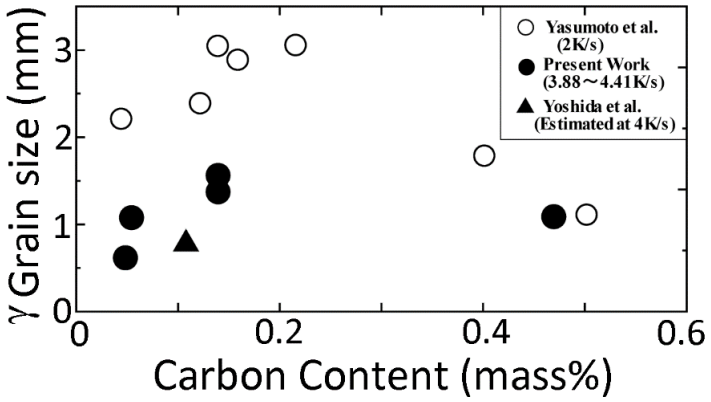

Figure 2.40. The γ grain size change by carbon content in terms of γ single phase temperature in Fe–C phase diagram. Reprinted with permission from reference [287].

Predictions at 3 different cooling rates for steels with different carbon contents and 0.3 pct Si and 1.5 pct Mn all match closely with measurements for similar grades, as shown in Figure 2.41 [301]. These results confirm that austenite grain size is larger in peritectic steels, with huge grains exceeding 1mm diameter in many cases.

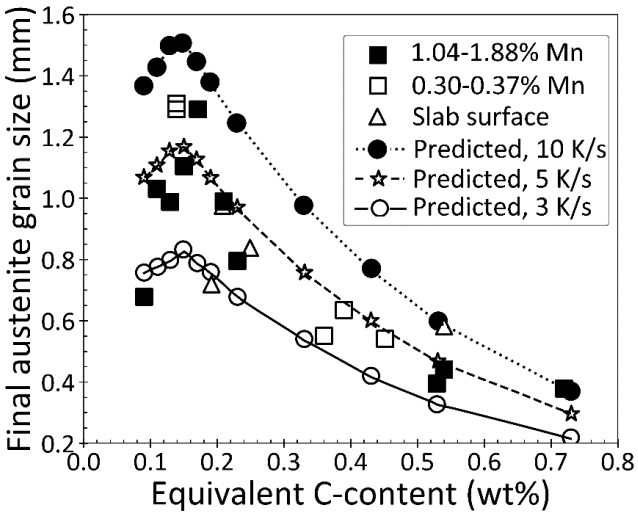

Figure 2.41. Measured and predicted austenite grain size vs. equivalent carbon content. Reprinted with permission from reference [301].

Transverse cracks are more severe with deep surface depressions and oscillation marks [295, 301-303]. This is expected because the greater interfacial resistance between the shell and the mold leads to lower heat flux, and a hotter, thinner, and weaker shell beneath the depression, as discussed earlier.

Heat transfer model calculations in Figure 2.42(a) show the expected temperature distribution near a group of deep oscillation marks. Surface temperatures beneath the oscillation mark can increase up to several hundred degrees hotter than the nearby steel surface, owing to the lower heat transfer, especially if the interfacial gap contains air [234]. The hotter surface causes a thinner and weaker shell, which matched thickness profile measurements on a breakout shell. The hotter surface also enables more grain growth, leading to coarse austenite grains and strain concentration in these areas, as shown schematically in Figure 2.42 [234]. Below the mold, spray cooling can make the strand surface temperature become more uniform, but cannot reduce the large austenite grain size on the surface.

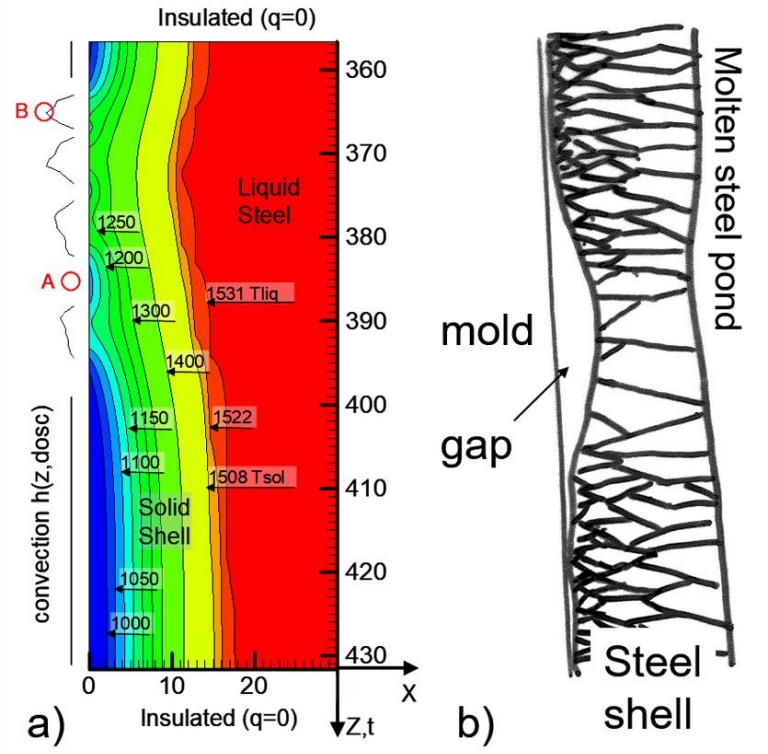

Figure 2.42. Closeup of solidifying steel shell in the mold showing (a) simulated temperature contours near a group of deep oscillation marks and (b) schematic of resulting grain structure leading to transverse cracks. Reprinted with permission from Reference [234].

In summary, transverse cracks are more common in peritectic steel than in other steel grades for two reasons. Firstly, the increased shrinkage of these steels causes deeper oscillation marks and surface depressions, which result in higher surface temperatures beneath the depressions. Secondly, austenite grain growth in these steels begins at higher temperature, leading to generally larger austenite grains beneath the surface depressions. Both effects lead to decreased intermediate-temperature ductility, increased strain concentration, and increased transverse crack formation in peritectic steels.

2.6 Conclusions

This paper summarizes current understanding of peritectic solidification of steel, and its important effects on commercial casting operations. Specific findings include:

- Several empirical relations are available to predict if a steel alloy will exhibit peritectic behavior according to its composition, especially carbon content. These include criteria based on carbon equivalent ranges, alloy-dependent critical points, ferrite potential, and CALPHAD methods. Although already successful, further work is needed, as different relations differ regarding the influence of some alloying elements, including Si, Cr, Ti, V, S, P, A, and Nb. The trends are clear for austenite forming elements Mn, Ni, Cu, and N and ferrite forming Mo.

- Fundamental mechanisms to explain peritectic solidification have been investigated using experiments which include calorimetry, diffusion couples, directional solidification, high-temperature confocal laser-scanning microscopy (HT-CLSM), and X-Ray imaging methods, and computational models which range from simple analytical diffusion equations to sophisticated phase-field simulations.

- Under equilibrium conditions, peritectic solidification proceeds in two distinct steps: the peritectic reaction, and the peritectic transformation.

- The peritectic reaction takes places when austenite nucleates and grows as a thin layer along the liquid / δ-ferrite interface at or just below the peritectic temperature. It is governed by diffusion of solute (carbon in plain Fe-C steels), especially in the liquid, and likely also depends on microscale heat transfer that causes local re-melting of δ-ferrite and liquid / solute mixing near the δ/γ/L triple point.

- The peritectic transformation first involves growth of the austenite layer thickness in both directions: into the liquid (L →γ) on one side, and into the δ-ferrite interior (δ→γ) on the other side, which separates the δ-ferrite and liquid by a thickening layer of austenite. Some believe that this transformation is controlled by diffusion, especially with low undercooling below the peritectic temperature. At high undercooling, the transformation is extremely fast, so others believe that the δ→γ transformation is controlled by massive transformation.

- At very high undercooling and transformation rates, some claim that the peritectic reaction is suppressed, due to either nucleation constraint, or to solute flux gradients, so the initial austenite layer never grows along the δ / L interface and the entire peritectic solidification process is governed by massive transformation.

- Peritectic steels cause deeper oscillation marks and surface depressions in cast products, relative to other steel grades. This is due to the large shrinkage that accompanies the δ→γ phase transformation, the higher transformation speed, the much higher strength of austenite relative to δ-ferrite, complex thermal-mechanical behavior during solidification, and possibly other factors involving the microstructure evolution.

- Peritectic steels having deeper surface roughness leads to higher resistance to heat transfer across the interfacial gap during initial solidification in the mold, lower heat flux, uneven shell growth, and thin regions in the solidifying steel shell, which have hotter local surface temperature. These thin, weak, hot spots lead to local strain concentration and make peritectic steels more susceptible to breakouts and hot-tearing cracks, especially internal cracks and longitudinal surface cracks, relative to other grades.

- Peritectic steels experience faster austenite grain growth at high temperature, which leads to lower intermediate temperature ductility. Together with the higher local temperatures found beneath oscillation marks and depressions, this makes peritectic steels more prone to cracks, especially transverse surface cracks.
- Many empirical indices and criteria have been developed to predict cracking due to hot tearing. Further research is needed, however, to better quantify both hot-tear crack formation and cracks related to intermediate temperature embrittlement before crack formation in peritectic steels (and other grades) can be accurately predicted.
- Although significant progress has been made in recent years, much further research is needed to confirm and quantify the mechanisms that govern peritectic solidification, how they are affected by composition and casting conditions, and how they can be controlled to improve final product quality.

Acknowledgements

The authors wish to thank the contributing companies of the Continuous Casting Center at the Colorado School of Mines for funding that enabled this research.

CHAPTER 3
PREDICTION OF THERMAL STRESS DURING STEEL SOLIDIFICATION

3.1 Abstract

Thermal distortion during the initial stages of solidification is an important cause of surface quality problems in cast products. In this work, a finite element model including non-linear temperature-, phase-, and carbon-content-dependent elastic–viscoplastic constitutive equations is applied to study the effect of steel grade and interfacial heat flux on thermal distortion of a solidifying steel droplet. Due to thermal contraction, the bottom surface of the droplet bends away from the chill plate and a gap forms. It is shown that, regardless of the nature of the heat flux, the gap forms and grows the most very early during solidification (~0.1s) and remains almost unchanged afterward. Increasing the heat flux decreases the time for evolution of the gap and increases its depth. When the carbon content is less than 0.10%C, the gap depth is very sensitive to the heat flux, but for higher carbon contents, this sensitivity is much weaker. The highest gap depths are predicted in ultra-low carbon (0.003%C) and peritectic steels (0.12%C), and agree both qualitatively and quantitatively with the experimental measurements. Thus, the current thermal-mechanical model, including its phase-dependent properties, captures the mechanism responsible for nonuniform solidification, depression sensitivity and surface defects affecting these steels.

Keywords: Solidification; Peritectic Steel; thermal distortion; thermo-elasto-viscoplastic model.

3.2 Introduction

Continuous casting technology is the primary method of producing semi-finished steel products, and over 96% of the world's steel is made using this process [8]. One of the most important features of continuously cast strands is their surface quality, which is mainly

controlled by initial solidification at the meniscus [9-11]. In this region, the solidifying shell is subjected to complicated thermal and mechanical loading conditions [12] which may lead to formation of surface defects such as depressions [13], oscillation marks [14, 15], and cracks [16, 17].

Understanding the root causes of surface defect formation is the main key to control the strand surface quality [116, 304, 305]. It is well known that steel grade is the most critical parameter that affects depression severity [11, 116, 120, 306]. Ultra-low carbon steels (<0.005%C) suffer from poor surface quality [12], and steels which undergo the peritectic transformation (~0.09 <%C< ~0.17) and experience "peritectic behavior" [307] exhibit the deepest surface depressions, with a peak in severity typically observed around 0.10%C [308, 309], depending on the other alloying elements [307]. Surface depressions during steel solidification are responsible for many other surface defects [310-313] and often have been attributed to the shrinkage associated with the δ-ferrite to austenite solid-state phase transformation [305, 314].

During continuous casting, initial solidification at the meniscus is influenced by many complicated transient phenomena such as mold oscillation [313], slag infiltration [315], movement of the slag rim [316], turbulent fluid flow [317], liquid surface level drops [318], liquid overflow of the shell tip [319], and surface tension effects [320], in addition to the high local heat flux and thermal distortion [116]. These all cause transient changes to the meniscus shape and affect the final shape of the surface of the solidified shell including surface depressions [12]. Thus, it is almost impossible to isolate the effect of thermal deformation due to phase transformation on the final surface shape. To this end, laboratory experimental methods have been developed to characterize the surface shape variations with steel grade during initial

solidification, such as the “dip test” [321] in which a copper chill block is immersed into a liquid steel bath for a short time. Visualizing and measuring the roughness of the thin steel shell that solidifies onto the plate provides an indication of the susceptibility of the steel grade to surface depressions during casting. Another simple experiment, the “droplet test”, was proposed by Dong and coworkers [322-324] in which a small liquid steel droplet is placed on a chill plate and the free deformation of the bottom of this droplet is measured. In spite of its differences with the actual production method, the effect of steel grade on the surface shape was found to match with experience in commercial continuous casters. Thus, the effect of thermal distortion on solidifying shell shape under a sharp temperature gradient can be isolated and studied using the droplet test.

Previously, the droplet test was used to investigate the effect of carbon content on free deformation during steel droplet solidification [323]. Small liquid steel droplets of 4-8 grams were levitated and dropped 35mm onto a water-cooled chill plate made of either graphite for slow cooling, or copper for fast cooling. After solidification and cooling to room temperature, the bottom surface of the droplets took a parabolically-curved shape, indicating that a gap formed between the bottom surface and the chill plate. The bottom surface of each solidified droplet was fitted to a parabola and the curvature was characterized with a single fitting parameter, N_d:

$$\text{gap} = N_d R^2, \tag{3.1}$$

where R is the horizontal distance from the center of the droplet bottom surface. The curvature of the bottom surface was measured for different grades and droplet sizes [323, 324]. It was found that the bottom surface curvature is controlled by the composition, with two peaks: at near pure iron (carbon content is almost zero) and at around 0.12%C. Positive curvature (gap increasing with R) was observed in all small droplets with < 0.6%C. In addition to steel grade,

the heat transfer rate between the solidifying droplet and chill plate has a great effect on thermal distortion. The measured curvatures of the droplet bottom surface solidified onto a copper chill plate are much larger than those on a graphite chill plate, especially with peritectic steels [323, 324]. This is because the average heat transfer coefficient at the steel shell/graphite chill plate interface is about one third of that at the steel/copper interface [323].

Several computational models of thermal-mechanical behavior of steel during initial solidification have been developed in previous works [272, 318, 325-335]. Analytical solutions of thermal stress during solidification have predicted air gap formation during the casting process, including the effects of mold taper and superheat, but these simple models neglect the effects of alloy solidification range, solid-state phase transformations, plasticity and creep [327, 328, 331]. Advanced computational models based on numerical methods such as the finite element method, are able to include these effects with realistic temperature-dependent thermal and mechanical properties. Several such models have investigated gap formation during steel continuous casting in the mold [272, 318, 333, 334, 336-343], and many of them have shown that shell shrinkage is greatest towards the mold corners, which generates large gaps between the shell and mold there [272, 334, 336-338]. These gaps become filled with mold flux [332, 338], leading to lower heat transfer [332], hot spots [333] and longitudinal depressions [336, 338] on the shell surface in the off-corner regions of the strand. Shell shrinkage in the mold was found to decrease with increasing casting speed, owing to the decreased time in the mold, leading to a hotter, thinner shell, [334] so less taper is required to compensate for the shrinkage [344].

Other such thermal-mechanical finite-element models have been applied to investigate sudden liquid level drops during the continuous casting process on thermal distortion of the shell during initial solidification and surface depression formation [318, 325]. These models showed

that shell tip distortion increases with increasing level drop and is largest for ultra-low carbon and peritectic steels [318, 325].

Parkman et al [326] simulated thermal distortion of solidifying steel droplets with an elastic-viscoplastic finite element model including the effect of phase transformation strains. Simulations showed that the gap forms and reaches its maximum depth at very early stages of solidification (within 0.1s). Based on temperature measurements during the droplet test [323], the heat transfer coefficient dropped suddenly from 17.8 to < 5 kW/m^2K. The transition was postulated to occur when the solid layer gained sufficient strength to support the ferrostatic pressure and bend away from the chill plate [322, 323]. Suddenly dropping the heat transfer coefficient in the simulation from 20 to 5 kW/m^2K after 0.05s was found to increase the droplet surface curvature (gap depth) [323]. Increasing the heat transfer coefficient or decreasing the transition time both increased the gap depth [323]. Similar to the experimental work in [323], their model investigation of the effect of carbon content on gap depth revealed two peaks at nearly pure iron (0.003%C) and 0.12%C (peritectic steel) [326]. However, despite predicting the gap depth trend with carbon content very accurately, the magnitude of the simulated gap depths (surface curvatures) [326] was much higher than measured [323].

The solid state $\delta \rightarrow \gamma$ phase transformation has been established to be the main cause of surface depressions and the associated surface quality problems in continuously cast steel products. However, no previous fundamental model appears to be able to quantitatively predict the steel surface shape under the heat transfer conditions of continuous casting. Accurate prediction of the severity of surface depressions for a specific steel grade under real conditions would enable appropriate action(s) to be taken at the caster to improve surface quality. The aim of this work is to study the effects of steel grade (carbon content) and heat flux conditions on

shrinkage and thermal distortion of a solidifying steel droplet. The same conditions as in the experimental droplet test [323] are used for the simulations, and predictions of the curvature of the bottom surface of the droplet are validated with the measurements. Furthermore, the effect on this behavior is investigated to reveal new insights into thermal distortion during initial solidification.

3.3 Model Description

The computational model used in this work to model initial thermal-mechanical behavior of steel during initial solidification, including the simulation domain, heat transfer model, stress model, and solution details are described in this section.

3.3.1 Model Domain and Boundary Conditions

Thermal distortion of a 4 gram steel droplet in two dimensions is simulated to represent the conditions of the experimental droplet test [323]. Since the geometry of the droplet and thermal loading (heat flux) are axially symmetric, a two-dimensional axisymmetric finite-element model is used to simulate the thermal-mechanical behavior of the solidifying droplet.

The simulation domain, highlighted with a red rectangle in Figure 3.1, represents a cylinder with 5 mm radius and 6 mm height. Heat flux is applied uniformly on the bottom surface and the other three surfaces are insulated. There is no mechanical constraint on the domain surfaces, so they can deform freely. Thus, the surfaces are stress free, except for a surface traction equivalent to the gravitational body force, $\rho g h$, applied on the bottom surface. This effectively pushes the thin solidifying steel shell towards the chill plate, according to the liquid pressure above it. Applying this pressure at the bottom avoids convergence problems associated with loading the weak liquid, while having negligible effect on the results.

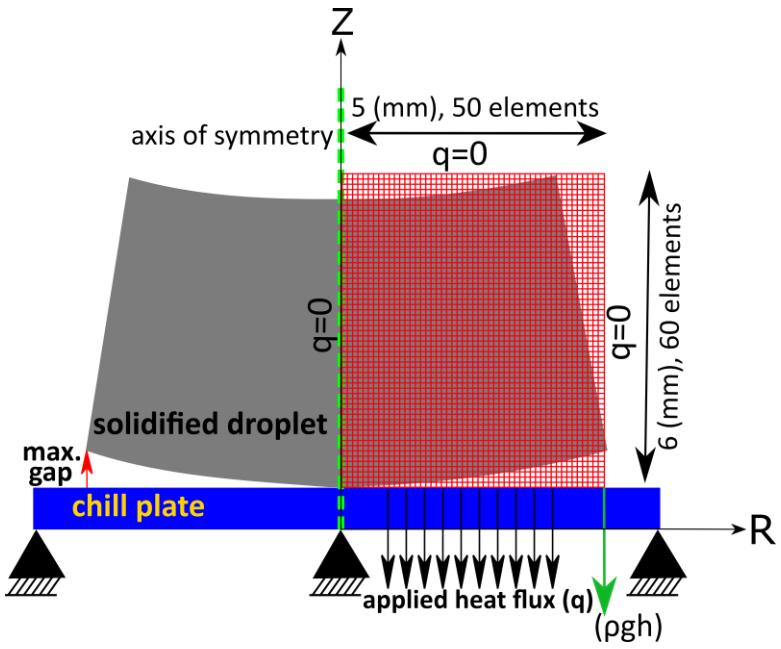

Figure 3.1. Cross section of the droplet showing the simulation domain (red rectangle) and boundary conditions.

3.3.2 Heat Transfer Model and Applied Heat Flux

The two-dimensional transient heat conduction equation is solved for the temperature field of the solidifying droplet in cylindrical coordinates:

$$\rho\left(\frac{\partial H}{\partial t}\right) = \nabla.(k\nabla T) \tag{3.2}$$

In this equation, ρ is temperature-dependent mass density, (kg/m^3) H is temperature-dependent specific enthalpy (J/kgK) which includes the latent heats of phase transformations, t is time (s), k is isotropic temperature-dependent thermal conductivity, (W/mK) and T is temperature (˚C).

Heat flux is applied on the bottom surface in Figure 3.1, and the other three surfaces are insulated. The initial temperature of the domain for each steel grade is set to be 10˚C above the

liquidus temperature (ie constant superheat) to facilitate fair comparison of steels with different carbon contents.

As a curve fit of measurements on typical slab casters, [335] instantaneous heat flux during continuous casting can be represented as a function of time by $\dot{q}_{standard} = \frac{6.36}{\sqrt{t+1.032}}$ (MW/m^2). This standard heat flux (SHF=$\dot{q}_{standard}$) and high heat flux (HHF=$2\dot{q}_{standard}$) conditions were used in this work to investigate the effect of heat flux during continuous casting on thermal distortion. On the other hand, the droplet test experiences a transition in heat flux (THF), where the heat transfer coefficient (h) in the heat convection equation ($\dot{q} = h\Delta T$) drops from 17.8 to less than 5 kW/m^{2}K at the solid shell/chill plate interface, once the solid shell starts to deform [324]. This sudden decrease of heat transfer coefficient is due to the formation of an air gap at the shell/plate interface between the solidifying steel shell and the chill plate. In order to compare the simulation results of this work with the measurements in [323], the instantaneous heat flux for the validation cases was set to suddenly drop from $3.2\dot{q}_{standard}$ to $\dot{q}_{standard}$ at t= 0.06s, which approximates the time when the solid shell starts to bend away from the chill plate.

3.3.3 Stress Model

During solidification, strains are in the order of only a few percent, so it is reasonable to adopt the small strain assumption. The mechanical behavior of the solidifying steel droplet is governed by the quasi-static momentum balance equation:

$$\nabla . \underline{\underline{\sigma}} + b = 0 \tag{3.3}$$

where $\underline{\underline{\sigma}}$ is the second-order Cauchy stress tensor, and b is an applied body force which is equal to zero in this work [272, 335].

The total strain rate is divided into elastic ($\dot{\varepsilon}_{el}$), inelastic ($\dot{\varepsilon}_{ie}$), thermal ($\dot{\varepsilon}_{th}$), and fluid strain ($\dot{\varepsilon}_{fl}$) components.

$$\dot{\varepsilon} = \dot{\varepsilon}_{el} + \dot{\varepsilon}_{ie} + \dot{\varepsilon}_{th} + \dot{\varepsilon}_{fl} \tag{3.4}$$

where inelastic strain includes the effects of time-independent plasticity and creep. The fluid strain is the inelastic strain generated while the steel is liquid. Fluid strain represents a measure of liquid feeding to accommodate thermal shrinkage of the solidifying shell. Stress and strain are related by phase-dependent unified constitutive equations. The liquid phase is considered as a perfectly-plastic material with elastic modulus of 1GPa, Poisson's ratio $\nu = 0.3$ and σ_{yield} =10 kPa. The δ-ferrite phase is modeled with the Zhu modified power law [345], and the austenite phase uses model III from Kozlowski [346]. Further details on the formulation of this thermal-mechanical finite-element model are given elsewhere [272, 335].

3.3.4 Phase Fractions and Thermal Properties

In this work, six steel grades with different carbon weight percent of 0.003%, 0.05%, 0.10%, 0.12%, 0.16 % and 0.23%, were examined. The mass fractions of liquid, δ-ferrite, and austenite (γ) for each steel are calculated as a function of temperature and steel composition, using the lever rule, as plotted in Figure 3.2. The phase diagram used in this work is a pseudo-binary phase diagram which is constructed based on 15 points in temperature-composition space that changes with alloying elements [272]. A rule for multicomponent ternary systems is applied in the non-equilibrium three-phase region [335] . In this model, complete mixing of solute elements in the liquid phase and local equilibrium at liquid-δ, liquid-γ and δ-γ interfaces is assumed to calculate phase fractions. Thus, non-equilibrium thermal undercooling effects are neglected.

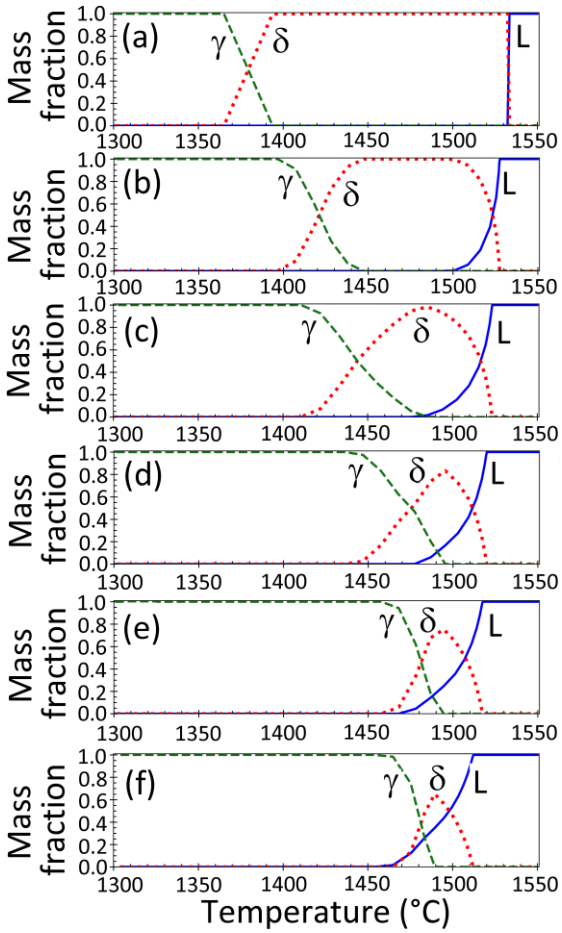

Figure 3.2. Phase fractions for six steel grades examined with different carbon content: (a) 0.003%C, (b) 0.05%C, (c) 0.10%C, (d) 0.12%C, (e) 0.16%C, and (f) 0.23%C.

Temperature dependent properties include thermal conductivity, enthalpy, mass density and thermal linear expansion, as shown in Figure 3.3, and are calculated using the method presented by Li and Thomas [272]. In mixed phase regions, specific heat, thermal linear expansion, and enthalpy are calculated using a weighted average (mixture rule) based on the mass fraction of the phases present at that temperature [272]. The thermal linear expansion (TLE) function for each phase is obtained from measurements of the solid-phase mass density [335, 347] and liquid density [348]. Further details on the TLE calculation can be found elsewhere [335].

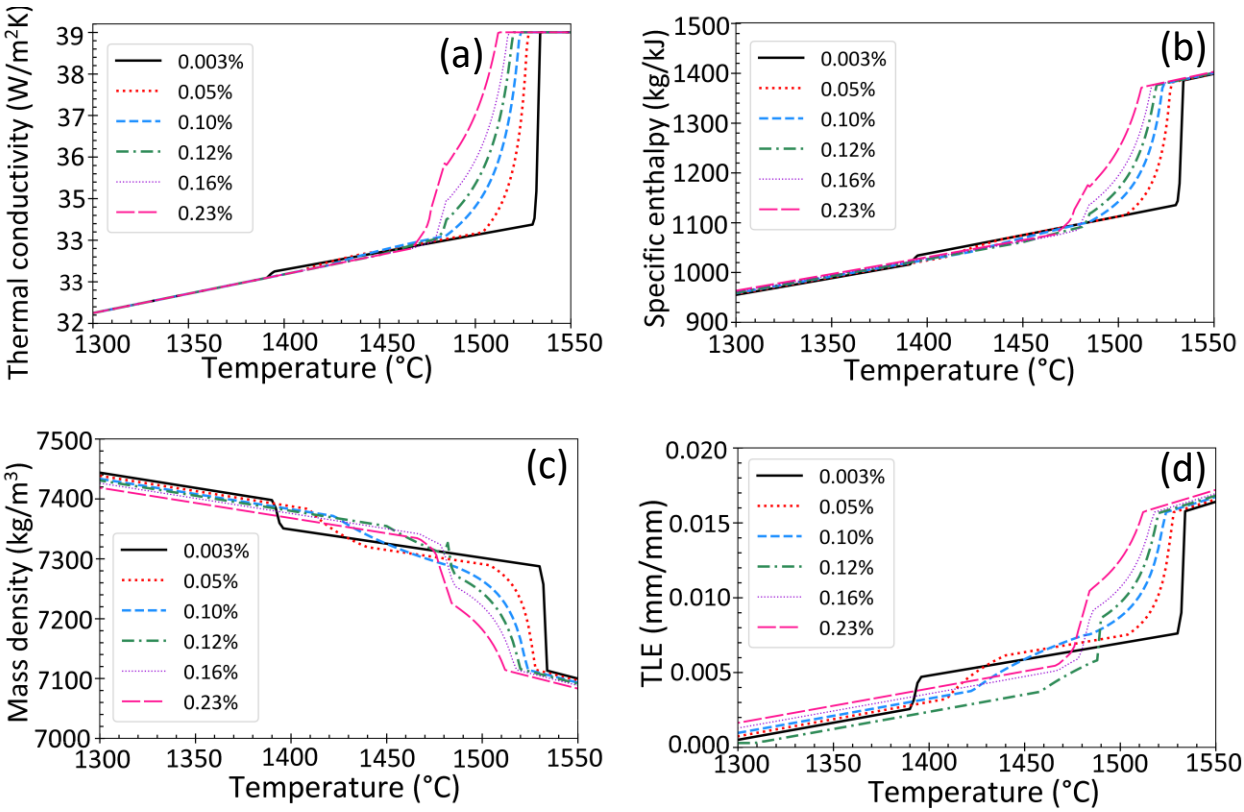

Figure 3.3. Temperature-dependent properties of six steel grades investigated: (a) thermal conductivity, (b) specific enthalpy, (c) mass density, and (d) thermal linear expansion.

3.3.5 Numerical Details

ABAQUS/Standard (implicit) [349] was used to solve the governing equations in two steps: the heat transfer analysis followed by the mechanical analysis. The ABAQUS user subroutine DFLUX [350] was used to apply the heat flux boundary condition. The calculated temperature field at each time step is an input to the mechanical analysis to calculate the thermal strain. Four-node axisymmetric convection/diffusion quadrilateral elements (DCCAX4) and 4-node hybrid, bilinear axisymmetric quadrilateral, constant pressure elements (CAX4H) were used for the thermal and stress analyses, respectively. The time step size varied from 0.0001 to 1 second, and was controlled to keep the maximum temperature change per time step within 50 K.

3.3.6 Mesh Resolution and Model Verification

The finite element mesh, shown in Figure 1, consists of 50 × 60 elements, with a constant element size of 0.1 mm. This mesh refinement was chosen based on a convergence study conducted for temperature, stress and distortion results for low-carbon steel. In this study, LC steel (0.05%C) with standard heat flux was simulated with different element sizes, (1, 0.5, 0.2, 0.1, and 0.05 mm), keeping the element aspect ratio (in radial r and height z directions) fixed at 1 (square elements).

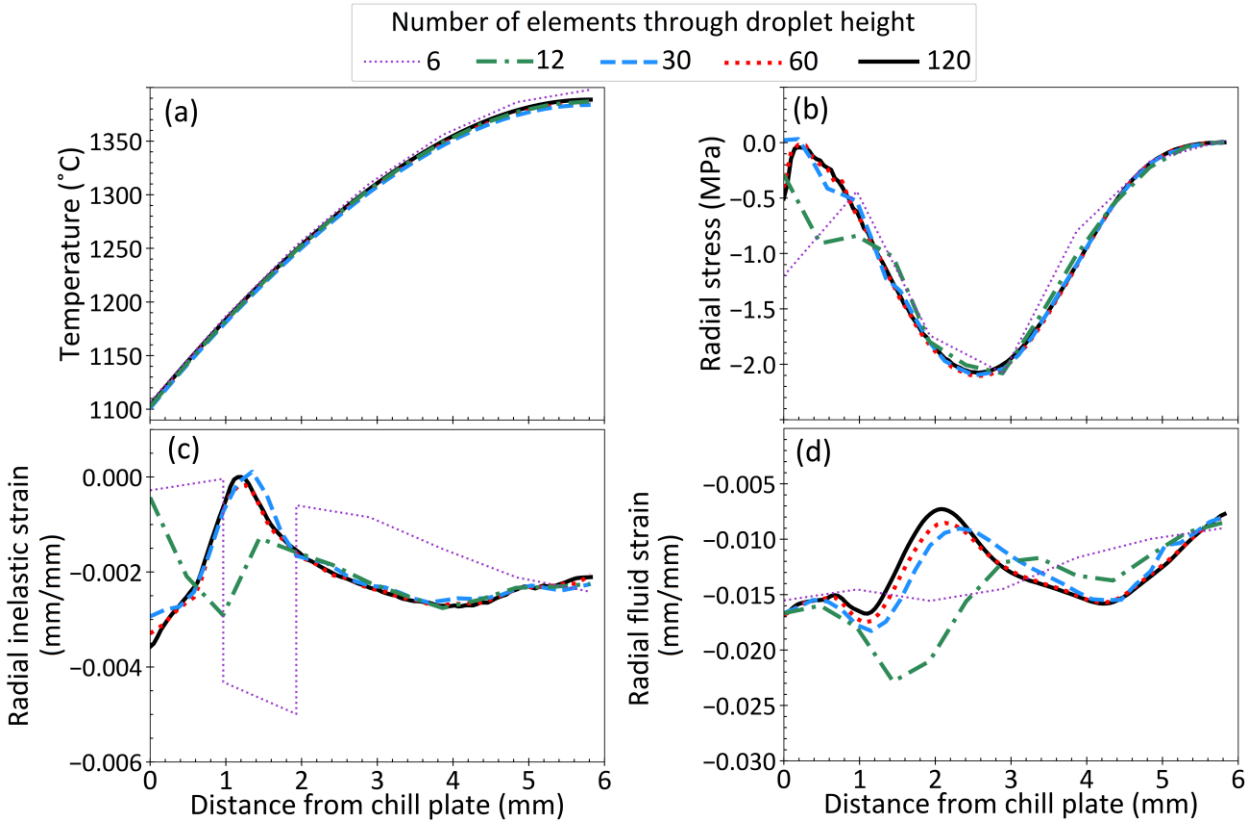

Figure 3.4. Mesh convergence study results through droplet height for low-carbon steel (0.05%C) at 5 s: (*a*) Temperature, (*b*) Radial-stress, (*c*) Radial inelastic strain, (*d*) Radial fluid strain.

Figure 3.4 shows results for the five different mesh refinements after 5 seconds of solidification. Although larger elements (1, 0.5, and 0.2 mm) can accurately reproduce the temperature history, shown in figure 3.4(a), a much more refined mesh is needed to resolve the stress and strain behavior, shown in figure 3.4(b)-(d). The inelastic strain results, shown in figure 3.4(c), are the least accurate, especially near the chill surface. Only meshes with 0.2-mm elements or smaller (60 and 120 elements through droplet height) predict the strain profile accurately. Results for these meshes with 0.1 mm and 0.2 mm elements all match everywhere within 1%. Thus, the 50×60 element mesh, with 0.1 mm elements, was chosen for the rest of this work. The model was also verified with the well-known analytical solution for thermal stress during unconstrained plate solidification by Boley and Weiner [351], as documented elsewhere [335].

3.4 Results and Discussion

Carbon content and cooling conditions are investigated here as the main factors that influence thermal distortion during steel solidification. The effects of these parameters on temperature distribution, stress distribution and gap formation during solidification of the steel droplet are discussed in the next sections.

3.4.1 Temperature Distribution

Figure 3.5(a) shows temperature profiles through the droplet height after 1s of solidification for different carbon contents and heat fluxes. For a given heat flux profile, it can be seen that the temperature profile through the droplet for all the examined cases is almost the same with temperatures within ~ 15˚C. This demonstrates how steel grade has little direct effect on properties and heat transfer, for the same gap profile. Also, it is evident that the temperature gradient with HHF is much steeper than SHF and THF after the transition to lower heat flux. At

very early times (≤ 0.06 s), the temperature gradient with THF is steeper. Figure 3.5(b) shows temperature evolution of the bottom surface for different heat flux profiles, choosing 0.003%C steel as representative. With SHF and HHF, the surface temperature decreases continuously with time, while with THF, the bottom surface temperature increases by 94˚C after the drop in the heat flux. This reheating of the bottom surface takes place because the heat from inside the droplet is conducted to the surface faster than it can be removed. This demonstrates that such recoalescence behavior can be explained solely by the droplet surface lifting up from the chill plate, and does not require nonequilibrium undercooling during solidification (which is neglected in the current model).

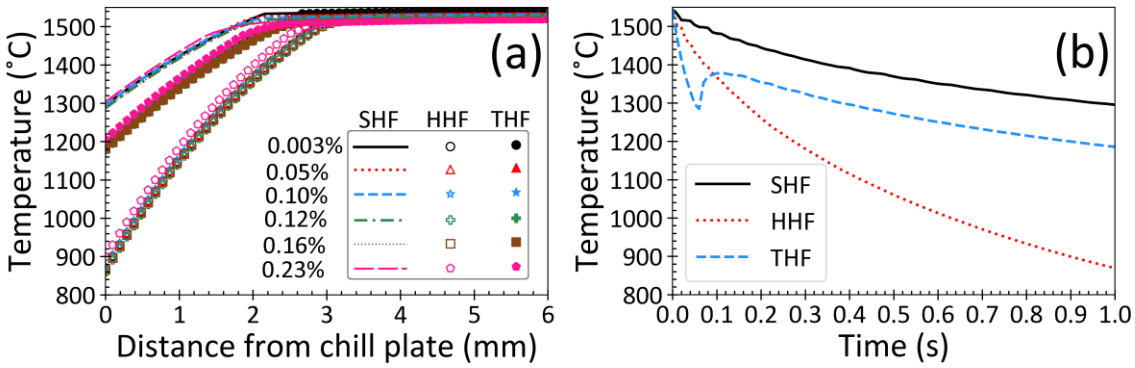

Figure 3.5. Temperature profile through the droplet height after 1s of solidification for six steel grades and different heat fluxes, and (b) change of bottom surface temperature with time for steel with 0.003%C and different heat fluxes.

Table 1 presents phase transformation temperatures for the 6 investigated alloys, in addition to the time when the bottom surface reaches the solidus and δ→γ transformation temperatures, the droplet solidification time when the top surface reaches the solidus temperature, and the incubation time (introduced in section 3.5). It takes 18s, 8s and 17s for the bottom surface to reach 300 ˚C (end of simulation) for the SHF, HHF and THF cases.

Table 3.1. Phase transition temperatures and times when droplet surfaces reach these temperatures for six investigated steels at different cooling conditions.

Carbon Content (wt%)	Liquidus Temp. (°C)	Solidus Temp. (°C)	δ→γ Transformation Start Temp. (°C)	Heat Flux Case	Time bottom surface reaches Solidus Temp. (s)	Time bottom surface reaches δ→γ Temp.(s)	Incubation Time (s)	Time top surface reaches Solidus Temp. (s)
0.003%C	1532	1532	1393	SHF	0.01	0.38	0.40	4.3
				HHF	<0.01	0.08	0.05	2.4
				THF	<0.01	0.02	0.01	3.2
0.05%C	1528	1500	1445	SHF	0.05	0.19	0.52	4.7
				HHF	0.01	0.04	0.15	2.7
				THF	<0.01	0.02	0.06	3.3
0.10%C	1525	1480	1481	SHF	0.09	0.09	0.30	4.8
				HHF	0.02	0.02	0.10	2.7
				THF	0.01	0.01	0.04	3.6
0.12%C	1521	1479	1494	SHF	0.08	0.05	0.26	4.8
				HHF	0.02	0.01	0.07	2.7
				THF	0.01	<0.01	0.03	3.7
0.16%C	1519	1470	1494	SHF	0.09	0.04	0.28	4.8
				HHF	0.03	0.01	0.08	2.8
				THF	0.01	<0.01	0.04	3.8
0.23%C	1514	1463	1491	SHF	0.12	0.03	0.57	5.8
				HHF	0.03	0.01	0.21	2.9
				THF	0.01	<0.01	0.06	3.8

With THF, the sudden drop in heat flux which accompanies gap formation results in surface reheating, thermal expansion of the surface layer, and a very large increase in the gap depth for all steel grades. The average heat transfer coefficient can be extracted from these results, based on the bottom surface temperature in figure 3.5(b) and choosing a chill plate temperature, such as 200˚C. From the instantaneous heat flux, $\dot{q}=h\Delta T$, the average heat transfer coefficient, h, in the first 1s is calculated to be 4.4 kW/m^2˚C for SHF and 11.4 kW/m^2˚C for HHF. With THF, h drops from 16.8 to 4.7 kW/m^2˚C after the first 0.06 s, which is very similar to the experimental measurements for pure iron [323].

3.4.2 Stress Distribution

Radial stress profiles through the droplet height at different times are presented in figure 3.6(a) for the 0.10%C steel and HHF cooling conditions. After 1s of solidification, slight tension is generated along the droplet surface due the cooling shrinkage, and the interior is under slight compression. This may increase the risk of surface crack formation and this issue is more severe in peritectic steels.

With further cooling to 2s, the stress profile reverses to compression along the bottom surface and tension in the interior. This reversal to the classic solidification stress profile is due to the most recently solidified steel towards the interior cooling and shrinking faster than the surface, as explained in previous work [335]. This stress profile naturally produces thermal distortion and gap formation that exhibits positive curvature of the droplet bottom surface.

At the end of solidification, at ~5s for HHF, both the top and bottom surface layers are under compression with a balancing tension in the central part of the droplet. The average stress

through the cross section must always equal zero, as the droplet exterior is unconstrained. Further cooling increases the stresses, but causes little further thermal distortion and gap depth increase, owing to the tension at the top surface being similar to that at the bottom.

Figure 3.6(b) compares the final stress state after the bottom surface temperature reaches 300˚C for the different steel grades for both SHF and HHF conditions (ie. 18s for SHF and 8s for HHF). The HHF case generates the maximum compression at the bottom surface, that is 50% more than that of the SHF case. Furthermore, the maximum tension in the interior with HHF is almost 150% greater than with SHF. These results show that increasing heat flux increases stress gradients in the droplet.

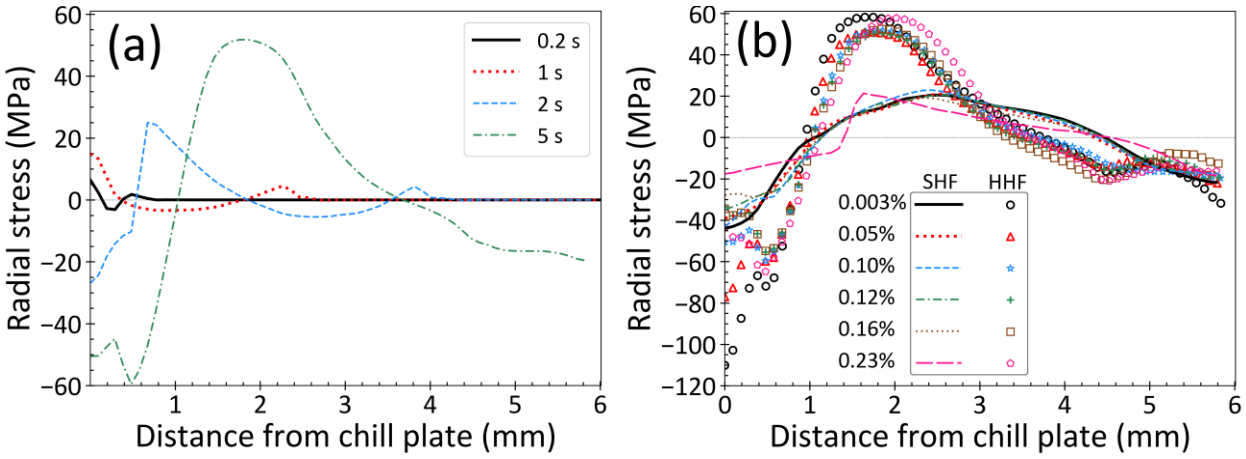

Figure 3.6. Radial stress profiles through the steel droplet (a) Evolution with time for 0.10%C steel with HHF, and (b) Final profiles at 300˚C for six examined steels and different heat fluxes.

3.4.3 Strain Distribution

Figure 3.6 shows the final radial strain distribution through the droplet when the bottom surface is 300°C. With no external load except gravity, the strains are all very small and thermal strain dominates the mechanical behavior. This strain is entirely shrinkage (negative), and

increases towards the droplet bottom surface to a maximum of 2.4%. The strain needed to accommodate fluid flow is also very important and reaches almost 1% as liquid is pushed out of and into the domain. Initially, the radial fluid flow is positive, as radial shrinkage from solidification decreases the cross-sectional area of the droplet and squeezes liquid upward. Later, the radial fluid flow becomes negative, as cooling and general shrinkage of the droplet draws liquid back down into the middle of the domain. This fluid flow is responsible for macrosegregation, which is obviously tiny in a droplet with such small strains. The mismatch between thermal strains causes inelastic strains, which although they are tensile, are also small, < 0.2%, so cracks, even hot tears, will not happen. The mismatch also causes elastic strains, which are very small, but critical, because they are directly responsible for the stresses. Creep lessens the elastic strains with time, but time is short, which partly explains why inelastic strains are small. Elastic and inelastic strains are also small because the shell can bend to accommodate them, rather than building up strain and stress which occurs in larger castings which have more constraints.

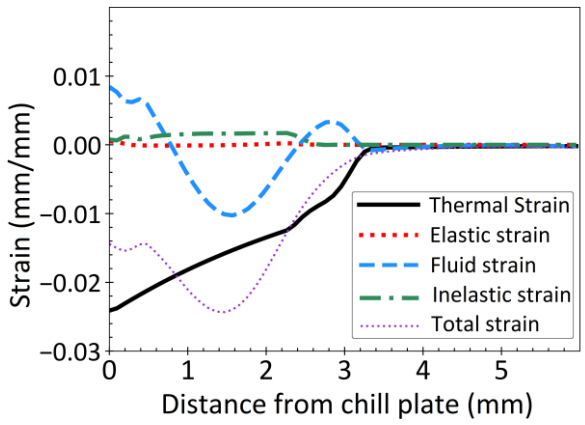

Figure 3.7. Final radial strain profile through droplet at 300°C for 0.10%C steel.

3.4.4 Thermal Distortion and Model Validation

Figure 3.8 shows the gap depth profiles of the solidified droplet for the six steels investigated for the three different heat flux conditions. The shape of the bottom surface in all cases is a parabola with different positive curvatures. The gap depth is largest in the peritectic steels, especially those containing 0.10%C and 0.12%C, with 0.16%C almost as deep. The ultra-low carbon steel (0.003%C) also experiences a very deep gap, especially with HHF. The low-carbon steels (0.05%C) and high-carbon steels, 0.23%C, consistently have shallow gaps. This trend of gap depth change with carbon content agrees with the experimental measurements [116, 310].

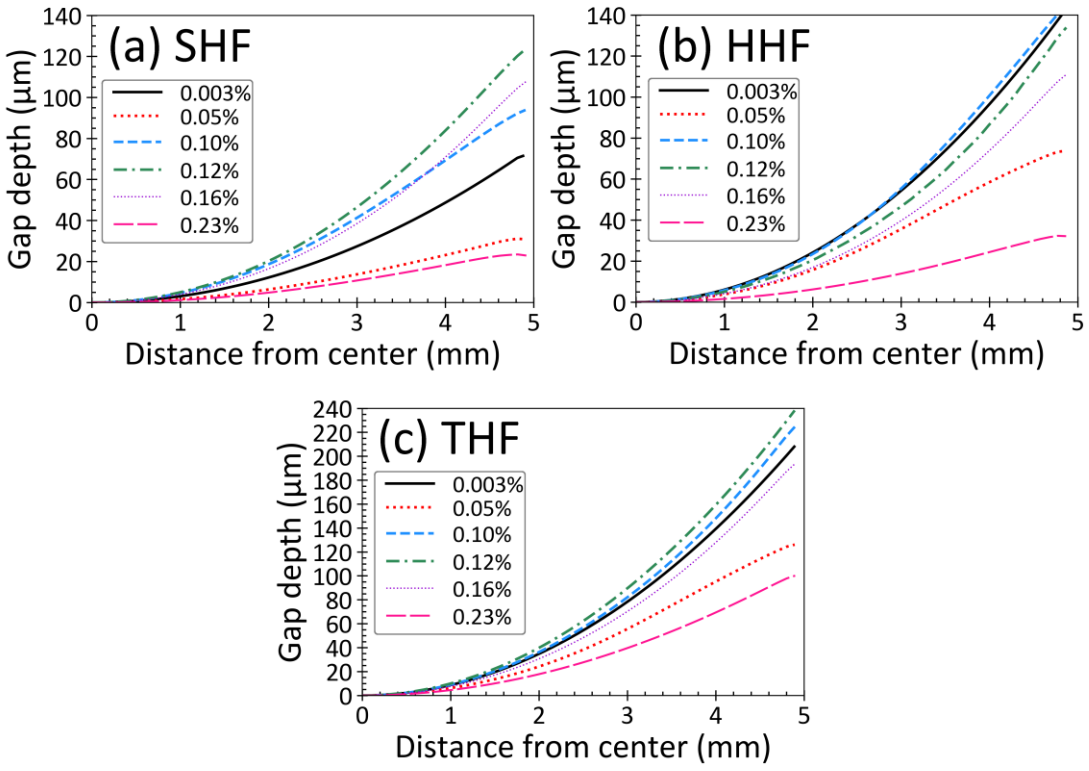

Figure 3.8. Gap depth profiles for six steel grades investigated and different heat fluxes at time when bottom surface temperature is 300˚C: (a) SHF (b) HHF and (c) THF.

Figure 3.9 compares the simulated curvatures of the bottom surface, (N_d in Eq. 3.1 fitted from the results in figure 3.8 in this work), with the droplet test measurements on the copper and graphite chill plates [323]. The simulated results with THF, which correspond closely with the experimental heat flux conditions on the copper chill plate (Exp-cc), match very well with the measurements, both qualitatively and quantitatively. In addition, the model predictions at lower cooling rate, SHF, match reasonably well with the experimental measurements on the graphite chill plate (Exp-gc). Of greatest significance, the model accurately captures the complicated trend with steel grade, where thermal distortion of the droplet bottom surface is greatest for peritectic and ultra-low carbon steels.

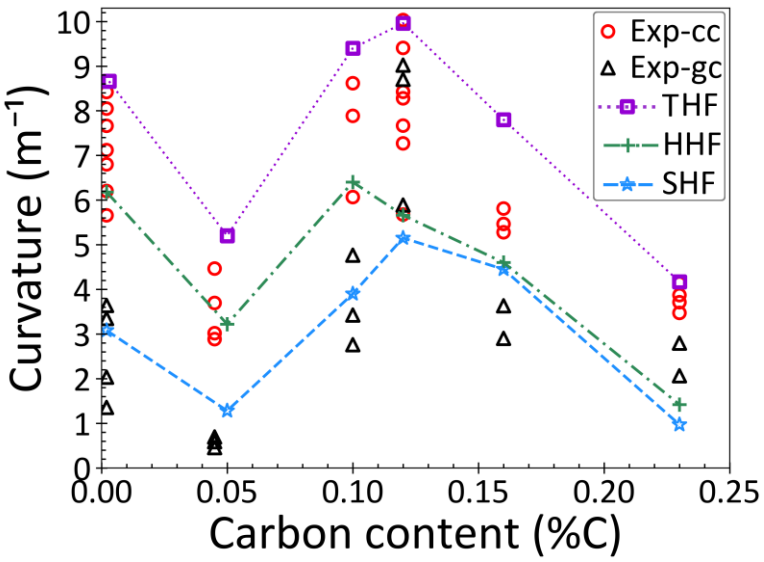

Figure 3.9. Comparison of predicted and measured droplet distortion for six steel grades investigated with different heat flux profiles.

It should be noted that the experiments were repeated several times for each steel grade, and the measured curvatures exhibit significant variations, most likely due to variability in the

heat flux conditions. Nevertheless, the agreement demonstrates that the current computational model captures the phenomena that govern thermal distortion during initial solidification, and that determine the shape of the final surface during steel casting.

3.4.5 Effect of Heat Flux Condition

Figure 3.9 contains many results showing the effect of heat flux profile on the thermal distortion results. The gap depths are all significantly higher with THF, where the heat flux drops from $3.2\dot{q}_{standard}$ to $\dot{q}_{standard}$ at t=0.06s. This shows that the high initial heat flux has a great effect in generating thermal distortion, even though it lasts for only a very short time. The SHF and HHF cases with constant heat flux generate much lower gap depths, even though the HHF heat fluxes and cooling rates greatly exceed those of THF for all times after 0.06s. This shows that regardless of steel grade and heat flux, the air gap forms and grows mainly during the very early stage of solidification. Thus, the final gap depth is very sensitive to the initial heat flux, while the later heat flux has little effect.

Figure 3.10 shows the evolution of the gap depth for the two most depression-sensitive steels, 0.003%C and 0.12%C, with different heat flux conditions. For all cases, the gap develops in three distinct stages. At the start of solidification, the gap depth remains at zero for a time period called “incubation time” in this paper. During this first stage, the steel shell is too weak to support even the small ferrostatic pressure from the liquid above it, so stays flat against the chill plate. The incubation time depends greatly on both steel grade and heat transfer coefficient, as shown in Table I, and greatly affects the final gap depth. After this incubation time, the shell has strengthened enough to overcome gravity and lift off of the plate. The gap grows very rapidly for a short time during this second stage: “growth”. Finally, there is a long third “steady-state” stage, when the gap remains relatively constant.

By increasing the heat flux from SHF to HHF, figure 3.9 shows that the gap depths (and corresponding curvatures) of steels with the lowest carbon contents, 0.003%C, 0.05%C and 0.10%C, increase significantly: by 100%, 140% and 100%, respectively. In contrast, the gap depths increase only slightly (12%, 5%, and 18%) for the other three grades, which have higher carbon content. Thus, there appears to be a general decrease in sensitivity to the higher heat flux with increasing C content, causing the jump in gap depth to decrease with increasing C content.

The higher sensitivity to heat flux in steels with carbon content less than 0.1%C stems from the different phase transformation sequence in these steels, compared with higher carbon steels. As can be seen in figures 3.2(a-c) steels with C≤ 0.1% solidify completely as δ-ferrite before transforming to austenite.

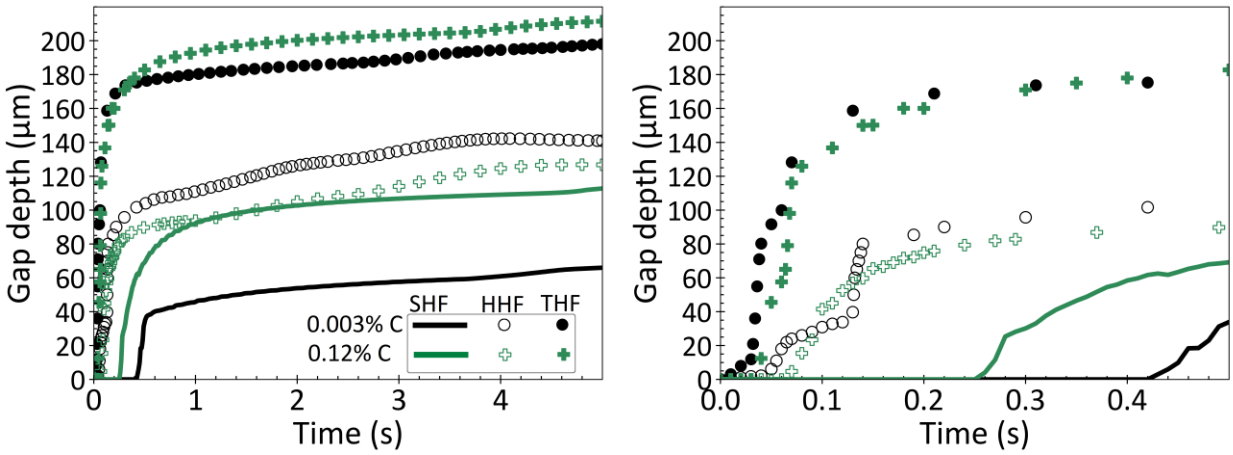

Figure 3.10. Gap depth evolution with time, comparing steels with 0.003%C and 0.12%C at different heat fluxes.

In these steels, by increasing heat flux from SHF to HHF, the δ-ferrite becomes thick enough to overcome ferrostatic pressure sooner, which in turn decreases the incubation time and

increases the gap depth considerably. On the other hand, in steels with higher carbon content, the liquid partly transforms to δ-ferrite and then the remaining liquid solidifies as δ-ferrite and austenite via the peritectic reaction.

The incubation time always occurs after the start of the δ→γ phase transformation, as shown in Table 1, except for 0.003%C steel, where this transformation is delayed. Increasing heat flux from SHF to HHF causes this transformation to occur sooner, as observed in figure 10 for 0.12%C steel. With THF, the incubation time occurs even sooner after the δ→γ transformation starts, especially for peritectic or partly-peritectic steels.

Further increasing the initial heat flux from HHF to THF causes the final gap depth to increase by about 100% for all grades. This is due to the large decrease in incubation time in all cases, caused by the high initial heat flux of THF.

3.4.6 Effect of Steel Composition

Depression sensitivity varies greatly with steel grade, as indicated by the final surface shape (curvature), shown in figure 3.9. figure 3.10 shows that, for the ultra-low carbon steel (0.003%C) with SHF, the incubation time is relatively long, 0.4s, at which time the gap depth increases to 38μm over 0.1s. This long incubation time is due to the weakness of the pure delta-ferrite initial shell, which is also very hot and thin due to the low heat flux, so it cannot overcome gravity during this long initial stage of solidification. The gap only starts to grow when austenite starts to form, after the surface has cooled to just below 1390 ^{o}C. With HHF, the solidified γ layer thickness increases faster, enabling the shell surface to cool and gain strength sooner, so the incubation time is only 0.05s. This leads to an initial gap depth of 90 μm, which is more than twice as deep as with SHF. Further increasing the initial heat flux from HHF to THF further decreases the incubation time to only 0.01 s, which doubles the initial gap depth again. This steel

has a very short solidification temperature range compared with all other steels. Thus, this steel can solidify more solid, for the same heat transfer and time, which enables the solid shell to become thicker and stronger, even though it is composed of soft delta-ferrite. Thus, this steel has the second highest gap depths and sensitivity to surface depressions of all steel grades investigated.

For 0.12%C steel with SHF, the incubation time is only 0.26s and the gap quickly grows to an initial depth of 81μm. This incubation time is shorter than that for ultra-low carbon and is due to the formation of the strong austenite phase very quickly after the start of solidification. For this steel, δ-ferrite is only stable for a 20˚C range, and quickly transforms to austenite via the peritectic reaction and subsequent peritectic transformation. Austenite is almost one order of magnitude stronger than δ-ferrite at the same temperature [352]. Thus, the solidified layer of 0.12%C steel quickly transforms to austenite, is strong enough to overcome ferrostatic pressure, and forms a gap very soon after the start of solidification. With HHF conditions, the incubation time is only 0.07s for steel with 0.12%C steel. After this incubation time, the gap depth suddenly increases to 91μm. Increasing heat flux from SHF to HHF has little effect on gap depth because the incubation time to strong austenite formation is short in both cases. Further increasing initial heat flux to THF conditions, the incubation time decreases to only 0.03s and the gap depth increases to the largest final depth of 190 μm. As mentioned earlier, surface depressions during steel solidification are attributed to the shrinkage associated with the solid-state δ→γ phase transformation. In 0.12%C steel this transformation coincides with a sudden drop in TLE (from 0.008 to 0.006) at 1490°C (see Figure 3.3). Because the new phase is the strong □-phase (almost 10 times stronger than δ-ferrite), the transformed austenite layer can overcome ferrostatic pressure even when it is very thin, (after only 0.03s), which aggravates the sudden TLE drop and

deepens the gap. As a result, this peritectic steel experiences the most severe gaps and sensitivity to surface depressions.

Figure 3.11 shows the evolution of the gap depth for all six investigated steels with THF, which has the highest initial heat flux. The peritectic steel, (0.12%C) transforms to austenite the fastest, so has the largest drop in TLE immediately below the solidus temperature, very short incubation time (0.03s), and consequently exhibits the deepest gap. For low-carbon (0.05%C), and high-carbon (0.23%C) steels, there is a greater temperature from the solidus to the start of transformation to austenite (see figure 3.3(d) and Table 1). This delay in the shrinkage (TLE drop), causes the shells of these steels to remain weak for a longer incubation time (0.06s). The longer incubation time causes smaller temperature gradients across the thin initial shell, leading to the smallest final gaps, and the least propensity towards surface depressions. The partly-peritectic steels (0.10%C and 0.16 %C) quickly transform to austenite, so have incubation times of only ~0.04 s, and thus these steels develop gaps almost as deep as the fully-peritectic steel of 0.12%C steel.

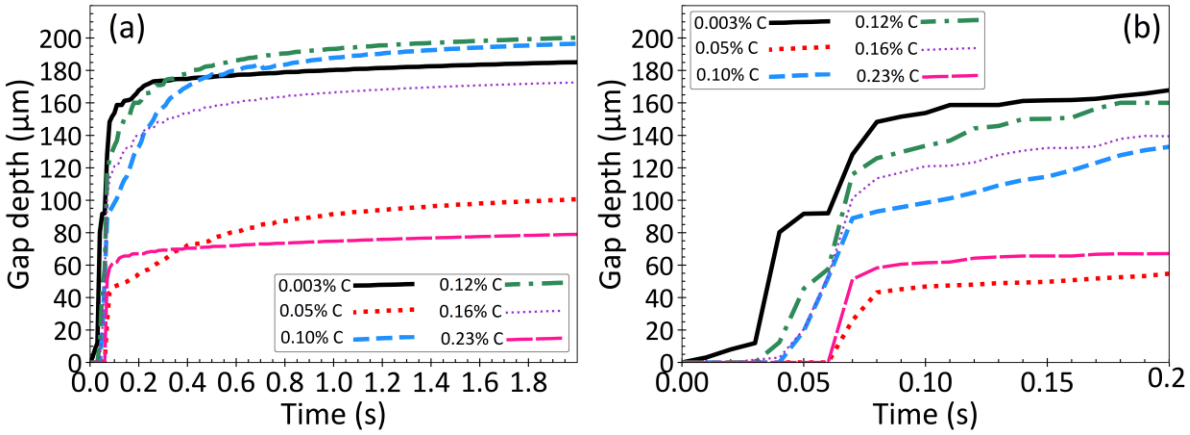

Figure 3.11. Gap depth evolution with time, with THF, for the six investigated steel grades.

These results show that the gap increases when the δ→γ transformation occurs sooner, (closer to the solidus temperature) and experiences the associated large drop in TLE when the shell is thinner. Ultra-low carbon steel has the shortest incubation time of 0.01 s and its gap depth is close to that of 0.12%C steel. It should be noted that with THF, for all grades, heat flux drops at 0.06s and the gap depth forms at either this time or earlier, (see incubation times in Table 1). With HHF conditions, heat flux is constant throughout solidification and cooling, but the gap still forms at roughly this time. With HHF, the droplet solidifies much sooner than with THF, but the gap depth is deeper with THF. These results confirm that the gap depth is controlled by heat flux during the very early stage of solidification, and usually starts soon after the start of the δ→γ phase transformation. Shorter incubation times produce deeper gaps. After that, changes in gap depth are very small, regardless of the heat flux.

3.5 Conclusions

The effects of steel carbon content and heat flux on the distortion of a steel droplet during solidification were investigated using a thermo-elasto-viscoplastic finite element model. Following the droplet test [323] as a benchmark experiment, the same chemical composition, geometry, and heat flux conditions were simulated to validate the model predictions of curvature of the bottom surface of the droplet with the measurements. The main findings are:

- The thermo-mechanical model captures the phenomena which govern gap formation during the initial stages of steel droplet solidification both qualitatively and quantitatively.
- Carbon content is the main factor that controls thermal distortion and bottom surface shape during steel solidification. The highest distortion, as indicated by the curvature of bottom surface of the droplet, is found in ultra-low carbon and peritectic steel grades.

- Heat flux also plays an important role in controlling thermal distortion during solidification. Increasing heat flux during the initial stages of solidification causes the gap depth (curvature of solidified droplet surface) to increase. This effect is most evident in ultralow carbon steels, and decreases with increasing carbon content, if the heat flux does not suddenly change.

- A sudden drop in heat flux typically accompanies gap formation, and is called the incubation time. This causes surface reheating, thermal expansion of the surface layer, and a very large increase in the gap depth, for all steel grades.

- Shorter incubation times lead to deeper gaps, owing to the higher temperature gradient across the thinner shell when the thermal distortion occurs.

- For every steel grade and heat flux condition investigated, the gap forms very early during solidification, within 0.06s for fast cooling and within 0.4s for slow cooling, and remains relatively constant after that. The heat flux rate at later times, after the first 1s, has little effect on the final thermally-distorted shape.

- The incubation time for gap formation is usually near or after the start of the $\delta \rightarrow \gamma$ phase transformation, which is controlled by the steel grade and initial heat flux. Thus, the gap forms sooner with faster initial cooling rates, and in peritectic steels.

- The gap depth is greatly affected by the $\delta \rightarrow \gamma$ phase transformation. In peritectic steel grades, this transformation occurs very soon after a thin solid shell has formed, which leads to deep gaps, implying deep surface depressions in cast products.

- Increasing the cooling rate and temperature gradient during initial solidification increases the severity of $\delta \rightarrow \gamma$ phase transformation, and results in a deeper gap.

- The findings of this fundamental model and gap formation mechanism have important implications for the formation of surface depressions and related defects in commercial steel continuous casting processes.

Acknowledgements

The authors wish to thank the contributing companies of the Continuous Casting Center at the Colorado School of Mines for funding that enabled this research.

CHAPTER 4
INTERACTIVE EFFECTS OF INTERFACIAL ENERGY ANISOTROPY AND SOLUTE TRANSPORT ON SOLIDIFICATION PATTERNS OF AL-CU ALLOYS

4.1 Abstract

Combined effects of the cooling rate, alloy composition, and crystal-melt (CM) interfacial anisotropy on solidification of Al-Cu alloys are studied by integrating molecular dynamics and phase-field simulations. Capillary fluctuation method is used to determine the CM interfacial energy properties by molecular dynamics simulations for alloys ranging from 3 to 11 at% Cu. While the average CM interfacial energy decreases with increasing Cu content, its anisotropy does not present a clear trend with composition change. Primary and secondary dendrite arm spacings as well as θ-phase fraction are calculated by phase-field simulations, and validated against experimental measurements and analytical solutions at cooling rates ranging from 1 to 1250 K/s. Results show that the θ-phase fraction decreases with increasing the cooling rate, and this reduction is more drastic in alloys with a higher Cu content. Also, the microstructure features are influenced by the growth dynamics, where seaweed structure formation results in a more homogenous distribution of θ-phase and a finer microstructure. The effects of temperature gradient, Cu concentration gradient, and interfacial energy properties on the dendritic growth morphology of Al-Cu alloys are summarized by a map of supercooling versus the CM interfacial anisotropy to predict pattern formation. The results show that, irrespective of Cu content and cooling rate, the seaweed structure formation is halted at CM interfacial anisotropies larger than 0.005. As the anisotropy decreases, different seaweed structures can form regarding the constitutional supercooling. At low anisotropies (Al-3 and Al-8.4 at% Cu) and low supercooling (Al-3 at% Cu) fractal or degenerate seaweed is dominant while at high supercooling (Al-8.4 at%

Cu) compact seaweed forms. This difference in supercooling stems from different solute atom transport rates.

Keywords: Al-Cu alloys; Solidification microstructure; Interfacial energy anisotropy; Molecular dynamics; Multi-phase field modeling.

4.2 Introduction

The crystal-melt (CM) interfacial energy is an intrinsic material property that plays a critical role in solidification pattern formation [56]. It influences the solidification microstructures in two ways; first, dendrites grow during solidification along the directions with the highest CM interfacial energy, and second, the instability of interface affecting the dendrite patterns, is controlled by the CM interfacial energy [57-59]. The CM interface energy has an anisotropic nature with respect to the crystallographic directions. Despite the unknown atomistic origin of interfacial energy anisotropy, for most alloys, the anisotropy is very small resulting in only a couple of percentage change in the interfacial energy in different crystallographic directions [56]. However, it governs the nucleation and growth kinetics [60-62], morphology [63-65], and crystallographic growth direction of the dendrites [66].

The instability of CM interface, which is influenced by the CM interfacial energy, controls microstructure evolution, dendrite arm spacing, and microsegregation patterns [58]. Coriell and Sekerka [67] added surface tension and surface kinetic anisotropy effects into the perturbation linear stability analysis and showed that the capillary term, that contributes in interface stability, is direction dependent [64, 68, 69]. Trivedi [353] compared experimental results with linear and weakly nonlinear analyses of the planar interface stability and showed that when a material is directionally solidified beyond the threshold of planar stability condition [71], the anisotropy of

interface properties not only affects the planar to cellular and cellular to dendritic transitions, but also causes tilting of cells and dendrite against the heat flow direction [72-74].

Besides dendritic microstructures, diverse types of morphologies can be formed during solidification of metallic alloys, including seaweed, dense-branched, fractal-like, and variations between these patterns [83]. These morphologies result from interactive effects of thermal diffusion, mass diffusion, and inherent interfacial anisotropy on interface stability. Amoorezaei et al. [83] showed that in a directionally solidified Mg alloy with low interfacial energy anisotropy, any change in processing condition considerably alters the solidification morphology. Their results indicated that at a low pulling velocity, seaweed structure is dominant, while by increasing pulling velocity compacted seaweed is the main morphology. In another study, Xing et al. [84] investigated the dynamics of growing dendrites and showed that the seaweed is the dominant morphology at weaker interfacial energy anisotropies, lower pulling velocities, and higher thermal gradients. It is believed that the instability at the tips, which stems from low surface energy anisotropy, is responsible for the formation of such a morphology [85, 86]. Chen et al. [87] showed that tip splitting takes place during the solidification of Al-4 wt% Cu with low interfacial energy anisotropy, which leads to seaweed structure. They argued that the seaweed regime is formed by morphological instability occurring when the cell/dendrite tip becomes too wide.

Despite its importance in predicting the microstructure, experimental measurements of the CM interfacial free energy and the anisotropy terms are very challenging and often not possible [88]. Because of the recent availability of reliable embedded interatomic potentials for metals, molecular dynamics (MD) has become a popular method for calculating the CM interface free energy. Among the two well-known methods, namely Cleavage [89] and the capillary fluctuation

method (CFM) [90], the latter results in a more accurate anisotropy parameter calculations, which is used in this study. CFM has been extensively used for interface energy calculations of metals [91-96], compounds [97], and binary alloys [98, 99].

The interface energy for an alloy depends on the working temperature and alloy composition. There are different MD simulations that discuss how the change in chemical composition alters the interface free energy and its anisotropy. Becker et al. [100] used CFM to show that the CM interface energy in Ni-5at%Cu alloy is 7.4% less than pure Ni. Furthermore, the addition of 5 at% Cu decreases $\square_1$ (Fourfold anisotropy parameter) from 0.09 to 0.072 and increases $\square_2$ (Six-fold anisotropy parameter) from -0.011 to -0.007 [101]. Potter and Hoyt [102] applied the CFM to the Cu-rich Cu–Ag–Au system; they indicated that species with a high enthalpy of mixing tend to destabilize the dendrites growing in the $\langle 100 \rangle$ direction and promote a transition to the growth of hyper-branched and $\langle 110 \rangle$ –oriented dendrites.

There are very limited experimental studies that support the computationally-predicted change in interface free energy and the corresponding anisotropy due to change in alloy composition. Using experimental observation [103] and phase-field modeling [104], it was shown that in Al-Zn alloys (Zn<25 wt%) with high values of ϵ_1 (four-fold anisotropy parameter) and low values of $|\epsilon_2|$ (six-fold anisotropy parameter), $\langle 100 \rangle$-oriented dendrites are dominant. When Zn concentration is more than 55 wt%, the value of ϵ_1 is low and the absolute value of ϵ_2 is high. Under this condition, $\langle 110 \rangle$ is found to be the favorable growth direction. In the intermediate regions, surface energy anisotropy becomes very small and leads to the formation of seaweed structures or hyper-branched dendrites [105]. Recently, Wang et al. [56] showed that in Al-Sm alloy system, increasing Sm content drastically reduces anisotropy strength while increasing the average interface energy (γ_0). The aforementioned studies indicate that chemical

composition is the main factor that controls CM interfacial energy and its anisotropy. Also, it was shown that since the equilibrium composition at CM interface changes by temperature, its energy and anisotropy are a function of temperature [107-109].

While the impact of CM interfacial anisotropy on the orientation selection and the interface stability is well established, there is a gap in the literature regarding its influence on the final phase fractions, arm spacing, and microsegregation. Furthermore, the combined effects of the CM interfacial anisotropy and alloying element content on growth dynamic are not well-understood. In this work, we performed an atomistic-informed phase-field study to investigate the microstructure evolution during solidification of Al-Cu binary alloys under different solidification conditions. First, MD simulations are performed to reveal the relationship between CM interfacial energy properties and Cu content. Subsequently, a multi-phase field model is utilized to explore how Cu concentration gradient ahead of growing dendrite (G_c) and CM interfacial anisotropy collaborate to generate different solidification patterns and consequently different solidification features, such as dendrite arm spacings, and θ-phase fraction and distribution. The simulation results are validated by comparison to experimental measurements and analytical solutions in a wide range of cooling rates from 1 to 1250 K/s.

4.3 Computational Models and Simulation Procedure

We use multi-phase field modeling to study microstructure evolution and pattern formation during solidification of different compositions of Al-Cu binary system. MD simulations were completed to determine the CM interface energy and its anisotropy for different compositions.

4.3.1 Molecular Dynamics Simulations

In CFM [90], the interface stiffness is obtained based on the interface's fluctuation amplitude, cross-section, and target temperature. Figure 4.1(a) demonstrates a snapshot of the

simulation system. The simulation system contains the coexistence of solid-and liquid, where the central part is in the liquid phase, and the CM interface normal is considered parallel to the z-direction. The interface is quasi-two dimensional (2D), where the interface width along y-direction, b, is much shorter than its length along x-direction, W. The simulation size along z-direction is considered very large to avoid any interactions between the interfaces. The position of atoms located at the CM interface, as presented by orange color in figure 4.1(b), is used to determine the position of interface, $p(x)$, for each time frame. The deviation of the interface position from its mean value, $\langle p \rangle$, can be written as a summation of Fourier Modes, $p(x) - \langle p \rangle = \sum_k A(k)\, e^{ikx}$. Based on the equipartition of energy and considering the Fourier modes as the degrees of freedom, Equation (1) relates the interface stiffness to the amplitudes and modes of Fourier transform.

$$\gamma + d^2\,\gamma/d\,\theta^2 = \frac{\mathrm{k_B}T}{\mathrm{bW}\langle|A(k)|^2\rangle k^2} \qquad (4.1)$$

where $\mathrm{k_B}$, is Boltzmann constant, T is the temperature, $\langle|A(k)|^2\rangle$ is the mean squared amplitude of the Fourier modes, and k is the mode wave number. γ is the CM interface free energy and $\gamma + d^2\,\gamma/d\,\theta^2$ is the interface stiffness, where θ is the angle between instantaneous local interface normal and the average orientation of interface. Interface free energy is an anisotropic property, and one can calculate the anisotropy term by considering different crystallographic orientations for the CM interface in the CFM. The spherical harmonic expansion of interface energy, which depends on interface normal orientation ($\hat{n}$), is represented:

$$\gamma(\hat{n}) = \gamma_0[1 + \delta_1(4\sum_{i=1}^{3} n_i^4 - 3) + \delta_2(\sum_{i=1}^{3} n_i^6 + 30n_1^2n_2^2n_3^2)] \qquad (4.2)$$

where $n_i(i = 1,2,3)$ are the components of normal to the interface vector, $\hat{n}$ in x and y and z-directions, γ_0 is the mean CM interface free energy, and δ_1 and δ_2 are the anisotropy

parameters, [354]. γ_0, δ_1, and δ_2 can be estimated by fitting the stiffness calculated from MD simulations to the analytical stiffness expression calculated from Equation (2). Details on obtaining the analytical stiffness expressions for each orientation can be found in our previous works [93-96, 98, 99].

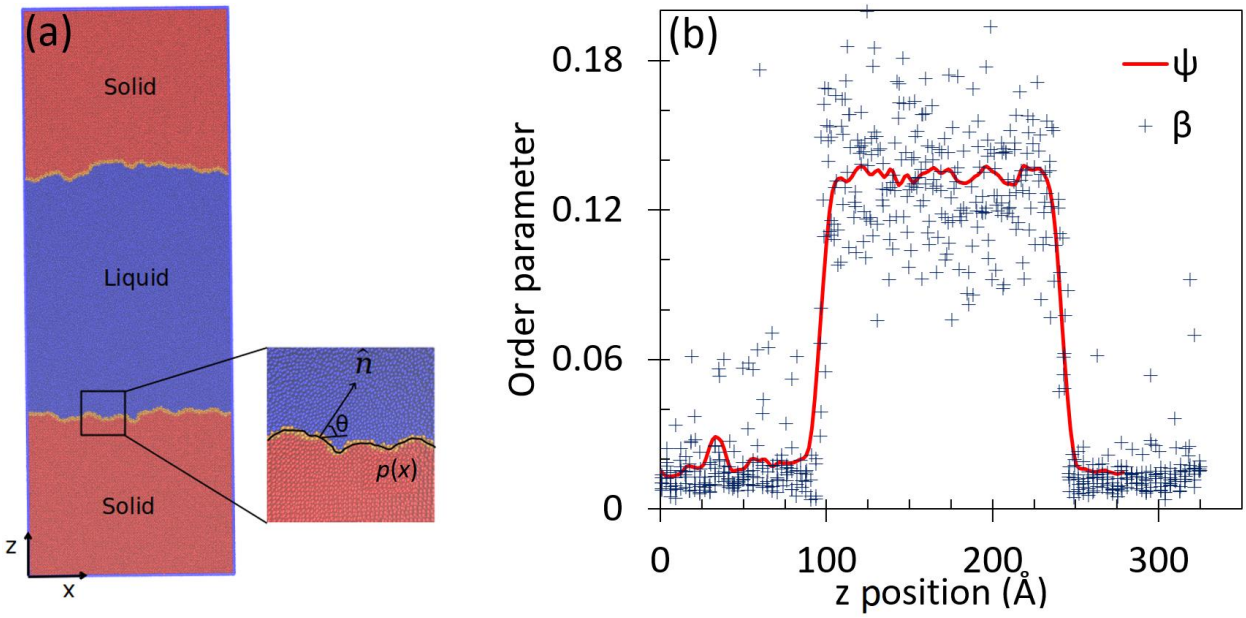

Figure 4.1. (a) Snapshot of MD simulation system demonstrating the two-phase coexistence slab. The red and blue colors represent the solid and liquid phases, respectively. The atoms located at the interface are colored as orange. (b) Order parameters, ψ and β, as a function of z. They are used to identify the solid and liquid phases.

All the MD simulations are performed using LAMMPS (Large-scale Atomic/Molecular Massively Parallel Simulator) [355], and the Al-Cu interatomic potential used in this study is developed by Avik and Asle Zaeem [356], which is based on the second nearest neighbor modified embedded atomic method (2NN-MEAM). This potential is specifically developed to reproduce the high temperature thermophysical and transport properties of the binary Al-Cu system. It should be mentioned that we have recently performed in depth nanoscale solidification

study of metals and performed uncertainty calculations to show the accuracy of MD simulations with 2NN-MEAM potentials [357, 358].

Since fluctuations of CM interface must be performed on the fully equilibrated coexistence of CM, the equilibrium CM phase boundary compositions for different temperatures are required. Thus, the first step is performing MD simulations to calculate the phase diagram. The details of phase-diagram calculations are explained in our previous work [98]. We calculate the phase diagram for temperatures ranging between 925 K (melting point of pure Al) and 860 K.

For [100]-oriented CM interface, first the interface energy is calculated by MD simulations using 50×4×80 face-centered cubic (fcc) unit cells (6400 atoms) of pure Al with [001] orientation along the z-direction. The simulation systems with [110] and [111] interface orientations have similar dimensions and number of atoms. First, the simulation system is equilibrated under NPT ensemble at the target temperature for 100 ps. Then, the central half of the system is melted by performing an NVT ensemble, at T=2000 K, for 40 ps, while keeping the rest of system unchanged. The temperature of the system is reduced to the target temperature, and to determine the interface energy of Al-Cu systems, some of Al atoms in the solid and liquid phases are replaced by Cu alloys such that the final solute concentration in each phase is consistent with the phase diagram. The simulation box sizes in x and y-directions are adjusted to obtain the correct lattice parameter of the solid phase at the target temperature and composition. This lattice parameter is obtained from a separate MD simulation on a system having solute concentration corresponding to the target temperature.

After proper size scaling of the simulation box, the system is equilibrated under a hybrid $NP_{ZZ}T$ (isothermal-isobaric) MD/MC ensemble. During this process, the box size is only allowed

to change in the z-direction, and the equilibration of concentration is performed using MC to randomly attempt swapping 3000 Al and Cu atoms every 5000 steps. The overall equilibration time considered ranges between 1 ns and 2. During this process, the potential energy of the system should approximately stay constant during the last 200 ps of the equilibration time. At the final step, an NPH ensemble (isoenthalpic–isobaric) is performed for 240 ps. During this step, the system configuration is saved every 1 ps for further analysis of the interface fluctuations.

Further analysis of the trajectory files is required to determine the local interface position, $p(x)$. This is performed by introducing an order parameter, β, for each atom, which identifies the solid and liquid phases by comparing the positions of its 12 first neighbors with its perfect crystal, $\vec{r}_{FCC}$ [92].

$$\beta = \frac{1}{12}\sum_i |\vec{r_i} - \vec{r}_{FCC}|^2 \quad (4.3)$$

This order parameter fluctuates a lot, as presented in figure 4.1(b), which makes the determination of interface position challenging. Thus, a new order parameter, ψ, was introduced by Asadi et al. which uses a smoothing function, w_d, to reduce fluctuations of β [94]:

$$\psi(x,z) = \frac{\sum_i w_d r_i \beta_i}{\sum_i w_d r_i} \quad (4.4)$$

Where $w_d = [1-(r_i/d)^2]^2$, $r_i = \sqrt{(x_i - x)^2 + (z_i - z)^2}$. The smoothing is performed over cylinders perpendicular to the y-direction with the radius of d. Figure 4.1(b) shows the change of ψ and β along the z-direction. The initial order parameter, β, fluctuates a lot, therefore the smoothened order parameter, ψ, is used, which approximately takes constant values in solid and liquid, and the location of the interface is defined to be where ψ is halfway between those

values. By performing Fourier transform on the interface position data and averaging the Fourier amplitude over all the time frames, we use Equation (1) to calculate the interface stiffness.

4.3.2 Multi-Phase Field Modeling

In this paper, a multicomponent multiphase-field model presented by Eiken et al. [359] is used, which is implemented in the software MICRESS® (version 6.4) [360]. Three non-conserved order parameters were assigned for liquid, α-phase (fcc-Al) and Al_2Cu, and one conserved order parameter, *c*, was assigned for Cu concentration. The phase-field equation governing the interface kinetics is expressed as [361],

$$\dot{\varphi}_\alpha = \sum_{\beta\neq\alpha}^{\nu} M_{\alpha\beta}^{\varphi}\left[b\Delta G_{\alpha\beta} - \sigma_{\alpha\beta}\left(K_{\alpha\beta} + A_{\alpha\beta}\right) + \sum_{\gamma\neq\beta\neq\alpha}^{\vartheta} J_{\alpha\beta\gamma}\right] \quad (4.5)$$

$\dot{\varphi}_\alpha$ is the time derivative of order parameter, where, α, β, and γ represent three different phases, and ν is the number of grains in the system. The subscripts αβ and αβγ represent the interface between grains with α and β phases, and the triple point junction between grains with α, β, and γ phases, respectively. Parameter $M_{\alpha\beta}^{\varphi}$ represents the phase-field mobility of the interface αβ and is related to the kinetic coefficient in the Gibbs-Thomson equation, $\mu_{\alpha\beta}^{G}$ (also known as the sharp interface mobility), through Eq. 4.6 [361].

$$M_{\alpha\beta}^{\varphi} = \frac{\mu_{\alpha\beta}^{G}}{1+\frac{\mu_{\alpha\beta}^{G}\eta\Delta s_{\alpha\beta}}{8}\left\{\sum_i m_i^l \sum_j\left[\left(D_\alpha^{ij}\right)^{-1}(1-k_j)c_{j\alpha}\right]\right\}} \quad (4.6)$$

η is the interface thickness in the phase-field simulations, $\Delta s_{\alpha\beta}$ is the entropy change during α to β phase transformation, m_i^l is the slope of the liquidus line, D_α^{ij} is the diffusion matrix in α phase, and k_j is the partition coefficient of solute atom j. For alloys where η is finite, the equation will result in a phase-field mobility that is smaller than the sharp interface mobility.

The first ($b\Delta G_{\alpha\beta}$), second ($\sigma_{\alpha\beta}\left(K_{\alpha\beta}+A_{\alpha\beta}\right)$), and third ($\sum_{\gamma\neq\beta\neq\alpha}^{\vartheta} J_{\alpha\beta\gamma}$) terms on the right-hand-side of Equation (5) represent the bulk, interface, and high order junction energy terms, respectively. In the first term, b is the pre-factor and $\Delta G_{\alpha\beta}$ is the molar Gibbs free energy density calculated by Equations (7) and (8), respectively.

$$b=\frac{\pi}{\eta}\left(\varphi_{\alpha}+\varphi_{\beta}\right)\sqrt{\varphi_{\alpha}\varphi_{\beta}} \quad (4.7)$$

$$\Delta G_{\alpha\beta}=\frac{1}{v^{m}}\left[\mu_{\beta}^{i}\left(\vec{c}_{\beta}\right)-\mu_{\alpha}^{i}\left(\vec{c}_{\alpha}\right)\right] \quad (4.8)$$

v^{m} is the molar volume of the phases, $\vec{c}_{\alpha}$ and $\vec{c}_{\beta}$ are concentration of solvent in α and β phases, $\mu_{\beta}^{i}\left(\vec{c}_{\beta}\right)$ and $\mu_{\alpha}^{i}\left(\vec{c}_{\alpha}\right)$ are the chemical potential of component i in α and β phases, which are defined as the increment in the Gibbs free energy of the phases, G_{α} or G_{β} , when a very small moles of species *i*, n^{i}, is added to these phases, while all other variables of the phase are kept constant.

In the second term of Equation (5), $\sigma_{\alpha\beta}$, $K_{\alpha\beta}$, and $A_{\alpha\beta}$ represent the interfacial energy, pairwise curvature, and anisotropy of the interface αβ, respectively. While $\sigma_{\alpha\beta}$ is a constant value, $K_{\alpha\beta}$ is calculated by:

$$K_{\alpha\beta}=\frac{\pi^{2}}{2\eta^{2}}\left(\varphi_{\beta}-\varphi_{\alpha}\right)+\frac{1}{2}\left(\nabla^{2}\varphi_{\beta}-\nabla^{2}\varphi_{\alpha}\right) \quad (4.9)$$

And the anisotropy of the interface for cubic symmetry is given by

$$A_{\alpha\beta}=1+\varepsilon_{4}\cos(4\varphi). \quad (4.10)$$

ε_{4} is the strength of anisotropy, $\varepsilon_{4}\in(0\ 1)$, and φ is the azimuthal angle measured from a reference direction.

The high order triple junction term in the third term of Equation (5), $J_{\alpha\beta\gamma}$, is calculated from equation (11) as:

$$J_{\alpha\beta\gamma} = \frac{1}{2}\left(\sigma_{\beta\gamma} - \sigma_{\alpha\gamma}\right)\left(\frac{\pi^2}{\eta^2}\varphi_\gamma + \nabla^2\varphi_\gamma\right) \quad (4.11)$$

Solute diffusion is described by [361]:

$$\dot{c}^i = \nabla \sum_{\alpha=1}^{v} \sum_{j=1}^{n-1} \varphi_\alpha D_\alpha^{ij} \nabla c_\alpha^j \quad (4.12)$$

For a system with n species, $c^{i=1\ldots..n-1}$ are the concentrations of the solute species. Diffusion coefficients D_α^{ij} are function of temperature individually for each phase in an Arrhenius approach.

Simulations are executed on 2D domains of 200 μm × 200 μm and 600 μm × 1000 μm with grid spacing of $\Delta x = \Delta y$ = 0.2 μm. Furthermore, a 3D simulation was performed with 150 μm × 150 μm× 150 μm domain size and the same grid spacing as in 2D to show there is not a noticeable difference between 2D and 3D results. The simulations started from 100% liquid phase at liquidus temperatures. The liquidus temperatures for Al-Cu alloys with 3, 6, 8.4 and 10.6 at% Cu were obtained from Thermo-Calc simulations, and they are 915.35K, 897.8K, 883.13K, and 869.3 K, respectively. Heat is extracted from the bottom boundary to an external medium with a fixed temperature of 298K and different heat transfer coefficients (h) of 0.5, 2, and 4 W/cm^{2}K. We used an embedded model for heterogeneous nucleation that creates randomly oriented initial seeds of the solid phase α at the bottom boundary (with 1μm thickness) whenever the local undercooling exceeded the required critical value (1 K for all simulations), while further nucleation is prohibited. Al_2Cu nucleation takes place at the interfaces of α/liquid with the same undercooling criterion [362]. The interaction between Al_2Cu with liquid and alpha phases was considered to be isotropic. The interfacial energies of Al2Cu/liquid and Al2Cu/alpha were set to 9.2×10^{-6} [363] and 3.7×10^{-5} [364], respectively.

The set of multi-phase-field equations are solved using finite-difference method to simulate the growth of the phases [365]. Solute redistribution is evaluated at all phase interfaces under the constraint of equal diffusion potentials [359]. Diffusion of Cu is solved in the liquid and α-phase under consideration of a numerical anti-trapping current within the diffuse interface regions [366]. Temperature is evaluated in the direction of heat flow (1-D temperature field). The conductivities of liquid and α-phase are set to 1.5 and 1.9 W/cm.K, respectively [367-369]. All thermodynamic materials properties such as driving forces, local undercooling, interface concentrations, heat capacity, enthalpy, and latent heat as well as the diffusion kinetics required for the phase-field simulation are calculated using Thermo-Calc and are passed to MICRESS through the TQ-interface (Thermodynamic Calculation Interface). The thermodynamic and mobility databases used for the current study are TCAL7 (Thermo-Calc database for Al-based alloy, version 7) and MOBAL5 (Al-based alloy mobility database, version 5).

Boundary conditions for phase-field order parameters and concentration are periodic at the left and right boundaries of the 2D domain, and the Neumann boundary condition (no-flux) is applied at the top and bottom boundaries. Boundary conditions for temperature are as follows: fixed at the bottom and the Neumann boundary condition (no-flux) at the top, left, and right boundaries.

4.4 Results and Discussion

Al-Cu alloys with 3, 6, 8.4, and 10.6 at% Cu are studied in this work. Solidification takes place by removing the heat from the bottom surface of the 2D domains under different heat transfer coefficients of 0.5, 2, and 4 W/cm^{2}K. First, the effect of Cu content on CM interfacial energy and its anisotropy is investigated through MD simulations. Then, multi-phase modeling is

used to study microstructure evolution and solidification pattern formation in the aforementioned Al-Cu alloys.

4.4.1 Crystal-Melt Interfacial Free Energy and Related Anisotropy Calculations

The first step for calculating CM interfacial free energy is obtaining the equilibrium crystal-melt phase boundary compositions for different temperatures. Interface energy calculations are performed on systems with Cu compositions ranging between 3 and 11 at%; the corresponding portion of the Al-Cu phase diagram, calculated by MD simulations and Thermo-Calc, is presented in figure 4.2.

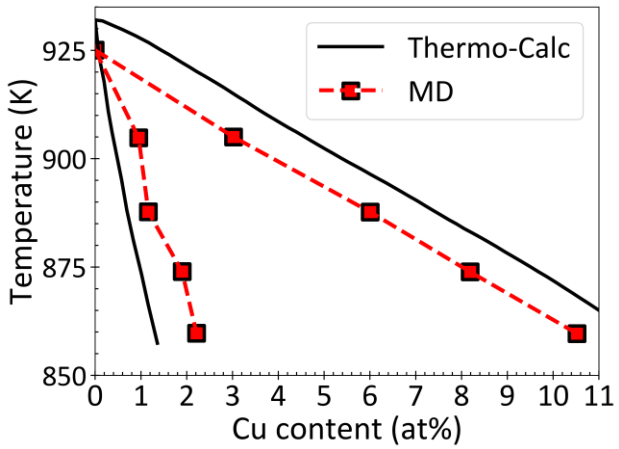

Figure 4.2. Cu-rich composition-temperature phase diagram for Al-Cu alloy calculated by MD simulations and Thermo-Calc. The symbols L and S denote the liquid and solid phases, respectively.

MD simulations are performed considering different orientations for the interface normal and interface width, given by [] and < >, respectively. Table 2 summarizes the details of the investigated orientations and the corresponding interface energy and stiffness expressions using Equation (2). For the interface planes with three-fold or higher symmetry, the stiffness value

does not depend on the orientations in which the interface is curved [370]. [110] oriented interface is an example that includes a two-fold symmetry. Thus, as demonstrated in Figure 4.2, considering two different orientations ($\langle 001 \rangle$ and $\langle 001 \rangle$) in the x-direction alters both the stiffness expression and its value. For the [110] CM interface, we performed two separate simulations, and one can distinguish the difference in their stiffness expressions presented in Table 1.

For each orientation, the interface stiffness is estimated by the slope of line fitting $k_B T/(bW\langle |A(k)|^2 \rangle)$ versus k^2. The stiffness values calculated by MD simulations are fitted to the stiffness expressions using Equation (2) to calculate the average CM interface free energy and the anisotropy parameters. Figure 4.3 shows the variation of $k_B T/bW< |A(k)|^2 >$ versus k^2 for the CM interface energy of the Al-Cu binary system at T= 888 K with the solidus and liquidus Cu compositions equal to 1.16 and 6 at%.

Table 4.1. The expressions of interface free energy, γ, and stiffness, $\gamma + d^2\gamma/d\theta^2$, for various interface orientations, as given by Equation (2).

orientation	γ	$\gamma + d^2\gamma/d\theta^2$
$\langle 100 \rangle$ [001]	$\gamma_0 [1+\delta_1 +\delta_2]$	$\gamma_0 [1 - 15\ \delta_1 - 5\ \delta_2]$
$\langle 001 \rangle$ [110]	$\gamma_0 [1 - \delta_1 +0.25\ \delta_2]$	$\gamma_0 [1 -9\ \delta_1 + 13.75\ \delta_2]$
$\langle 1\bar{1}0 \rangle$ [110]	$\gamma_0 [1 - \delta_1 +0.25\ \delta_2]$	$\gamma_0 [1 + 15\ \delta_1 + 6.25\ \delta_2]$
$\langle 1\bar{1}0 \rangle$ [111]	$\gamma_0 [1 - 1.67\ \delta_1 +1.22\ \delta_2]$	$\gamma_0 [1+ 9\ \delta_1 - 9.45\delta_2]$

It should be mentioned that Equation (1) fails for small wavelengths, and a logarithmic behavior is expected for large values of k [101]. Thus, in the fitting process and stiffness calculations, only the portion of the MD results related to the linear section is used in the analysis. The fitting process results in γ_0=96.11±7.4 mJ/m^2, δ_1=0.014, and δ_2=-0.0042.

Considering $\delta_1>0$ and a small value for δ_2, Equation (2) produces either [100] and [110] dendrites. Larger δ_1 results in the growth of [100]-oriented dendrites, but when $\delta_2<0$, [110] dendrites can also grow [104].

A similar process is repeated for all the other binary systems. The interface energy and anisotropy parameters are summarized in table 2. In Table 4.2 Each binary system is presented by a temperature and the corresponding equilibrium liquidus and solidus concentrations.

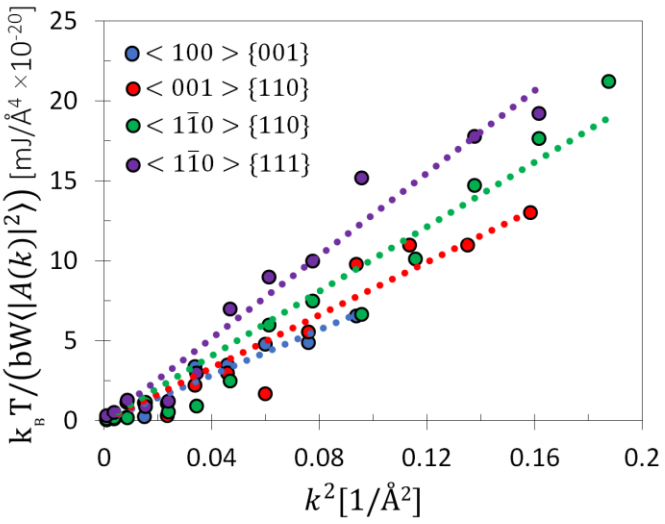

Figure 4.3. The variation of $k_B T/(bW\langle|A(k)|^2\rangle)$ versus k^2 for different orientations as obtained by MD simulations of Al-Cu binary system at T=888 K with solidus and liquidus Cu compositions equal to 1.16 and 6 at.%. The dotted lines are linear fits to symbols with the same color.

The results do not reveal a trend line for the anisotropy changes, but the mean CM interface free energy decreases by a decrease of temperature (an increase of solute concentration). In 2D, the interfacial energy is:

$$\gamma = \gamma_0\left(1 + \varepsilon_4(\cos 4\varphi)\right) \tag{4.13}$$

where ε_4 is the anisotropy parameter in 2D, and φ is the azimuthal angle. Using trigonometric relations, ε_4 is calculated as a function of 3D anisotropy parameters (δ1 and δ2) and presented in Table 2. The details of calculating ε_4 is presented in Appendix 1.

Table 4.2. The average interface free energy, γ_0 (mJ/m2), anisotropy parameters, δ_1 and δ_2, defined in Eq. 4.2, and ε_4, defined in Eq. 4.13, for four Al-Cu binary systems. Each binary system is identified by the solidus, C_S, and liquidus, C_L, compositions at temperature T, which are obtained from the phase diagram, Figure 4.2.

				γ_0	δ_1	δ_2	ε_4
Case I:	T=905 K	C_s=0.96 at%	C_L=3.05 at%	110 ± 4.9	0.0045	-0.0026	0.0035
Case II:	T=888 K	C_s=1.16 at%	C_L=6.0 at%	96.11 ± 7.4	0.014	-0.0042	0.0124
Case III:	T=874 K	C_s=1.93 at%	C_L=8.2 at%	92.24 ± 7.3	0.008	-0.0044	0.0050
Case IV:	T=860 K	C_s=2.2 at%	C_L=10.6 at%	89.8 ± 6.9	0.01	-0.0079	0.0071

4.4.2 Grid Convergence Study

Grid convergence study was conducted for directional solidification of Al-3 at% Cu with different heat transfer coefficients (h), to demonstrate that the solution is independent of the discretization at different growth rates. Grid spacing is not the only numerical parameter that influences simulation results, and proper interface mobility (IM) values need to be determine to guarantee diffusion-controlled growth without kinetically slowing down the interface [371]. In order to determine appropriate grid size and IM, simulations should be run with different IM values for a constant grid size, and phase fraction versus time should be plotted for quantitative grid resolution study [371]. By increasing IM value two behaviors can be observed: (1) If grid size is large, by increasing IM, the growth rate increases until numerical instability takes place, or (2) If grid spacing is fine enough, by increasing IM, the growth rate will reach a constant

value and remains constant even for higher IM values. In this study, heat transfer coefficients were set to h= 0.5, h=2, and h=4 W/cm^{2}K, and for each heat transfer coefficient a grid resolution study was conducted where domain size was 100 μm by 120 μm. Figure 4.4(a)-(c) show θ-phase fraction as a function of time for grid size of 200, 100, and 50 nm at different IM values for h=0.5 W/cm^{2}K. In this figure for all grid sizes, the growth rate of θ-phase increases by increasing IM. While for grid spacing of 200 nm, numerical instability takes place at IM of 0.8 cm^4/Js and no instability was observed in the case of grid sizes of 100 and 50 nm. The solidification microstructure for different grid size at IM of 0.8 cm^4/Js are shown in figure 4.4(d)-(f).

These results prove that by choosing a grid size of 100 nm and an IM value of 0.4 cm^4/Js when heat transfer coefficient is h=0.5 W/cm^{2}K, the solution is independent of grid size. Furthermore, the minimal interface curvature radius (minimum tip radius) at h=0.5 W/cm^{2}K is 600 nm which is much higher than the selected grid size.

The same procedure was followed to perform grid convergence studies for heat transfer coefficients of 2 and 4 W/cm^{2}K. The results demonstrated that the results are independent of grid size for both heat transfer coefficients when the grid size and IM value are 50 nm and 0.4 cm^4/Js, respectively. The minimal radius of curvature of interface at h=2 and h=4 W/cm^{2}K is 350 and 300 nm, respectively, which is much higher than the selected grid size.

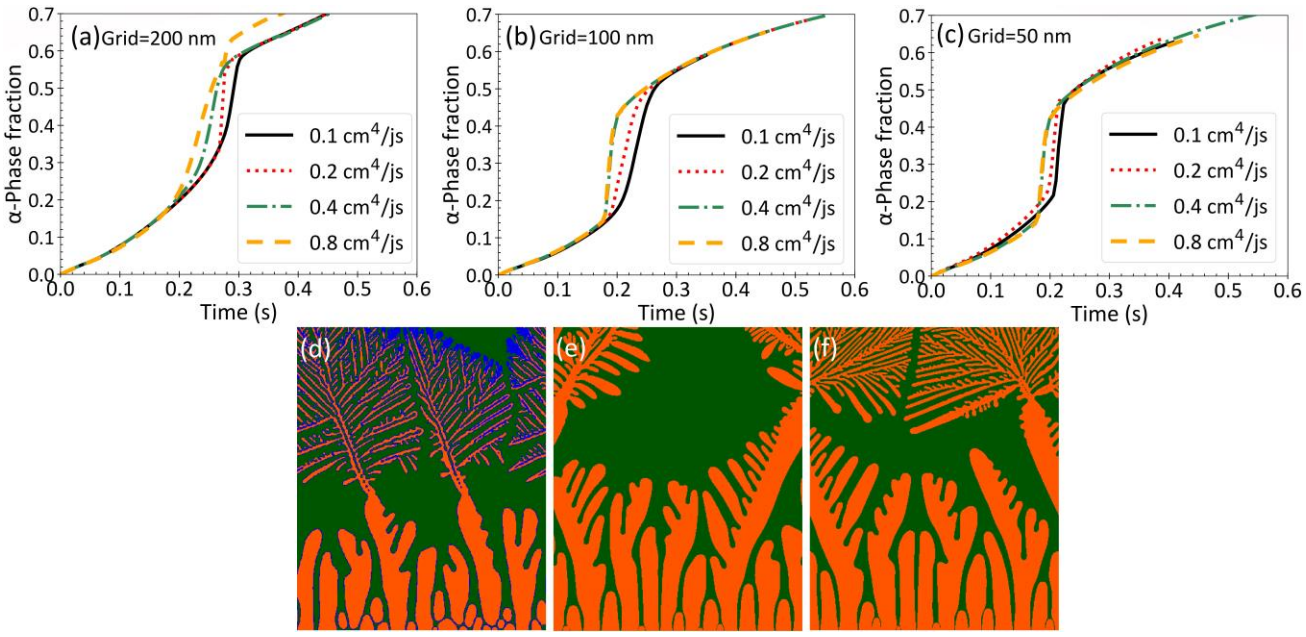

Figure 4.4 Grid convergence data (a-c) θ-Phase fraction as a function of time for different grid size and IM values at heat transfer coefficient of h=0.5 W/cm^{2}K, (d-f) Related microstructure at IM of 0.8 cm^4/Js and different grid size, (d) 200 nm, (e) 100 nm, and (f) 50 nm. Numerical instability takes place when grid size is 200 nm while no instability was observed when grid size is set to 100 and 50 nm, even for very high IM values.

4.4.3 Comparison of Predicted Primary Dendrite Arm Spacing to Experiments

Simulation results of the primary dendrite arm spacing (λ_1) of Al-3 at% Cu (Al-6.9 wt% Cu) are validated by experimental measurements [372-378] and analytical solutions[379, 380]. We performed 2D phase-field simulations of solidification for cooling rates ranging between 3.2 and 165℃/s. Also, a 3D phase-field simulation is completed to show there is only a negligible difference between 2D and 3D simulations in this study. Figure 4.5(a)-(f) presents the dendritic microstructure at different cooling rates, and the overall comparison of the phase-field results with the experimental measurements and analytical solutions is summarized in figure 4.5(g). The model predictions are in a good agreement with the experimental measurements. Also, it is evident that at low cooling rates, long secondary arms are developed in directions that are not

necessarily perpendicular to primary arms; while by increasing the cooling rate, secondary arms get shorter and are perpendicular to primary dendrites. This change of secondary arm features with cooling rate has been observed in both experimental [381] and simulation [382] studies. It should be noted that in the case of 3D simulation, the primary dendrite arm spacing was obtained using the Voronoi Warnken–Reed approach with α parameter equals to 1.8 [383] .

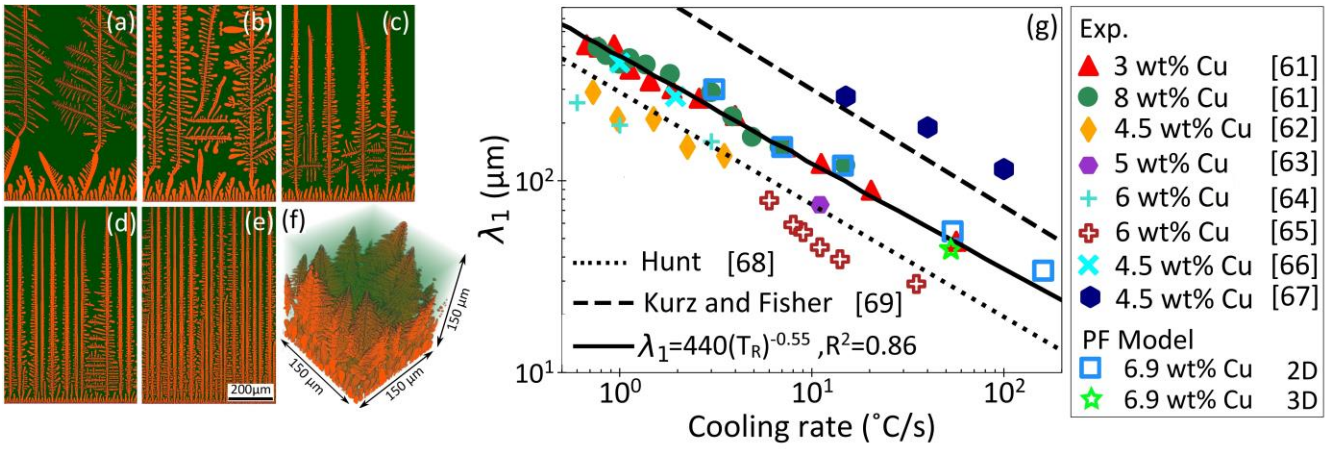

Figure 4.5. Predicted microstructure using 2D phase-field simulations at different cooling rates (a) 3.2 °C/s, (b) 7 °C/s, (c) 17 °C/s, (d) 52 °C/s, and (e) 165 °C/s; (f) 3D phase-field simulation at cooling rate of 52 °C/s; orange and green colors show solid and liquid phases, respectively; and (g) Comparison of the experimentally measured primary dendrite arm spacing with phase-field simulation results.

It can be seen in figure 4.5(f) that 9 dendrites are formed in the domain. The traditional approach for measuring λ_1, is given by $\lambda_1=c\sqrt{\frac{A}{n}}$, where n is the number of dendrites, *A* is the area normal to growth direction, and c is coefficient equals to 1.075 for hexagonal array of points [384] which is the case for 3D simulation. Considering this approach, λ_1=53.75 which is very close to the obtained value from the 2D simulation with the same cooling rate (52 °C/s).

4.4.4 Microstructures Characteristics

We investigate the microstructural features and how they are related to solidification conditions. The microstructures of solidified Al-Cu alloys with different heat transfer coefficients (different h) predicted by phase-field simulations are presented in figure 4.6. In this figure, green, white and red colors represent α-phase, θ-phase, and liquid, respectively.

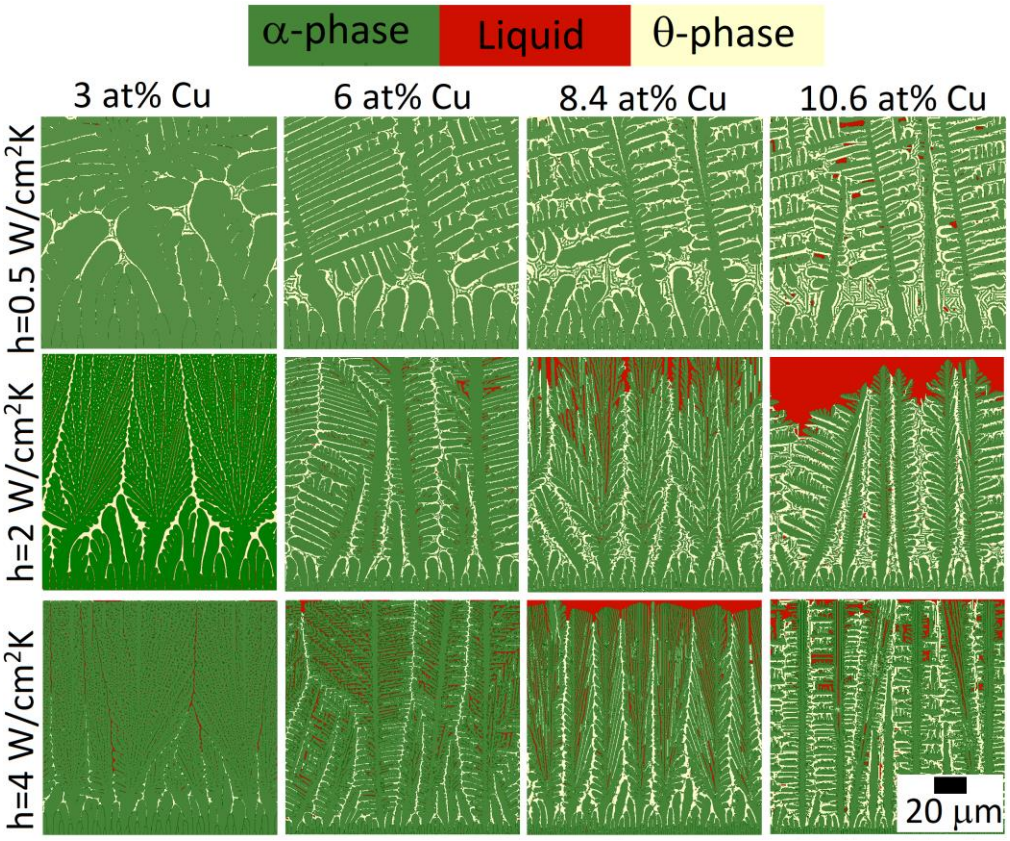

Figure 4.6. Microstructures of Al-Cu alloys solidified with different heat transfer coefficients. The temperature of top surface is 397 K for all cases.

The solidified microstructures are different in many aspects, including primary and secondary arm spacing, phase fractions, and phase distribution. These diverse microstructures stem from different growth dynamics of dendrites during solidification, which is influenced by

solute atom redistribution, the anisotropy of CM interface energy, and cooling conditions. We will focus on the solidification pattern formation in the following sub-section (3.5), and here we focus on analyzing the microstructural features. For all investigated alloys, when the heat transfer coefficient is 0.5 W/cm^{2}K, dendrites are tilted against the heat transfer direction (HTD). By increasing h to 2 and 4 W/cm^{2}K they get aligned with HTD. In addition to the change in dendrite growth direction, dendritic morphologies in different alloys show different behavior by increasing h, especially for Al-3 and Al-8.4 at% Cu.

Due to low CM interfacial energy anisotropy, a morphology known as seaweed structure forms during solidification with a morphology very sensitive to cooling condition (discussed in section 3.5). On the other hand, in alloys with 6 and 10.6 at% Cu dendritic morphology is dominant in all heat transfer coefficients. In order to gain further insights into the effect of Cu content and cooling condition on the solidification microstructure of Al-Cu alloys, it is necessary to quantitatively show how microstructure characteristics change with these parameters. figure 4.7(a) and figure 4.7(b) compare simulations and analytical results of primary dendrite arm spacing (λ_1) and secondary dendrite arm spacing (λ_2) at different heat transfer coefficients.

A few analytical models have been proposed for predicting λ_1 [380, 385-387] and all of them have a similar form to the model presented by Dantzig and Rappaz [58]:

$$\lambda_1 = \left(\frac{72\pi^2 \Gamma_{sl} D_l \Delta T_0}{k_e}\right)^{\frac{1}{4}} (v^*)^{-\frac{1}{4}} (G)^{-\frac{1}{2}} \qquad (4.14)$$

Γ_{sl} is the Gibbs-Thomson coefficient, D_l is diffusion coefficient of solute atom in liquid, and ΔT_0 is freezing range. For the analytical solutions presented in figure 4.7, the material properties are obtained from MD and Thermo-Calc simulations. In addition, the processing conditions, namely the interface velocity (v^*) and the temperature gradient (G), are obtained

from phase-field simulation results. The required data and the procedure for calculation of dendrite arm spacings via analytical solutions are represented in appendix 2.

In figure 4.7(a), λ_1 decreases by increasing the heat transfer coefficient and Cu content. These results agree with the experimental measurements [372, 388, 389] and analytical solutions presented in figure 4.7(a). Furthermore, it can be seen from this figure that the effect of Cu content on λ_1 is more pronounced at a lower cooling rate (h=0.5 W/cm^{2}K) and decreases with an increase in h. Based on Eq. 4.14, the parameters affecting λ_1 are divided into two main groups: material properties and processing conditions. Considering the data in Table A.2 (in the Appendix), for h=0.5 W/cm^{2}K, the net effect of the processing condition ($(v^*)^{-\frac{1}{4}}(G)^{-\frac{1}{2}}$) considerably decreases with Cu content. But for other two h values, the decrease of $(v^*)^{-\frac{1}{4}}(G)^{-\frac{1}{2}}$ with the increase of Cu content is minor. In addition, material properties effect in Eq. 4.14 show a decreasing behavior by increasing Cu content. Both D_l and ΔT_0 decrease with increasing Cu content [390] and their values are presented in Table A.1 (in the Appendix). Also, for a 2D simulation of a crystal with four-fold symmetry, the Gibbs-Thomson coefficient is given by [391]:

$$\Gamma_{sl} = \frac{\gamma_0(1-15\varepsilon_4(\cos 4\varphi))}{\rho \Delta s_f} \tag{4.15}$$

where ρ is alloy density, and Δs_f is entropy of fusion. The value of Γ_{sl} for alloys with 3, 6, 8.4, and 10.6 at% Cu are 6.63×10^{-8}, 4.83×10^{-8}, 5.25×10^{-8}, and 5.16×10^{-8} Km, respectively. (presented in the Appendix). Overall, the decrease of D_l and ΔT_0, and the oscillating change of Γ_{sl} with the increase of Cu lead to decrease of λ_1 with Cu.

The analytical model for calculation of λ_2 was presented by Dantzig and Rappaz [58]:

$$\lambda_2 = 5.5\left(-\frac{\Gamma_{sl}D_l\ln\left(\frac{C_{eut}}{C_0}\right)}{m_l(1-k_e)(C_{eut}-C_0)}\right)^{\frac{1}{3}}\left(\frac{\Delta T_0}{Gv^*}\right)^{\frac{1}{3}} \quad (4.16)$$

where C_{eut} is the final composition of liquid just before solidification, and m_l is the local temperature-concentration slope at the liquidus line of the given alloy, which are both extracted from Thermo-Calc simulation. Figure 4.7(b) shows that λ_2 decreases by increasing h and Cu content, but again the rate of change is higher with Cu at h=0.5 W/cm^{2}K. In all cases, increasing Cu content decreases λ_2 indicating that finer microstructures are obtained at higher Cu contents, which is in agreement with experimental observations [388] and analytical models [58, 392, 393].

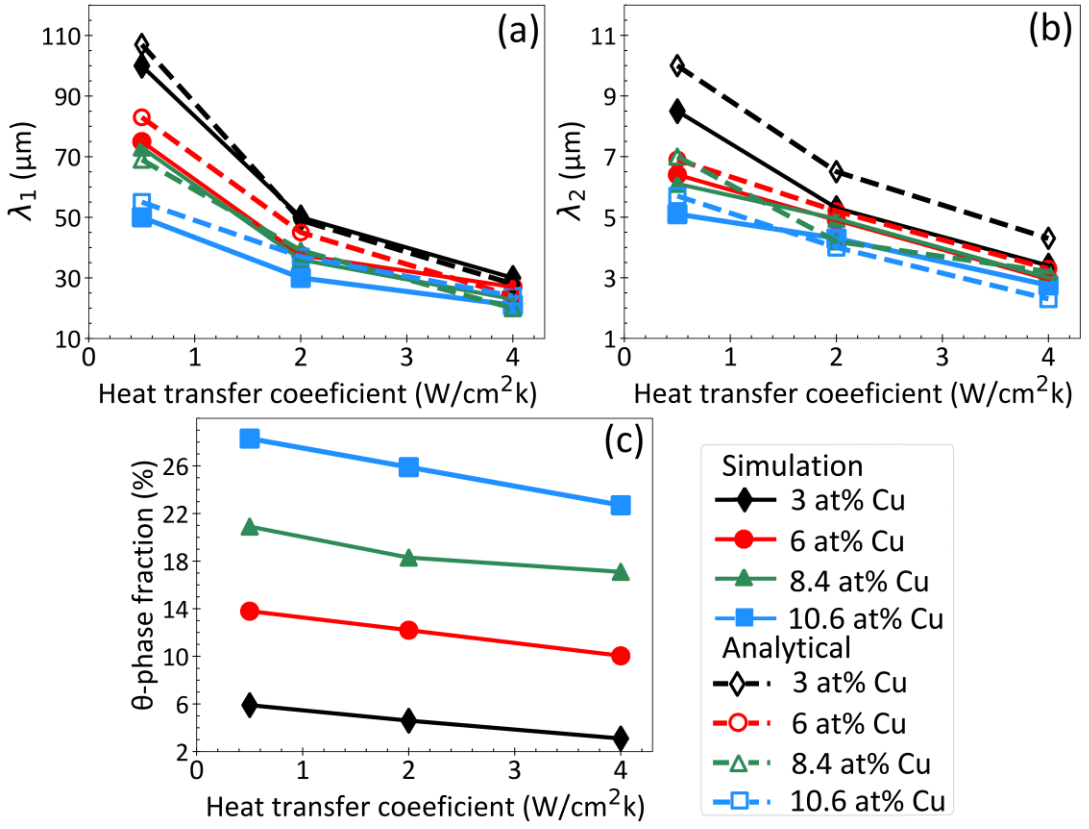

Figure 4.7. Effect of heat transfer coefficient content on (a) λ_1, (b) λ_2, and (c) θ-phase fraction for different alloys.

From Eq. 4.14-4.16, it is obvious that the effect of CM interfacial energy anisotropy on dendrite arm spacings is mixed with the influence of other material properties which results in decrease of arm spacings with Cu content. But, it should be mentioned that the main effect of CM interfacial energy anisotropy is on pattern formation during solidification of θ-Phase (discussed in section 3.5) which have great effect on final microstructure especially distribution of phases.

Figure 4.7(c) shows the effect of heat transfer coefficient on the θ-phase fraction (θ-PF) in the investigated alloys. The results show that by increasing h, the amount of θ-phase for all alloys decreases linearly. This behavior has been observed in experimental work too [388]. In all alloys, θ-phase forms via eutectic reaction but at different undercooling which is imposed by different heat transfer coefficients. Figure 4.8 shows the phase fraction change as a function of time for different alloys and heat transfer coefficients. This figure indicates that in equilibrium conditions (obtained from Thermo-Calc) eutectic reaction takes place at 820.75 K. When h=0.5 W/cm^2K, eutectic reaction takes place at 819.4 K (1.3 undercooling) in all alloys and results in the formation of a eutectic structure. In this condition, the amount of θ-phase is less than equilibrium for all alloys because more θ-phase has formed before the nucleation of θ-phase. For example, in the case of Al- 6at% Cu, nucleation of θ-phase in equilibrium condition takes place when the amount of liquid is equal to 23% but at h=0.5 W/cm^2K the amount of liquid is 21% before θ-phase nucleation. The eutectic structure is shown in figure 4.9 for Al-10.6 at% Cu, where it is obvious that α+θ phases simultaneously grow within the liquid phase.

The eutectic structure is not completely lamellar and consists of both lamellar and wavy structures, which was also observed in experimental studies [394, 395]. The lamellar spacing is 1.2±0.2 μm for all alloys at h=0.5 W/cm^{2}K.

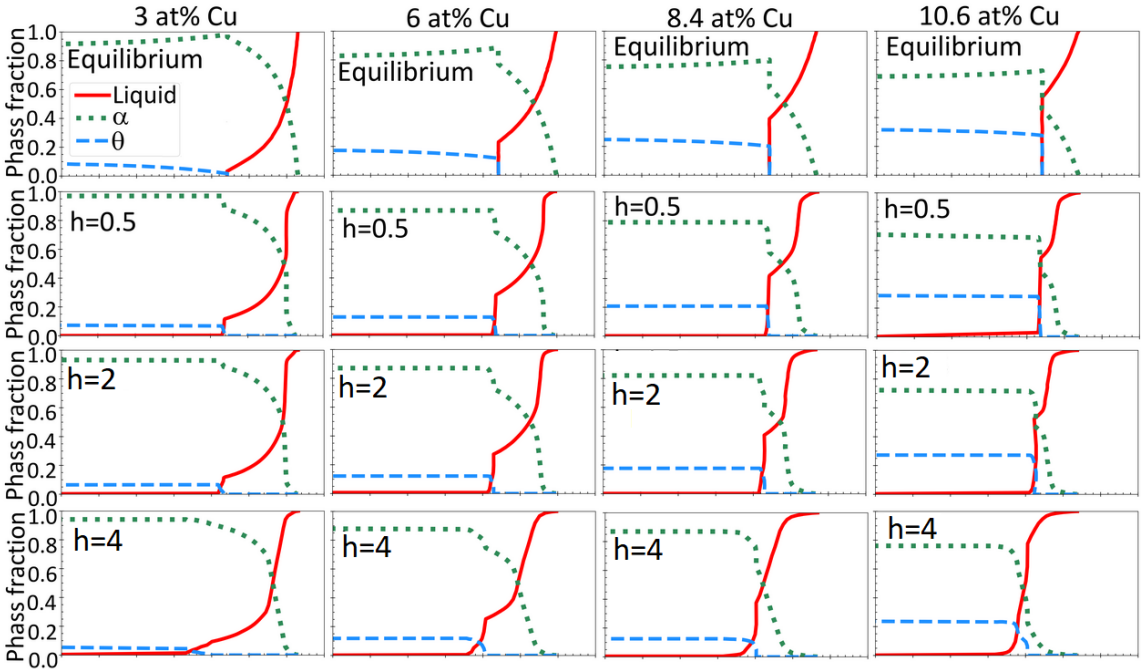

Figure 4.8. Effect of heat transfer coefficient and Cu content on solidification path of Al-Cu alloys.

By increasing h to 2 W/cm^{2}K, eutectic reaction starts at 813.6 K (7.15 K undercooling). In this situation, a higher amount of h α-phase forms before nucleation of θ-phase and less liquid will transform into a α+θ structure via eutectic reaction (18% liquid in the case of Al-6 at% Cu). Also, due to higher cooling rates, all Cu atoms cannot segregate from the θ-phase into interdendritic region and coring takes place [396, 397], and consequently the amount of θ-phase decreases. In this condition, the lamellar spacing is 0.7 ±0.1 μm for all alloys. By increase h to 4 W/cm^{2}K, θ-phase starts to form at 803±4 K (17-21 K undercooling) through both eutectic

reaction and direct solidification from enriched liquid. In this situation, the amount of liquid phase before eutectic reaction has decreased even more (14.5% in the case of Al-6 at% Cu) and coring is more severe, which results in a reduction of θ-phase. It is obvious from last row in Figure 4.8 that the θ-phase doesn't form at a constant temperature (eutectic reaction) which implies that eutectic reaction is partly suppressed at this high cooling rate. In addition to the variation of θ-phase fraction with Cu content and heat transfer coefficient, its distribution also changes considerably with these parameters. It can be seen in figure 4.6 that at a constant heat transfer coefficient, h, θ-phase distribution is more homogenous in Al-3 and Al-8.4 at% Cu alloys than Al-6 and Al-10.6 at% Cu. In the latter cases, dendritic morphology is dominant and θ-phase forms in interdendritic regions, while in the former cases, primary α-phase solidifies as a seaweed structure and θ-phase forms between seaweed branches. The underlaying reasons for the different structures of α-phase during solidification have been discussed in the next section.

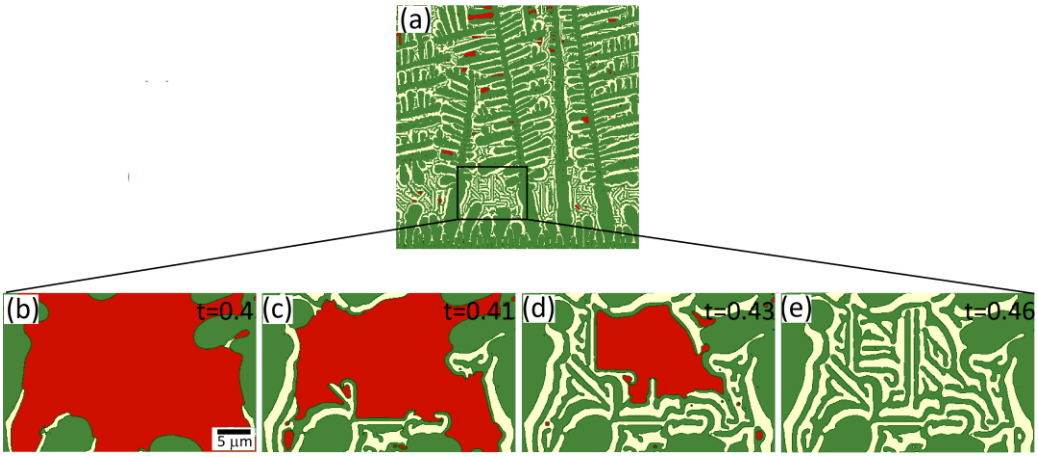

Figure 4.9. (a) The solidified structure of Al-10.6 at% Cu solidified at h=0.5 W/cm2K. (b-e) different snapshots that show sequence of eutectic structure formation via eutectic reaction.

In all investigated alloys by increasing heat transfer coefficient, the distribution of phase becomes more homogenous but this homogenization is more noticeable in alloys with 3 and 8.4 at% Cu. In these alloys, tip splitting frequency increases considerably by heat transfer coefficient. As a consequent, the distribution of the θ-phase becomes more homogenous. By comparison of the two left columns in figure 4.6, it is completely obvious that θ-phase distribution is more homogenous in seaweed structures (Al-8.4 at% Cu) than dendritic structures (Al-10.6 at% Cu), and θ-phase distribution is more sensitive to heat transfer coefficient in alloys with seaweed structure.

4.4.5 Solidification pattern Formation

Figure 4.10 Shows the Dendritic morphology of the investigated alloys at different cooling conditions when the α-phase fraction in the simulation system is 30%. It can be seen that at h=0.5 W/cm^{2}K different morphologies are formed for different alloys. In the case of alloys with 3 and 8.4 at% Cu, tip splitting occurs during the solidification and results in seaweed structure formation, a common phenomenon during solidification of alloys with weak CM interfacial energy anisotropy [75-78, 81, 82, 86, 87, 398-400]. While, in alloys with 6 and 10.6 at% Cu, dendritic solidification takes place without any tip splitting. Since the anisotropy of CM interfacial energy is high for Al-6 and Al-10.6 at% Cu alloys, dendritic growth is dominant in these alloys at all investigated cooling conditions. On the other hand, in the case of Al-3 and Al-8.4 at% Cu, the anisotropy of interfacial energy is much lower, which results in the formation of different seaweed structures like stabilized [86], degenerate or fractal seaweed (FS) [76, 86], and compact seaweed (CS) [76] at different cooling conditions..

Figure 4.10 (a-c) show the structures of solidifying Al-3 at% Cu at different cooling conditions. In figure 4.10 (a), the tips of growing dendrites split off center in such a way that the

larger tip keeps growing as the other falls behind. This growth mode results in the formation of a structure called stabilized seaweed [86]. By increasing heat transfer coefficient to 2 W/cm^{2}K (figure 4.10 (b)), the tip splits to alternate sides producing tips of comparable size which grow as main branches and the splitting will keep happening in each one of them.

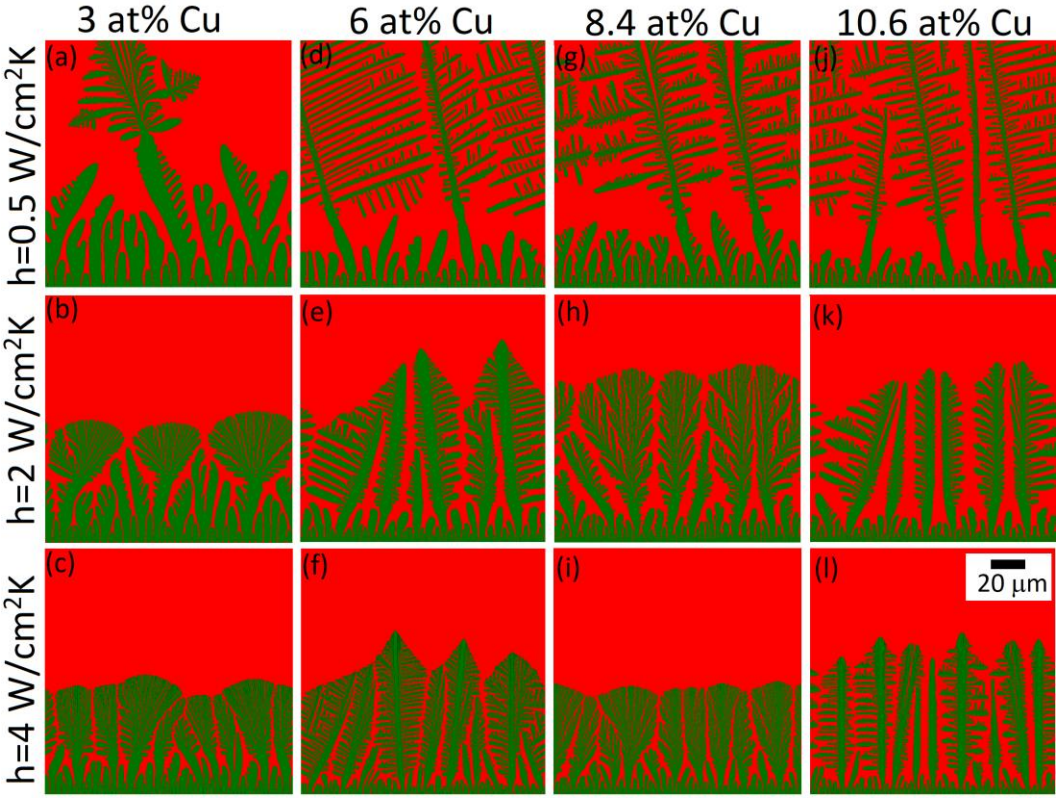

Figure 4.10. Morphology of solidifying α-phase for investigated alloys at different cooling condition when solid phase fraction is 30%.

This structure is called degenerate or FS which is formed by alternating tip splitting [76, 86, 398]. The same structure is formed at h=4 W/cm^{2}K (Figure 4.10 (c)) but the tip splitting frequency (f) is much higher. It has been shown that the tip splitting frequency in FS structure is related to growth velocity (V) as a power law $f \propto V^{1.5}$ [86, 398]. In this study, at h=2 and 4

W/cm^{2}K, *f* is 334 and 538 s^{-1}, respectively, and the related growth velocities are 2900 and 6100 μm/s. Figure 4.10 (g-i) show structures of solidifying Al-8.4 at% Cu at investigated cooling conditions. At h=0.5 W/cm^{2}K (figure 4.10 (g)), a mixture of stabilized and FS is observed. By increasing the heat transfer coefficient to 2 W/cm^{2}K (Figure 4.10 (h)), tip splitting takes place in a nonfractal mode, which results in a structure known as compact seaweed morphology [76, 79, 82] or dense branching [400]. By further increase of heat transfer to 4 W/cm^{2}K, CS forms with higher splitting frequency. During the solidification, dendrites tend to grow in the direction of maximum CM interfacial energy. On the other hand, thermal noises can lead to the destabilization of interface and formation of seaweed structures [80, 82]. When the strength of CM interfacial energy is high, the interface is stable against thermal noises and dendritic morphology with a parabolic tip is dominant, which is the case for Al-6 and Al-10.6 at% Cu. In the case of Al-3 and Al-8.4 at% Cu, the interfacial energy anisotropy is low, and interface destabilizes due to the thermal noise and consequently tip flattens and widens before splitting (Figure 4.11). The details of the tip flattening and splitting mechanisms have been discussed elsewhere [76-78, 82, 86, 398].

As it was elucidated, FS is dominant in Al-3 at% Cu and CS is the dominant structure in Al-8.4 at% Cu, while the strength of interfacial energy anisotropy is weak in both. This difference stems from different constitutional supercooling during solidification. Figure 4.12 (a) and Figure 4.12 (b) show concentration profile and corresponding liquidus line at ahead of growing seaweed for Al-3 and Al-8.4 at% Cu, respectively

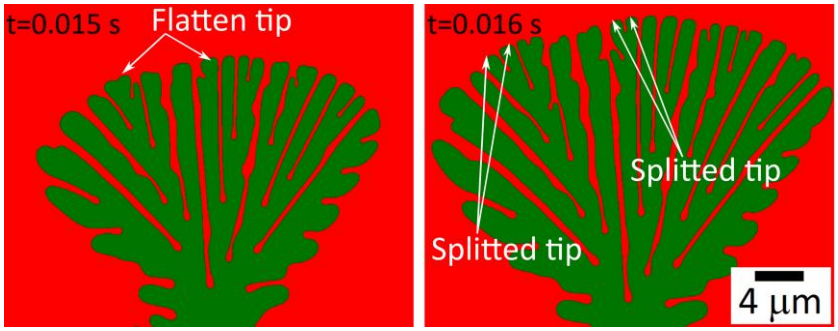

Figure 4.11. Tip flattening and splitting phenomena during solidification of Al-3 at% Cu at h=0.5 W/cm^{2}K.

For the heat transfer coefficient of 4 W/cm^{2}K. For Al-3 at% Cu, the constitutional supercooling is 5.1K exactly at ahead of growing tip and increases to almost 25 K in 6 μm from it. For Al-8.4 at% Cu supercooling is 9.85 K ahead of growing tip and reaches 68 K in 9 μm. At the limit of diffusion control growth, it has been shown that at a low interfacial energy anisotropy and a low supercooling, FS is dominant and with increasing supercooling, a transition is observed and CS becomes dominant [79, 82].

Based on the patterns obtained from phase-field simulations and considering the aforementioned analysis, we construct a map of strength of anisotropy parameter (ε_4) versus constitutional supercooling (Δ) in Figure 4.13 that shows solidification morphology formation in Al-Cu alloys. Regardless of Cu content and supercooling, when the anisotropy parameter value is larger than 0.005 dendritic morphology is dominant and seaweed structure is halted. At a lower anisotropy and supercooling less than 8K, fractal seaweed forms during solidification. While at anisotropies less than 0.005 and supercooling higher than 8K, compact seaweed structure is dominant.

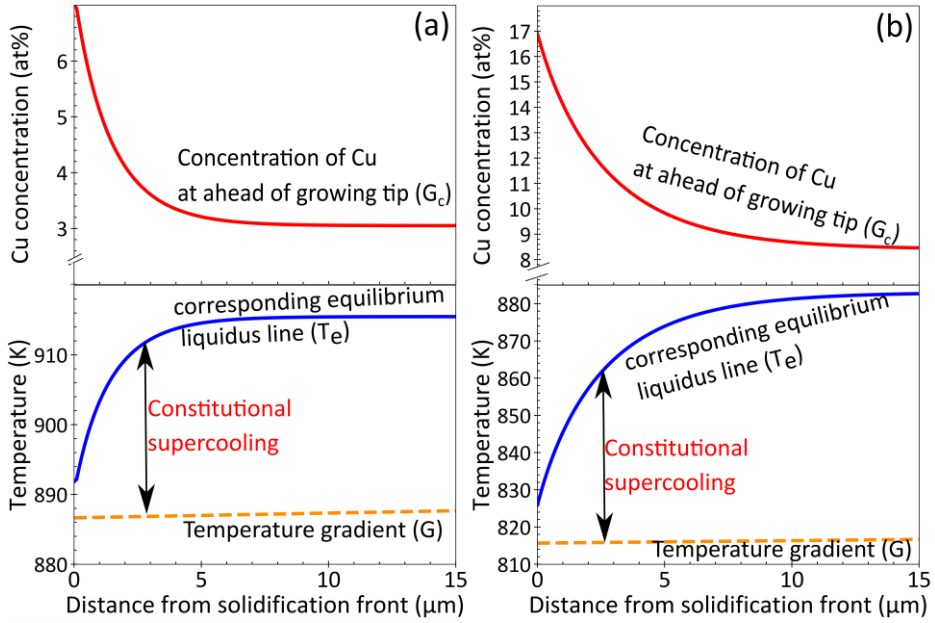

Figure 4.12. Concentration profile at ahead of growing tip and corresponding constitutional supercooling for (a) Al-3 at% Cu, and (b) Al-8.4 at% Cu.

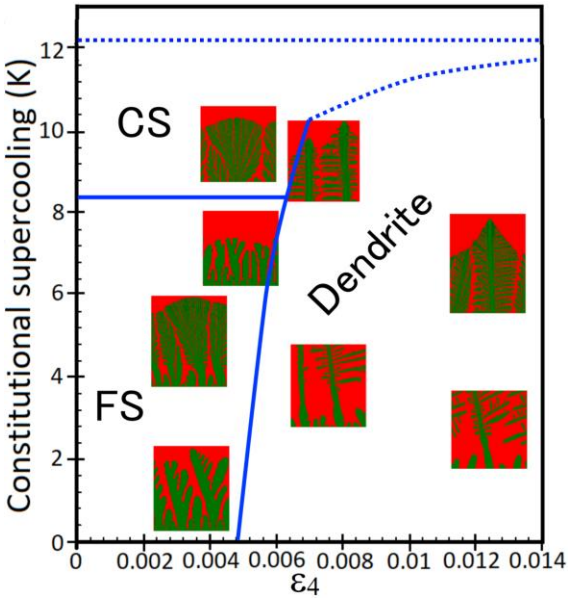

Figure 4.13. Map of morphology formation in Δ-ε_4 plane during solidification of Al-Cu alloys. The dotted lines show the expected trends at higher constitutional supercooling.

4.5 Conclusions

Solidification of four Al-Cu alloys with 3%, 6%, 8.4%, and 10.6 at% Cu was investigated using atomistic-informed multi-phase field modeling. We investigated the combined effects of cooling condition, alloy composition and interfacial energy anisotropy on θ-phase fraction and its distribution, and growth dynamics and morphology of solidification structures. First, the CM interfacial energies and its anisotropy were determined using molecular dynamic simulations. These values were used in phase-field simulations to quantitatively investigate the interactive effects of Cu content, CM interfacial properties, and cooling condition on growth dynamics and solidification patterns. Specific findings include the following:

1- Molecular dynamics simulation results showed that the CM interfacial energy decreases linearly with increasing Cu content while its anisotropy does not show a specific trend.

2- Phase-field simulation results showed that with increasing the cooling rate, the dendrite arm spacing and the amount of θ-phase decrease, and this reduction is more pronounced in alloys with higher Cu content. Also, the θ-phase fraction decreases by increasing the heat transfer coefficient. This reduction is due to the higher undercooling needed for eutectic reaction, which results in the formation of higher α-phase, and less liquid transforms into θ+α phase via eutectic reaction. Furthermore, the coring phenomenon is more noticeable at higher cooling rates which results in a reduction in Cu content in the interdendritic regions and a decrease inθ-phase.

3- Distribution of θ-phase is more homogenous in alloys with seaweed structures (Al-3 and Al-8.4 at% Cu) than the alloys with dendritic structures. In all investigated alloys, the distribution of θ-phase becomes more homogenous by increasing the heat transfer

coefficient, but it is more sensitive to the value of heat transfer coefficient with seaweed structures.

4- Anisotropy of CM interfacial energy has a significant effect on solidification patterns and their growth dynamic. At the limit of diffusion control growth, when the strength of anisotropy is higher than 0.005 dendritic morphology is dominant at all cooling rates. At lower CM interfacial energy anisotropy different seaweed structures can form regarding constitutional supercooling at ahead of growing tip. When supercooling is less than 8K degenerate or fractal seaweed form while at higher supercoolings compact seaweed is dominant microstructure.

4.6 Appendix 1

Eq. A1 was used to calculate the anisotropy parameters in 3D:

$$\gamma(\hat{n}) = \gamma_{0(3D)}[1 + \delta_1(4\sum_{i=1}^{3} n_i^4 - 3) + \delta_2(\sum_{i=1}^{3} n_i^6 + 30n_1^2n_2^2n_3^2)] \quad (4.17)$$

The following 2D equation (Eq. A2) is used for PF simulations:

$$\gamma = \gamma_{0(2D)}\big(1 + \varepsilon_4(\cos 4\varphi)\big) \quad (4.18)$$

Using a series of trigonometric relations, we can calculate ε_4 in 2D as a function of δ_1 and δ_2. Having $n_1 = \cos\varphi$, $n_2 = \sin\varphi$, and $n_3 = 0$, we can rewrite Eq. A1 as follow:

$$\frac{\gamma(\hat{n})}{\gamma_{0(3D)}} = [1 + 4\delta_1(cos^4\varphi + sin^4\varphi - 3/4) + \delta_2(cos^6\varphi + sin^6\varphi)] \quad (4.19)$$

From trigonometric relations we have:

$$cos^4\varphi + sin^4\varphi = (cos^2\varphi + sin^2\varphi)^2 - 2sin^2\varphi\, cos^2\varphi = 1-2sin^2\varphi\, cos^2\varphi\,, \quad (4.20)$$

$$cos^6\varphi + sin^6\varphi = (cos^2\varphi + sin^2\varphi)^3 - 3sin^2\varphi\, cos^2\varphi = 1-3sin^2\varphi\, cos^2\varphi\,, \quad (4.21)$$

$$\sin\varphi\cos\varphi = \frac{1}{2}\sin 2\varphi \Rightarrow sin^2\varphi\, cos^2\varphi = \frac{1}{4}sin^2 2\varphi\,, \tag{4.22}$$

$$sin^2 2\varphi = \frac{1-\cos 4\varphi}{2} \tag{4.23}$$

By substituting Eq. A.4-A.7 into Eq. A.3 we have:

$$\frac{\gamma(n\hat{})}{\gamma_{0(3D)}} = \left[1 + 4\delta_1\left(1 - \frac{1}{4} + \frac{1}{4}\cos 4\varphi - \frac{3}{4}\right) + \delta_2\left(\frac{5}{8} + \frac{3}{8}\cos 4\varphi\right)\right] \tag{4.24}$$

Then:

$$\frac{\gamma(n\hat{})}{\gamma_{0(3D)}} = 1 + \frac{5}{8}\delta_2 + \left(\delta_1 + \frac{3}{8}\delta_2\right)\cos 4\varphi. \tag{4.25}$$

We define X=$1 + \frac{5}{8}\delta_2$ and Y=$\delta_1 + \frac{3}{8}\delta_2$ and divide all terms by X. then we have:

$$\frac{\gamma(n\hat{})}{\gamma_{0(3D)}X} = 1 + \frac{Y}{X}\cos 4\varphi. \tag{4.26}$$

Comparing Eq. A.2 and A.10 we have □$_4$ = $\frac{Y}{X}$ and $\gamma_{0(2D)} = \gamma_{0(3D)}X$. Since X∼1 for all alloys, $\gamma_{0(2D)} = \gamma_{0(3D)}$.

4.7 Appendix 2

The analytical solutions for λ_1 and λ_2 (Equation 13 and 14) include material properties which are obtained from MD simulations and Thermo-Calc databases. The first parameter is Gibbs-Thomson coefficient which is calculated using Eq. A.11.

$$\Gamma_{sl} = \frac{\gamma_{sl} + \gamma''_{sl}}{\rho \Delta s_f} \tag{4.27}$$

where γ_{sl} and γ''_{sl} are CM interfacial energy and its second derivative, respectively. ρ is density and Δs_f is the entropy of fusion. Almost all the dendrites of investigated Al-Cu alloys

have ⟨100⟩ [001] orientation. So, based on Table 1 we can use Eq. A.12 to calculate numerator of Eq. A.11.

$$\gamma_{sl} + \gamma''_{sl} = \gamma_0(1 - 15\delta_1 - 5\delta_2) \tag{4.28}$$

Entropy of fusion, Δs_f, is extracted from Thermo-Calc simulations and $\rho = \frac{wt\%_{Al}+wt\%_{Cu}}{V}$ where $wt\%_{Al}$and $wt\%_{Cu}$ are weight percent of Al and Cu, respectively. V is the volume of 1 kg alloy and is calculated as: $V = \left(\frac{wt\%_{Al}}{\rho_{Al}}\right) + \left(\frac{wt\%_{Cu}}{\rho_{Cu}}\right)$. ρ_{Al} and ρ_{Cu} are equal to 2710 kg/m^3 and 8950 kg/m^3, respectively. Interdiffusion coefficient of Cu atoms at the liquidus temperatures ($\widetilde{D}^{Al}_{CuCu}$), freezing range ($\Delta T_0$), slope of liquidus line (m_l), and final composition of liquid before freezing (c_{eut}) are extracted from Thermo-Calc. All these parameters are presented in Table A.1

Table A.1. Material properties of investigated alloys.

c_0(at%)	c_0(wt%)	c_{eut}(wt%)	$\Delta T_0(K)$	m_l(K/wt%)	$\widetilde{D}^{Al}_{CuCu}$(m^2/s)	Δs_f(J/K.kg)	ρ(kg/m^3)	$\gamma_{sl} + \gamma''_{sl}$(J/m^2)	Γ_{sl}(K.m)
3	6.9	33.49	99	-3.07	5.12E-09	551	2847	0.104	6.63E-08
6	13	33.49	77	-2.93	5.05E-09	541.73	2980	0.0779	4.83E-08
8.4	17.76	33.49	63	-2.91	4.9E-09	512.29	3092	0.0832	5.25E-08
10.6	21.83	33.49	50	-2.89	4.88E-09	484.11	3196	0.0799	5.16E-08

Interface velocity (v^*) and temperature gradient (G) were extracted from phase-field simulations at steady state condition and are presented in Table A.2. Also, in this study the equilibrium partition coefficient, $k_e = 0.185$, is used.

Table A.2- Process dependent parameters of investigated alloys at different heat transfer coefficients.

Cu (at%)	h (W/cm^2.K)	v^* (m/s)	$G \times 10^3$(K/m)	λ_1 (μm)	λ_2 (μm)
3	0.5	0.0024	19.9	107.5	13.7
	2	0.0029	73.5	53.6	8.5
	4	0.0061	16.5	29.7	5
6	0.5	0.0027	21.6	86.9	9.83
	2	0.0038	74.2	43	5.9
	4	0.0072	17.3	24	3.7
8.4	0.5	0.0027	25.2	76.5	8.6
	2	0.0035	75.05	41.6	5.4
	4	0.0068	17.3	23.2	3.3
10.6	0.5	0.0027	29.3	66.5	7.3
	2	0.0037	79.6	37.3	4.7
	4	0.0069	175	21.5	2.93

Acknowledgment

This study was supported by the National Science Foundation, NSF-CMMI 2031800, and by NASA, 80NSSC19K0569. We are grateful for supercomputing time allocation provided by the Extreme Science and Engineering Discovery Environment (XSEDE), award number TG-DMR140008.

CRediT Author Statement

Ghavam Azizi: Conceptualization, Methodology, Software, Formal analysis, Writing-Original draft preparation. Sepideh Kavousi: Conceptualization, Methodology, Formal analysis, Writing- Reviewing and Editing. Mohsen Asle Zaeem: Supervision, Conceptualization, Methodology, Formal analysis, Writing- Reviewing and Editing, Funding Acquisition.

Data availability

All necessary data generated or analyzed during this study are included in this published article, and other auxiliary data are available from the corresponding author on reasonable request.

Declaration of Competing Interest

The authors declare no competing interests.

CHAPTER 5 CONCLUSIONS

Mechanical and physical properties of metals and alloys are greatly influenced by solidification defects which can form in both macro and microscale inside the alloy or at the surface. In this Ph.D. research, by means of computational modeling, we investigated the formation mechanisms of surface defects that form during continuous casting of steels especially peritectic steels. A macro-scale computational framework based on finite element method was developed to understand the effect of carbon on surface defect features of steels. In this work we also investigated solidification pattern formation, microsegregation and second phase formation mechanisms in Al-Cu alloys with cupper content ranging from 3 to 11 at% using an atomistic informed phase field model implemented in MICRESS program. Specific findings include the following:

1. Under equilibrium conditions, peritectic solidification proceeds in two distinct steps: the peritectic reaction, and the peritectic transformation.

2. The peritectic reaction takes places when austenite nucleates and grows as a thin layer along the liquid / δ-ferrite interface at or just below the peritectic temperature. It is governed by diffusion of solute (carbon in plain Fe-C steels), especially in the liquid, and likely also depends on microscale heat transfer that causes local re-melting of δ-ferrite and liquid / solute mixing near the δ/γ/L triple point.

3. The peritectic transformation first involves growth of the austenite layer thickness in both directions: into the liquid (L $\rightarrow\gamma$) on one side, and into the δ-ferrite interior ($\delta\rightarrow\gamma$) on the other side, which separates the δ-ferrite and liquid by a thickening layer of austenite. Some believe that this transformation is controlled by diffusion, especially with low

undercooling below the peritectic temperature. At high undercooling, the transformation is extremely fast, so others believe that the δ→γ transformation is controlled by massive transformation.

4. At very high undercooling and transformation rates, some claim that the peritectic reaction is suppressed, due to either nucleation constraint, or to solute flux gradients, so the initial austenite layer never grows along the δ / L interface and the entire peritectic solidification process is governed by massive transformation.

5. Peritectic steels cause deeper oscillation marks and surface depressions in cast products, relative to other steel grades. This is due to the large shrinkage that accompanies the δ→γ phase transformation, the higher transformation speed, the much higher strength of austenite relative to δ-ferrite, complex thermal-mechanical behavior during solidification, and possibly other factors involving the microstructure evolution.

6. Peritectic steels having deeper surface roughness leads to higher resistance to heat transfer across the interfacial gap during initial solidification in the mold, lower heat flux, uneven shell growth, and thin regions in the solidifying steel shell, which have hotter local surface temperature. These thin, weak, hot spots lead to local strain concentration and make peritectic steels more susceptible to breakouts and hot-tearing cracks, especially internal cracks and longitudinal surface cracks, relative to other grades.

7. Carbon content is the main factor that controls thermal distortion and bottom surface shape during steel solidification. The highest distortion, as indicated by the curvature of bottom surface of the droplet, is found in ultra-low carbon and peritectic steel grades.

8. Heat flux also plays an important role in controlling thermal distortion during solidification. Increasing heat flux during the initial stages of solidification causes the gap depth (curvature of solidified droplet surface) to increase. This effect is most evident in ultralow carbon steels, and decreases with increasing carbon content, if the heat flux does not suddenly change.

9. A sudden drop in heat flux typically accompanies gap formation, and is called the incubation time. This causes surface reheating, thermal expansion of the surface layer, and a very large increase in the gap depth, for all steel grades.

10. Shorter incubation times lead to deeper gaps, owing to the higher temperature gradient across the thinner shell when the thermal distortion occurs.

11. For every steel grade and heat flux condition investigated, the gap forms very early during solidification, within 0.06s for fast cooling and within 0.4s for slow cooling, and remains relatively constant after that. The heat flux rate at later times, after the first 1s, has little effect on the final thermally-distorted shape.

12. The incubation time for gap formation is usually near or after the start of the $\delta \rightarrow \gamma$ phase transformation, which is controlled by the steel grade and initial heat flux. Thus, the gap forms sooner with faster initial cooling rates, and in peritectic steels.

13. The gap depth is greatly affected by the $\delta \rightarrow \gamma$ phase transformation. In peritectic steel grades, this transformation occurs very soon after a thin solid shell has formed, which leads to deep gaps, implying deep surface depressions in cast products.

14. Increasing the cooling rate and temperature gradient during initial solidification increases the severity of $\delta \rightarrow \gamma$ phase transformation, and results in a deeper gap.

15. The findings of this fundamental model and gap formation mechanism have important implications for the formation of surface depressions and related defects in commercial steel continuous casting processes.

16. Molecular dynamics simulation results showed that the CM interfacial energy decreases linearly with increasing Cu content while its anisotropy does not show a specific trend.

17. Phase-field simulation results showed that with increasing the cooling rate, the dendrite arm spacing and the amount of θ-phase decrease, and this reduction is more pronounced in alloys with higher Cu content. Also, the θ-phase fraction decreases by increasing the heat transfer coefficient. This reduction is due to the higher undercooling needed for eutectic reaction, which results in the formation of higher α-phase, and less liquid transforms into θ+α phase via eutectic reaction. Furthermore, the coring phenomenon is more noticeable at higher cooling rates which results in a reduction in Cu content in the interdendritic regions and a decrease inθ-phase.

18. Distribution of θ-phase is more homogenous in alloys with seaweed structures (Al-3 and Al-8.4 at% Cu) than the alloys with dendritic structures. In all investigated alloys, the distribution of θ-phase becomes more homogenous by increasing the heat transfer coefficient, but it is more sensitive to the value of heat transfer coefficient with seaweed structures.

19. Anisotropy of CM interfacial energy has a significant effect on solidification patterns and their growth dynamic. At the limit of diffusion control growth, when the strength of anisotropy is higher than 0.005 dendritic morphology is dominant at all cooling rates. At lower CM interfacial energy anisotropy different seaweed structures can form regarding

constitutional supercooling at ahead of growing tip. When supercooling is less than 8K degenerate or fractal seaweed form while at higher supercoolings compact seaweed is dominant microstructure.

CHAPTER 6 FUTURE WORKS

In this thesis we investigated the thermal distortion formation during steel solidification in macroscale level using our finite element model. The next step to gain deeper understanding of defect formation should be done by microscale modeling to investigate the effect of solidification mechanism in different grades on surface defect formation. To this end, quantitative phase-field modeling in which all the interfacial energies are known would be the best option.

Understanding solidification behavior of alloys in microgravity situation is a very important step for space exploration process. In this matter, it is necessary to know how interfacial energies and surface tensions influence solidification pattern formation in microgravity conditions.

Considering these, following potential future works are suggested:

1- We speculate that in addition to $\delta \rightarrow \gamma$ phase transformation rate the direction of this transformation has a great effect on stress distribution during solidification and consequently on thermal distortion. To this end, phase field modeling of steel solidification should be performed in order to investigate the effect of carbon content on phase transformation sequence and direction in microscale.
2- Since phase field modeling is a phenomenological approach to make phase field modeling quantitative, one needs to have exact physical properties including crystal-melt interfacial energy properties to correctly simulate microstructure evolution and phase

transformation kinetics during steel solidification. Molecular dynamic simulations should be performed for Fe-C alloys to calculate interfacial energy and its anisotropy.

3- During solidification, stress and strain distribution are the main reason for surface defect formation. In order to predict stress distribution in micro level the phase field model should be coupled with stress model to study the effect of $\delta \rightarrow \gamma$ phase transformation rate and direction on stress and strain distribution during steel solidification.

4- As we showed in this Ph.D. thesis, crystal-melt interfacial energy and related anisotropy play a crucial role on pattern formation during solidification of metals and alloys in terrestrial condition. In microgravity condition and absence of earth gravity, when there is no buoyancy force the properties of interfacial energies (solid-liquid and liquid-gas) dominant the solidification mechanism and determine the characteristics of both macro and microscale defects. In order to predict the effects of gravity level on microstructure evolution and defect formation during solidification the phase field model should be coupled with Naiver- Stokes equations.

REFERENCES

1 G.K. Sigworth and C. Wang, "Mechanisms of porosity formation during solidification: A theoretical analysis," *Metallurgical transactions B,* vol. 24, no. 2, pp. 349-364, 1993.

2 A. Ludwig, M. Wu, and A. Kharicha, "On macrosegregation," *Metallurgical and Materials Transactions A,* vol. 46, no. 11, pp. 4854-4867, 2015.

3 V. Khalajzadeh and C. Beckermann, "Simulation of shrinkage porosity formation during alloy solidification," *Metallurgical and Materials Transactions A,* vol. 51, no. 5, pp. 2239-2254, 2020.

4 J. Brimacombe and K. Sorimachi, "Crack formation in the continuous casting of steel," *Metallurgical transactions B,* vol. 8, no. 2, pp. 489-505, 1977.

5 V. Uthaisangsuk, et al., "A study of microcrack formation in multiphase steel using representative volume element and damage mechanics," *Computational Materials Science,* vol. 50, no. 4, pp. 1225-1232, 2011.

6 C. Pequet, M. Rappaz, and M. Gremaud, "Modeling of microporosity, macroporosity, and pipe-shrinkage formation during the solidification of alloys using a mushy-zone refinement method: applications to aluminum alloys," *Metallurgical and Materials Transactions A,* vol. 33, no. 7, pp. 2095-2106, 2002.

7 D. Kirkwood, "Microsegregation," *Materials Science and Engineering,* vol. 65, no. 1, pp. 101-109, 1984.

8 B. G. Thomas, "Review on modeling and simulation of continuous casting," *steel Res. Int.,* vol. 89, no. 1, pp. 1700312, 2018.

9 J.K. Brimacombe and K. Sorimachi, "Crack formation in the continuous casting of steel," *Metall. Mater. Trans. B,* vol. 8, no. 2, pp. 489-505, 1977.

10 P. Lyu, W. Wang, and H. Zhang, "Mold Simulator Study on the Initial Solidification of Molten Steel Near the Corner of Continuous Casting Mold," *Metall. Mater. Trans. B,* vol. 48, no. 1, pp. 247-259, 2017.

11 M. Wolf and W. Kurz, "The effect of carbon content on solidification of steel in the continuous casting mold," *Metall. Mater. Trans. B,* vol. 12, no. 1, pp. 85-93, 1981.

12 J. Sengupta, et al., "A new mechanism of hook formation during continuous casting of ultra-low-carbon steel slabs," *Metall. Mater. Trans. A,* vol. 37, no. 5, pp. 1597-1611, 2006.

13 A. Grill, K. Sorimachi, and J.K. Brimacombe, "Heat flow, gap formation and break-outs in the continuous casting of steel slabs," *Metall. Trans. B,* vol. 7, no. 2, pp. 177-189, 1976.

14 A. Badri, et al., "A mold simulator for continuous casting of steel: Part II. The formation of oscillation marks during the continuous casting of low carbon steel," *Metall. Mater. Trans. B,* vol. 36, no. 3, pp. 373-383., 2005.

15 K. Schwerdtfeger and H. Sha, "Depth of oscillation marks forming in continuous casting of steel," *Metall. Trans. B,* vol. 31, no. 4, pp. 813-826, 2000.

16 K. Kim, et al., "Analysis of surface and internal cracks in continuously cast beam blank," *Ironmak. Steelmak.,* vol. 24, no. 3, pp. 249-256, 1997.

17 Y. Maehara, et al., "Surface cracking mechanism of continuously cast low carbon low alloy steel slabs," *Mater. Sci. Tech.,* vol. 6, no. 9, pp. 793-806, 1990.

18 G. Kasperovich, et al., "Microsegregation during solidification of an Al-Cu binary alloy at largely different cooling rates (0.01 to 20,000 K/s): modeling and experimental study," *Metallurgical and Materials Transactions A,* vol. 39, no. 5, pp. 1183-1191, 2008.

19 Q. Du, et al., "Two-dimensional modelling and experimental study on microsegregation during solidification of an Al–Cu binary alloy," *Acta materialia,* vol. 55, no. 5, pp. 1523-1532, 2007.

20 J. Quaresma, C.A. Santos, and A. Garcia, "Correlation between unsteady-state solidification conditions, dendrite spacings, and mechanical properties of Al-Cu alloys," *Metallurgical and Materials Transactions A,* vol. 31, no. 12, pp. 3167-3178, 2000.

21 S. Singh and K. Blazek, "Heat transfer and skin formation in a continuous-casting mold as a function of steel carbon content," *JOM,* vol. 26, no. 10, pp. 17-27, 1974.

22 T. Emi and H. Fredriksson, "High-speed continuous casting of peritectic carbon steels," *Materials Science and Engineering: A,* vol. 413, no. pp. 2-9, 2005.

23 J. Konishi, et al., "Modeling the formation of longitudinal facial cracks during continuous casting of hypoperitectic steel," *Metallurgical and materials transactions B,* vol. 33, no. 3, pp. 413-423, 2002.

24 M. Suzuki, et al., "Origin of heat transfer anomaly and solidifying shell deformation of peritectic steels in continuous casting," *ISIJ international,* vol. 36, no. Suppl, pp. S171-S174, 1996.

25 A. Grill, K. Sorimachi, and J. Brimacombe, "Heat flow, gap formation and break-outs in the continuous casting of steel slabs," *Metallurgical transactions B,* vol. 7, no. 2, pp. 177-189, 1976.

26 M. Suzuki and Y. Yamaoka, "Influence of carbon content on solidifying shell growth of carbon steels at the initial stage of solidification," *Materials transactions,* vol. 44, no. 5, pp. 836-844, 2003.

27 J. Xu, et al., "Analysis of crack susceptibility of regular carbon steel slabs using volume-based shrinkage index," *ISIJ international,* vol. 53, no. 10, pp. 1812-1817, 2013.

28 R. Kuziak, R. Kawalla, and S. Waengler, "Advanced high strength steels for automotive industry," *Archives of civil and mechanical engineering,* vol. 8, no. 2, pp. 103-117, 2008.

29 D.M. Stefanescu, "Microstructure evolution during the solidification of steel," *ISIJ international,* vol. 46, no. 6, pp. 786-794, 2006.

30 W. Bosze and R. Trivedi, "On the kinetic expression for the growth of precipitate plates," *Metallurgical Transactions,* vol. 5, no. pp. 511-512, 1974.

31 Y. Chuang, D. Reinisch, and K. Schwerdtfeger, "Kinetics of the diffusion controlled peritectic reaction during solidification of iron-carbon-alloys," *Metallurgical and Materials Transactions A,* vol. 6, no. 1, pp. 235-238, 1975.

32 H. Nassar, "On peritectic reactions and transformations and hot forming of cast structures*"*, in *KTH, Stockholm, Sweden, pp. 23-24.* 2009.

33 H. Fredriksson and T. Nylen, "Mechanism of peritectic reactions and transformations," *Metal Science,* vol. 16, no. 6, pp. 283-294, 1982.

34 K. Matsuura, Y. Itoh, and T. Narita, "A solid-liquid diffusion couple study of a peritectic reaction in iron-carbon system," *ISIJ international,* vol. 33, no. 5, pp. 583-587, 1993.

35 D. Phelan, M. Reid, and R. Dippenaar, "Kinetics of the peritectic reaction in an Fe–C alloy," *Mater. Sci. Eng. A,* vol. 477, no. 1-2, pp. 226-232, 2008.

36 S. Griesser, C. Bernhard, and R. Dippenaar, "Effect of nucleation undercooling on the kinetics and mechanism of the peritectic phase transition in steel," *Acta materialia,* vol. 81, no. pp. 111-120, 2014.

37 M. Yoshiya, et al., "Interface energies of hetero-and homo-phase boundaries and their impact on δ-γ massive-like phase transformations in carbon steel*"*, in *Materials transactions,2015, Vol. 56, No. 9, pp. 1461-1466.* 2015.

38 S. Griesser, C. Bernhard, and R. Dippenaar, "Mechanism of the peritectic phase transition in Fe–C and Fe–Ni alloys under conditions close to chemical and thermal equilibrium," *ISIJ international,* vol. 54, no. 2, pp. 466-473, 2014.

39 H. Shibata, et al., "Kinetics of peritectic reaction and transformation in Fe-C alloys," *Metallurgical and Materials Transactions B,* vol. 31, no. 5, pp. 981-991, 2000.

40 L. Luo, et al., "Peritectic reaction and its influences on the microstructures evolution during directional solidification of Fe–Ni alloys," *Journal of alloys and compounds,* vol. 461, no. 1-2, pp. 121-127, 2008.

41 Y. Arai, et al., "In-situ observed dynamics of peritectic solidification and δ/γ transformation of Fe-3 to 5 at. pct Ni alloys," *Metallurgical and Materials Transactions A,* vol. 36, no. 11, pp. 3065-3074, 2005.

42 B.K. Dhindaw, et al., "Characterization of the peritectic reaction in medium-alloy steel through microsegregation and heat-of-transformation studies," *Metallurgical and Materials Transactions A,* vol. 35, no. 9, pp. 2869-2879, 2004.

43 H. Yasuda, et al. "In-situ observation of peritectic solidification in Sn-Cd and Fe-C alloys," *in IOP conference series: materials science and engineering. 2012*. IOP Publishing.

44 J.S. Lee, et al., "Numerical simulation of peritectic reaction using a multi-phase-field model," *ISIJ international,* vol. 39, no. 7, pp. 730-736, 1999.

45 M. Ohno and K. Matsuura, "Quantitative phase-field modeling for two-phase solidification process involving diffusion in the solid," *Acta materialia,* vol. 58, no. 17, pp. 5749-5758, 2010.

46 M. Ohno and K. Matsuura, "Diffusion-controlled peritectic reaction process in carbon steel analyzed by quantitative phase-field simulation," *Acta materialia,* vol. 58, no. 18, pp. 6134-6141, 2010.

47 "H. Shibata, Y. Arai, M. Suzuki, T. Emi, Kinetics of peritectic reaction and transformation in Fe-C alloys, Metall. Mater. Trans. B, 2000, Vol. 31(5), p. 981-991.," vol. no.,

48 Y. Ueshima, et al., "Analysis of solute distribution in dendrites of carbon steel with δ/γ transformation during solidification," *Metallurgical Transactions B,* vol. 17, no. 4, pp. 845-859, 1986.

49 D. Phelan, M. Reid, and R. Dippenaar, "Kinetics of the peritectic phase transformation: In-situ measurements and phase field modeling," *Metallurgical and Materials Transactions A,* vol. 37, no. 3, pp. 985-994, 2006.

50 S. Griesser, et al., "Diffusional constrained crystal nucleation during peritectic phase transitions," *Acta materialia,* vol. 67, no. pp. 335-341, 2014.

51 T. Nishimura, et al. "Kinetics of the δ/γ interface in the massive-like transformation in Fe-0.3 C-0.6 Mn-0.3 Si alloys," *in IOP Conference Series: Materials Science and Engineering. 2015*. IOP Publishing.

52 A. Grill and J. Brimacombe, "Influence of C Content on Rate of Heat Extraction in the Mould of a Continuous-Casting Machine," *Ironmak. Steelmak.,* vol. 3, no. pp. 76-79, 1976.

53 H. Yasuda, et al. "Massive transformation from δ phase to γ phase in Fe–C alloys and strain induced in solidifying shell," *in IOP conference series: materials science and engineering. 2012*. IOP Publishing.

54 "M. Suzuki, C. H. Yu, H. Sato, Y. Tsui, H. Shibata, T. Emi, Origin of heat transfer anomaly and solidifying shell deformation of peritectic steels in continuous casting, ISIJ Int., 1996, 36, p. S171-S174.," vol. no.,

55 Y.M. Won, et al., "A new criterion for internal crack formation in continuously cast steels," *Metallurgical and Materials Transactions B,* vol. 31, no. 4, pp. 779-794, 2000.

56 L. Wang, et al., "Controlling solid-liquid interfacial energy anisotropy through the isotropic liquid," *Nature communications,* vol. 11, no. 1, pp. 1-7, 2020.

57 S.H. Davis, *Theory of solidification*. 2001: Cambridge University Press.

58 J.A. Dantzig and M. Rappaz, *Solidification: -Revised & Expanded*. 2016, New York: EPFL press.

59 M.E. Glicksman, *Principles of solidification: an introduction to modern casting and crystal growth concepts*. 2010: Springer Science & Business Media.

60 J. Yang and W. Hu, "Nucleation and solid–liquid interfacial energy of Li nanoparticles: a molecular dynamics study," *physica status solidi (b),* vol. 253, no. 10, pp. 1941-1946, 2016.

61 Y. Shibuta, et al., "Heterogeneity in homogeneous nucleation from billion-atom molecular dynamics simulation of solidification of pure metal," *Nature communications,* vol. 8, no. 1, pp. 1-9, 2017.

62 M. Rappaz, et al., "The influence of solid–liquid interfacial energy anisotropy on equilibrium shapes, nucleation, triple lines and growth morphologies," *Scripta materialia,* vol. 62, no. 12, pp. 904-909, 2010.

63 W.J. Boettinger, et al., "Solidification microstructures: recent developments, future directions," *Acta materialia,* vol. 48, no. 1, pp. 43-70, 2000.

64 J.S. Langer, "Instabilities and pattern formation in crystal growth," *Reviews of modern physics,* vol. 52, no. 1, pp. 1, 1980.

65 J. Hoyt, et al., "Crystal–melt interfaces and solidification morphologies in metals and alloys," *MRS bulletin,* vol. 29, no. 12, pp. 935-939, 2004.

66 T. Haxhimali, et al., "Orientation selection in dendritic evolution," *Nature materials,* vol. 5, no. 8, pp. 660-664, 2006.

67 S. Coriell and R. Sekerka, "The effect of the anisotropy of surface tension and interface kinetics on morphological stability," *Journal of crystal growth,* vol. 34, no. 2, pp. 157-163, 1976.

68 P. Kopczyński, W.-J. Rappel, and A. Karma, "Critical role of crystalline anisotropy in the stability of cellular array structures in directional solidification," *Physical review letters*, vol. 77, no. 16, pp. 3387, 1996.

69 A.A. Golovin and S.H. Davis, "Effect of anisotropy on morphological instability in the freezing of a hypercooled melt," *Physica D: Nonlinear Phenomena,* vol. 116, no. 3-4, pp. 363-391, 1998.

70 R. Trivedi, "Effects of anisotropy properties on interface pattern formation," *Appl. Mech. Rev.* , vol. 43, no. 55, pp. S79-S84, 1990.

71 W.W. Mullins and R. Sekerka, "Stability of a planar interface during solidification of a dilute binary alloy," *Journal of applied physics,* vol. 35, no. 2, pp. 444-451, 1964.

72 G. Young, S. Davis, and K. Brattkus, "Anisotropic interface kinetics and tilted cells in unidirectional solidification," *Journal of crystal growth,* vol. 83, no. 4, pp. 560-571, 1987.

73 H. Xing, et al., "Effect of interface anisotropy on growth direction of tilted dendritic arrays in directional solidification of alloys: insights from phase-field simulations," *International Journal of Heat and Mass Transfer,* vol. 104, no. pp. 607-614, 2017.

74 F. Yu and Y. Wei, "Effect of surface tension anisotropy and welding parameters on initial instability dynamics during solidification: a phase-field study," *Metallurgical and Materials Transactions A,* vol. 49, no. 8, pp. 3293-3305, 2018.

75 T. Ihle and H. Müller-Krumbhaar, "Diffusion-limited fractal growth morphology in thermodynamical two-phase systems," *Physical review letters,* vol. 70, no. 20, pp. 3083, 1993.

76 T. Ihle and H. Müller-Krumbhaar, "Fractal and compact growth morphologies in phase transitions with diffusion transport," *Physical Review E,* vol. 49, no. 4, pp. 2972, 1994.

77 S. Akamatsu, G. Faivre, and T. Ihle, "Symmetry-broken double fingers and seaweed patterns in thin-film directional solidification of a nonfaceted cubic crystal," *Physical Review E,* vol. 51, no. 5, pp. 4751, 1995.

78 M. Georgelin and A. Pocheau, "Onset of sidebranching in directional solidification," *Physical Review E,* vol. 57, no. 3, pp. 3189, 1998.

79 E. Brener, H. Müller-Krumbhaar, and D. Temkin, "Kinetic phase diagram and scaling relations for stationary diffusional growth," *EPL (Europhysics Letters),* vol. 17, no. 6, pp. 535, 1992.

80 E. Brener, et al., "Fluctuation effects on dendritic growth morphology," *Physica A: Statistical Mechanics and its Applications,* vol. 204, no. 1-4, pp. 96-110, 1994.

81 S. Akamatsu and G. Faivre, "Anisotropy-driven dynamics of cellular fronts in directional solidification in thin samples," *Physical Review E,* vol. 58, no. 3, pp. 3302, 1998.

82 E. Brener, H. Müller-Krumbhaar, and D. Temkin, "Structure formation and the morphology diagram of possible structures in two-dimensional diffusional growth," *Physical Review E,* vol. 54, no. 3, pp. 2714, 1996.

83 M. Amoorezaei, S. Gurevich, and N. Provatas, "Orientation selection in solidification patterning," *Acta materialia,* vol. 60, no. 2, pp. 657-663, 2012.

84 H. Xing, et al., "Degenerate seaweed to tilted dendrite transition and their growth dynamics in directional solidification of non-axially oriented crystals: a phase-field study," *Scientific reports,* vol. 6, no. pp. 26625, 2016.

85 H. Xing, et al., "Growth competition between columnar dendrite and degenerate seaweed during directional solidification of alloys: Insights from multi-phase field simulations," *Materials & Design,* vol. 185, no. pp. 108250, 2020.

86 B. Utter and E. Bodenschatz, "Dynamics of low anisotropy morphologies in directional solidification," *Physical Review E,* vol. 66, no. 5, pp. 051604, 2002.

87 Y. Chen, et al., "Tip-splitting instability and transition to seaweed growth during alloy solidification in anisotropically preferred growth direction," *Acta materialia,* vol. 66, no. pp. 219-231, 2014.

88 G.W. Lee, et al., "Crystal–liquid interfacial free energy and thermophysical properties of pure liquid Ti using electrostatic levitation: Hypercooling limit, specific heat, total hemispherical emissivity, density, and interfacial free energy," *The Journal of Chemical Thermodynamics,* vol. 63, no. pp. 1-6, 2013.

89 J.Q. Broughton and G.H. Gilmer, "Molecular dynamics of the crystal–fluid interface. v. structure and dynamics of crystal–melt systems," *The Journal of chemical physics,* vol. 84, no. 10, pp. 5749-5758, 1986.

90 J. Hoyt, M. Asta, and A. Karma, "Method for computing the anisotropy of the solid-liquid interfacial free energy," *Physical review letters,* vol. 86, no. 24, pp. 5530, 2001.

91 J. Hoyt and M. Asta, "Atomistic computation of liquid diffusivity, solid-liquid interfacial free energy, and kinetic coefficient in Au and Ag," *Physical Review B,* vol. 65, no. 21, pp. 214106, 2002.

92 D. Sun, M. Asta, and J. Hoyt, "Kinetic coefficient of Ni solid-liquid interfaces from molecular-dynamics simulations," *Physical Review B,* vol. 69, no. 2, pp. 024108, 2004.

93 E. Asadi and M. Asle Zaeem, "The anisotropy of hexagonal close-packed and liquid interface free energy using molecular dynamics simulations based on modified embedded-atom method," *Acta materialia,* vol. 107, no. pp. 337-344, 2016.

94 E. Asadi, et al., "Quantitative modeling of the equilibration of two-phase solid-liquid Fe by atomistic simulations on diffusive time scales," *Physical Review B,* vol. 91, no. 2, pp. 024105, 2015.

95 E. Asadi, et al., "Two-phase solid–liquid coexistence of Ni, Cu, and Al by molecular dynamics simulations using the modified embedded-atom method," *Acta materialia,* vol. 86, no. pp. 169-181, 2015.

96 S. Kavousi, et al., "Combined molecular dynamics and phase field simulation investigations of crystal-melt interfacial properties and dendritic solidification of highly undercooled titanium," *Computational materials science,* vol. 163, no. pp. 218-229, 2019.

97 R. Ramakrishnan and R. Sankarasubramanian, "Crystal-melt kinetic coefficients of Ni3Al," *Acta materialia,* vol. 127, no. pp. 25-32, 2017.

98 S. Kavousi, et al., "Modified embedded-atom method potential for high-temperature crystal-melt properties of Ti–Ni alloys and its application to phase field simulation of solidification," *Modelling and Simulation in Materials Science and Engineering,* vol. 28, no. 1, pp. 015006, 2019.

99 A. Mahata, T. Mukhopadhyay, and M. Asle Zaeem, "Modified embedded-atom method interatomic potentials for Al-Cu, Al-Fe and Al-Ni binary alloys: From room temperature to melting point," *Computational materials science,* vol. 201, no. pp. 110902, 2022.

100 C. Becker, et al., "Atomistic underpinnings for orientation selection in alloy dendritic growth," *Physical review letters,* vol. 98, no. 12, pp. 125701, 2007.

101 M. Asta, J. Hoyt, and A. Karma, "Calculation of alloy solid-liquid interfacial free energies from atomic-scale simulations," *Physical Review B,* vol. 66, no. 10, pp. 100101, 2002.

102 A. Potter and J. Hoyt, "A molecular dynamics simulation study of the crystal–melt interfacial free energy and its anisotropy in the Cu–Ag–Au ternary system," *Journal of crystal growth,* vol. 327, no. 1, pp. 227-232, 2011.

103 J. Friedli, et al., "Dendritic growth morphologies in Al-Zn alloys—Part I: X-ray tomographic microscopy," *Metallurgical and Materials Transactions A,* vol. 44, no. 12, pp. 5522-5531, 2013.

104 J. Dantzig, et al., "Dendritic growth morphologies in Al-Zn alloys—Part II: phase-field computations," *Metallurgical and Materials Transactions A,* vol. 44, no. 12, pp. 5532-5543, 2013.

105 F. Gonzales and M. Rappaz, "Dendrite growth directions in aluminum-zinc alloys," *Metallurgical and Materials Transactions A,* vol. 37, no. 9, pp. 2797-2806, 2006.

106 M. Becker, et al., "Dendrite orientation transition in AlGe alloys," *Acta Materialia,* vol. 165, no. pp. 666-677, 2019.

107 J. Hoyt, et al., "Unusual temperature dependence of the solid-liquid interfacial free energy in the Cu-Zr system," *Computational materials science,* vol. 154, no. pp. 303-308, 2018.

108 C. Qi, et al., "Solid-liquid interfacial free energy and its anisotropy in the Cu-Ni binary system investigated by molecular dynamics simulations," *Journal of alloys and compounds,* vol. 708, no. pp. 1073-1080, 2017.

109 G. Kaptay, "On the solid/liquid interfacial energies of metals and alloys," *Journal of materials science,* vol. 53, no. 5, pp. 3767-3784, 2018.

110 B.G. Thomas, M.S. Jenkins, and R.B. Mahapatra, "Investigation of strand surface defects using mould instrumentation and modelling," *Ironmaking & steelmaking,* vol. 31, no. 6, pp. 485-494, 2004.

111 J. Sengupta, et al., "Micrograph evidence of meniscus solidification and sub-surface microstructure evolution in continuous-cast ultralow-carbon steels," *Acta materialia,* vol. 54, no. 4, pp. 1165-1173, 2006.

112 W. Kurz, in*:"About initial solidification in continuous casting of steel", la metallurgia italiana, 2008, Issue 7-8, pp. 56-64.*

113 H. Zhang and W. Wang, "Mold simulator study of the initial solidification of molten steel in continuous casting mold: Part II. Effects of mold oscillation and mold level fluctuation," *Metallurgical and Materials Transactions B,* vol. 47, no. 2, pp. 920-931, 2016.

114 V. Guyot, et al., "Control of surface quality of 0.08%< C< 0.12% steel slabs in continuous casting," *ISIJ international,* vol. 36, no. Suppl, pp. S227-S230, 1996.

115 A. Badri, et al., "A mold simulator for the continuous casting of steel: part I. The development of a simulator," *Metallurgical and Materials Transactions B,* vol. 36, no. 3, pp. 355-371, 2005.

116 S. N. Singh and K. E. Blazek, "Heat transfer and skin formation in a continuous-casting mold as a function of steel carbon content," *JOM,* vol. 26, no. 10, pp. 17-27, 1974.

117 T. Emi and H. Fredriksson, "High-speed continuous casting of peritectic carbon steels," *Mater.Sci. Eng. A,* vol. 413, no. pp. 2-9, 2005.

118 "J. Konishi, M. Militzer, I. V. Samarasekera, J. K. Brimacombe, Modeling the formation of longitudinal facial cracks during continuous casting of hypoperitectic steel," *Metall. Mater. Trans. B,* vol. 33, no. 3, pp. 413-423, 2002.

119 J. Sengupta, C. Ojeda, and B. Thomas, "Thermal-mechanical behaviour during initial solidification in continuous casting: steel grade effects," *International Journal of cast metals research,* vol. 22, no. 1-4, pp. 8-14, 2009.

120 T. W. Clyne, M. Wolf, and W. Kurz, "The effect of melt composition on solidification cracking of steel, with particular reference to continuous casting," *Metall. Trans. B,* vol. 13, no. 2, pp. 259-266, 1982.

121 G. Xia, et al., "A study about the influence of carbon content in the steel on the casting behavior," *steel Res. Int.*, vol. 82, no. 3, pp. 230-236, 2011.

122 L.-G. Zhu and R. Kumar, "Shrinkage of carbon steel by thermal contraction and phase transformation during solidification," *Ironmaking & steelmaking*, vol. 34, no. 1, pp. 71-75, 2007.

123 "K. Harste, K. Schwerdtfeger, Shrinkage of round iron-carbon ingots during solidification and subsequent cooling, 2003, Vol. 43(7), ISIJ Int., p. 1011-1020.," vol. no.,

124 "A. Grill, K. Sorimachi, J. K. Brimacombe, Heat flow, gap formation and break-outs in the continuous casting of steel slabs," *Metall. Trans. B*, vol. 7, no. 2, pp. 177-189, 1976.

125 "J. XU, S. He, X. Jiang, T. Wu, and Q. Wang, Analysis of crack susceptibility of regular carbon steel slabs using volume-based shrinkage index, 2013, ISIJ Int., 53(10), p. 1812-1817.," vol. no.,

126 A. Lagerstedt, et al., "Measurements and modeling of air gap formation in iron-base alloys," *Mater. Sci. Eng. A*, vol. 413, no. pp. 44-51, 2005.

127 A. Grill and J. Brimacombe, "Influence of C Content on Rate of Heat Extraction in the Mould of a Continuous-Casting Machine," *Ironmaking Steelmaking*, vol. 3, no. 2, pp. 76-79, 1976.

128 "K. Kim, H.N. Han, T. Yeo, Y. Lee, K. H. Oh, D. N. Lee, Analysis of surface and internal cracks in continuously cast beam blank," *Ironmak. Steelmak.*, vol. 24, no. 3, pp. 249-256, 1997.

129 C.H. Yu, et al., "Simulation of crack formation on solidifying steel shell in continuous casting mold," *ISIJ international*, vol. 36, no. Suppl, pp. S159-S162, 1996.

130 B. De Cooman, "Structure–properties relationship in TRIP steels containing carbide-free bainite," *Current Opinion in Solid State and Materials Science*, vol. 8, no. 3-4, pp. 285-303, 2004.

131 P. Jacques, "Transformation-induced plasticity for high strength formable steels," *Current Opinion in Solid State and Materials Science*, vol. 8, no. 3-4, pp. 259-265, 2004.

132 I. Tamura, H. Sekine, and T. Tanaka, *Thermomechanical processing of high-strength low-alloy steels*. 2013: Butterworth-Heinemann.

133 K.-H. Lee, et al., "Master curve characterization of the fracture toughness behavior in SA508 Gr. 4N low alloy steels," *Journal of Nuclear Materials*, vol. 403, no. 1-3, pp. 68-74, 2010.

134 H. Kerr and W. Kurz, "Solidification of peritectic alloys," *International Materials Reviews*, vol. 41, no. 4, pp. 129-164, 1996.

135 H.W. Kerr, J. Cisse, and G. Bolling, "On equilibrium and non-equilibrium peritectic transformations," *Acta Metallurgica,* vol. 22, no. 6, pp. 677-686, 1974.

136 G. Wen, et al., "Development of fluoride-free mold powders for peritectic steel slab casting," *ISIJ international,* vol. 47, no. 8, pp. 1117-1125, 2007.

137 M. Kawamoto, et al., "Improvement of the initial stage of solidification by using mild cooling mold powder," *ISIJ international,* vol. 37, no. 2, pp. 134-139, 1997.

138 X. Long, et al., "Properties of high basicity mold fluxes for peritectic steel slab casting," *J. Iron Steel Res. Int.,* vol. 19, no. 7, pp. 39-45, 2012.

139 J. Brooks and A. Thompson, "Microstructural development and solidification cracking susceptibility of austenitic stainless steel welds," *International Materials Reviews,* vol. 36, no. 1, pp. 16-44, 1991.

140 H. Yin. "Solidifying shell waviness during continuous casting of AHSS slabs," *in IOP Conference Series: Materials Science and Engineering. 2019*. IOP Publishing.

141 P. Presoly, R. Pierer, and C. Bernhard, "Identification of defect prone peritectic steel grades by analyzing high-temperature phase transformations," *Metallurgical and Materials Transactions A,* vol. 44, no. 12, pp. 5377-5388, 2013.

142 J. Chipman, "Thermodynamics and phase diagram of the Fe-C system," *Metallurgical and Materials Transactions B,* vol. 3, no. 1, pp. 55-64, 1972.

143 M. Tisza, "Physical metallurgy for engineers", in *ASM International, Materials Park, Ohio, 2003.*

144 P. Presoly, et al., "Continuous Casting of Hypo-peritectic Steels: Mould Thermal Monitoring and DSC-analysis," *BHM Berg-und Hüttenmännische Monatshefte,* vol. 159, no. 11, pp. 430-437, 2014.

145 E. Wielgosz and T. Kargul, "Differential scanning calorimetry study of peritectic steel grades," *Journal of Thermal Analysis and Calorimetry,* vol. 119, no. 3, pp. 1547-1553, 2015.

146 H. Chen, et al., "Manganese Influence on Equilibrium Partition Coefficient and Phase Transformation in Peritectic Steel", in *TMS Annual Meeting & Exhibition, Springer, Cham,2018, pp. 419-430.*

147 O. Martiník, et al., "Experimental and theoretical assessment of liquidus, peritectic transformation, and solidus temperatures of laboratory and commercial steel grades," *J. Phase Equilib. Diff.,* vol. 40, no. 1, pp. 93-103, 2019.

148 S. Abraham, et al., "Investigation of Peritectic Behavior of Steel Using a Thermal Analysis Technique," *Metallurgical and Materials Transactions A,* vol. 50, no. 5, pp. 2259-2271, 2019.

149 G. Xia, et al., "Investigation of mould thermal behaviour by means of mould instrumentation," *Ironmaking & steelmaking,* vol. 31, no. 5, pp. 364-370, 2004.

150 A. Howe, "Development of a computer model of dendritic microsegregation for use with multicomponent steels," *Applied Scientific Research,* vol. 44, no. 1-2, pp. 51-59, 1987.

151 M. Wolf, "Continuous Casting, Volume Nine: Initial Solidification and Strand Surface Quality of Peritectic Steels*",* in *Iron and Steel Society, Warrendale, PA , 1997, pp. 61-65.*

152 J. Xu, et al., "Effect of elements on peritectic reaction in molten steel based on thermodynamic analysis," *ISIJ international,* vol. 52, no. 10, pp. 1856-1861, 2012.

153 A. Kagawa and T. Okamoto, "Influence of alloying elements on temperature and composition for peritectic reaction in plain carbon steels," *Materials science and technology,* vol. 2, no. 10, pp. 997-1008, 1986.

154 R. Sarkar, et al., "Effects of Alloying Elements on the Ferrite Potential of Peritectic and Ultra-Low Carbon Steels," *ISIJ international*, vol. 55, no. 4, pp. 781-790, 2015.

155 P. Presoly, R. Pierer, and C. Bernhard, "Linking up of HT-LSCM and DSC measurements to characterize phase diagrams of steels*",* in *IOP Conference Series: Materials Science and Engineering, IOP Publishing, vol. 33, p. 012064.* 2012. p. 012064.

156 D.S. Petrovič, et al., "Differential scanning calorimetry study of the solidification sequence of austenitic stainless steel," *Journal of Thermal Analysis and Calorimetry,* vol. 105, no. 1, pp. 251-257, 2011.

157 B. Cantor, "Differential scanning calorimetry and the advanced solidification processing of metals and alloys," *Journal of Thermal Analysis and Calorimetry,* vol. 42, no. 4, pp. 647-665, 1994.

158 G. Klančnik, et al., "Influence of Mn on the solidification of Fe–Si–Al alloy for non-oriented electrical steel," *Journal of Thermal Analysis and Calorimetry,* vol. 116, no. 1, pp. 295-302, 2014.

159 W. Mingjia, et al., "Influence of rare earth elements on solidification behavior of a high speed steel for roll using differential scanning calorimetry," *J. Rare Earths,* vol. 29, no. 11, pp. 1089-1094, 2011.

160 Ş.H. Atapek, E. Erişir, and S. Gümüş, "Modeling and thermal analysis of solidification in a low alloy steel," *Journal of Thermal Analysis and Calorimetry,* vol. 114, no. 1, pp. 179-183, 2013.

161 K. Hechu, et al., "A novel approach for interpreting the solidification behaviour of peritectic steels by combining CSLM and DSC," *Materials Characterization,* vol. 133, no. pp. 25-32, 2017.

162 A. Howe, *Segregation and Phase Distribution During Solidification of Carbon, Alloy and Stainless Steels: 1 July 1986 to 30 June 1989; Final Report*. 1991: Office for Official Publications of the European Communities.

163 A. NORMSNTON, "Improving surface quality of continuously cast semis by an understanding of shell development and growth. Final report, Technical steel research series, Luxembourg,(2005), 349 p". ISBN 92-79-00066-1.

164 A.K. Sinha, "Physical metallurgy handbook", in *McGraw-Hill Professional Publishing, New york, pp. 594-600.* 2003.

165 K.E. Blazek, et al., "Calculation of the peritectic range for steel alloys," *Iron & steel technology,* vol. 5, no. 7, pp. 80-85, 2008.

166 "Thermo-Calc Software TCFE9 Steels/Fe-alloys database, Råsundavägen, Sweden. ".

167 Y. Liu, et al., "Effect of casting parameters on sticker breakout and its propagation behaviour during slab continuous casting," *Ironmak. Steelmak.*, vol. 41, no. 10, pp. 748-755, 2014.

168 S. McKay, et al., "Continuous casting mould powder evaluation," *Ironmak. Steelmak.,* vol. 29, no. 3, pp. 185-190, 2002.

169 S. Sridhar, et al., "Break temperatures of mould fluxes and their relevance to continuous casting," *Ironmak. Steelmak.*, vol. 27, no. 3, pp. 238-242, 2000.

170 J.-O. Andersson, et al., "Thermo-Calc & DICTRA, computational tools for materials science," *Calphad,* vol. 26, no. 2, pp. 273-312, 2002.

171 K. Matsuura, et al., "Rate of peritectic reaction in iron-carbon system measured by solid/liquid diffusion couple method," *ISIJ international,* vol. 35, no. 2, pp. 183-187, 1995.

172 A. Titchener and J. Spittle, "A solid–liquid diffusion couple study of peritectic reactions," *Metal Science,* vol. 8, no. 1, pp. 112-116, 1974.

173 S.P. Gupta, "Intermetallic compounds in diffusion couples of Ti with an Al–Si eutectic alloy," *Materials Characterization,* vol. 49, no. 4, pp. 321-330, 2002.

174 F. Bartels, et al., "Intermetallic phase formation in thin solid-liquid diffusion couples," *Journal of electronic Materials,* vol. 23, no. 8, pp. 787-790, 1994.

175 J.-H. Dai, et al., "Effect of Mn additions on diffusion behavior of Fe in molten magnesium alloys by solid-liquid diffusion couples," *Journal of alloys and compounds,* vol. 710, no. pp. 260-266, 2017.

176 C.R. Hutchinson, et al., "A novel experimental approach to identifying kinetic transitions in solid state phase transformations," *Scripta materialia,* vol. 50, no. 2, pp. 285-290, 2004.

177 M. Mirjalili, et al., "On the kinetics of TiAl3 intermetallic layer formation in the titanium and aluminum diffusion couple," *Intermetallics*, vol. 32, no. pp. 297-302, 2013.

178 G.S. Kino and T.R. Corle, "Confocal scanning optical microscopy and related imaging systems", in *Academic Press, San Diego, 1996.*

179 N. McDonald and S. Sridhar, "Observations of the advancing δ-ferrite/γ-austenite/liquid interface during the peritectic reaction," *Journal of materials science*, vol. 40, no. 9-10, pp. 2411-2416, 2005.

180 T. Liu, et al., "Investigations of the peritectic reaction and transformation in a hypo-peritectic steel: Using high-temperature confocal scanning laser microscopy and differential scanning calorimetry," *Materials Characterization*, vol. 156, no. pp. 109870, 2019.

181 H. Chikama, et al., "'In-situ' real time observation of planar to cellular and cellular to dendritic transition of crystals growing in Fe–C alloy melts," *Materials transactions, JIM*, vol. 37, no. 4, pp. 620-626, 1996.

182 "In-situ Observation at Ultra High Temperature Confocal Scanning Laser Microscope (VL2000DX-SVF17S) (2018), https://www.lasertec.co.jp/en/products/microscope/laser/vl2000dx.html".

183 W. Mu, et al., "High-temperature confocal laser scanning microscopy studies of ferrite formation in inclusion-engineered steels: a review," *JOM*, vol. 70, no. 10, pp. 2283-2295, 2018.

184 R.H. Mathiesen, et al., "Time-resolved x-ray imaging of aluminum alloy solidification processes," *Metallurgical and Materials Transactions B*, vol. 33, no. 4, pp. 613-623, 2002.

185 H. Yasuda, et al., "Development of X-ray imaging for observing solidification of carbon steels," *ISIJ international*, vol. 51, no. 3, pp. 402-408, 2011.

186 M. Rappaz, et al., "Connectivity of phases and growth mechanisms in peritectic alloys solidified at low speed: an X-ray tomography study of Cu-Sn," *Metallurgical and Materials Transactions A*, vol. 41, no. 3, pp. 563-567, 2010.

187 S.H. Davis, "Theory of solidification", in *Cambridge University Press, New York, 2001, p. 45.*

188 A. Karma, et al., "Model of banding in diffusive and convective regimes during directional solidification of peritectic systems," *Metallurgical and Materials Transactions A*, vol. 29, no. 5, pp. 1457-1470, 1998.

189 T.A. Lograsso, B. Fuh, and R. Trivedi, "Phase selection during directional solidification of peritectic alloys," *Metallurgical and Materials Transactions A*, vol. 36, no. 5, pp. 1287-1300, 2005.

190 D. Huntley and S.H. Davis, "Thermal effects in rapid directional solidification: linear theory," *Acta metallurgica et materialia,* vol. 41, no. 7, pp. 2025-2043, 1993.

191 G. Merchant and S.H. Davis, "Morphological instability in rapid directional solidification," *Acta metallurgica et materialia,* vol. 38, no. 12, pp. 2683-2693, 1990.

192 H.Z. Fu and L. Liu. "Progress of directional solidification in processing of advanced materials," *in Materials Science Forum. 2005*. Trans Tech Publ.

193 T.S. Lo, A. Karma, and M. Plapp, "Phase-field modeling of microstructural pattern formation during directional solidification of peritectic alloys without morphological instability," *Physical Review E,* vol. 63, no. 3, pp. 031504, 2001.

194 J. Valloton, J.-D. Wagnière, and M. Rappaz, "Competition of the primary and peritectic phases in hypoperitectic Cu–Sn alloys solidified at low speed in a diffusive regime," *Acta materialia,* vol. 60, no. 9, pp. 3840-3848, 2012.

195 H. Fu and F. Xie, "The solidification characteristics of near rapid and supercooling directional solidification," *Sci. Technol. Adv. Mater.,* vol. 2, no. 1, pp. 193, 2001.

196 H. Terasaki, et al., "Time-resolved in-situ analysis of phase evolution for the directional solidification of carbon steel weld metal," *Metallurgical and Materials Transactions A,* vol. 37, no. 4, pp. 1261-1266, 2006.

197 H.N. Thi, et al., "Preliminary in situ and real-time study of directional solidification of metallic alloys by x-ray imaging techniques," *Journal of Physics D: Applied Physics,* vol. 36, no. 10A, pp. A83, 2003.

198 N. McDonald and S. Sridhar, "Peritectic reaction and solidification in iron-nickel alloys," *Metallurgical and Materials Transactions A,* vol. 34, no. 9, pp. 1931-1940, 2003.

199 M. Hillert, "Solidification and casting of metals*",* in *The Metals Society, London, 1979, vol. 81, p. 413.*

200 S. Pan, M. Zhu, and M. Rettenmayr, "A phase-field study on the peritectic phase transition in Fe-C alloys," *Acta materialia,* vol. 132, no. pp. 565-575, 2017.

201 D. Phelan, M. Reid, and R. Dippenaar, "Experimental and modelling studies into high temperature phase transformations," *Computational materials science,* vol. 34, no. 3, pp. 282-289, 2005.

202 B. Chalmers, "Principles of solidification", in *Applied solid state physics*. 1970, Springer. p. 161-170.

203 A. Choudhury, et al., "Growth morphologies in peritectic solidification of Fe–C: A phase-field study," *Acta materialia,* vol. 58, no. 10, pp. 3815-3823, 2010.

204 G. Boussinot, E. Brener, and D. Temkin, "Kinetics of isothermal phase transformations above and below the peritectic temperature: Phase-field simulations," *Acta materialia,* vol. 58, no. 5, pp. 1750-1760, 2010.

205 E.A. Brener and D. Temkin, "Melting of alloys along the inter-phase boundaries in eutectic and peritectic systems," *Acta materialia,* vol. 55, no. 8, pp. 2785-2789, 2007.

206 G. Boussinot, et al., "Isothermal solidification in peritectic systems," *Acta materialia,* vol. 75, no. pp. 212-218, 2014.

207 H. Nassar and H. Fredriksson, "On peritectic reactions and transformations in low-alloy steels," *Metallurgical and Materials Transactions A,* vol. 41, no. 11, pp. 2776-2783, 2010.

208 H. Lopez, "Analysis of solute segregation effects on the peritectic transformation," *Acta metallurgica et materialia,* vol. 39, no. 7, pp. 1543-1548, 1991.

209 H. Ha and J. Hunt, "A numerical and experimental study of the rate of transformation in three directionally grown peritectic systems," *Metallurgical and Materials Transactions A,* vol. 31, no. 1, pp. 29-34, 2000.

210 A. Das, I. Manna, and S. Pabi, "An analytical model for peritectic transformation with experimental verification," *Scripta materialia,* vol. 36, no. 8, pp. 867-874, 1997.

211 N. Liu, et al., "Peritectic solidification of undercooled Fe–Co alloys," *Journal of alloys and compounds,* vol. 465, no. 1-2, pp. 391-395, 2008.

212 S. Pan and M. Zhu, "Peritectic transformation with non-linear solute distribution in all three phases: Analytical solution, phase-field modeling and experiment comparison," *Acta materialia,* vol. 146, no. pp. 63-75, 2018.

213 K. Matsuura, et al., "Effects of cooling rate on growth behavior of austenite phase during peritectic reaction in iron-carbon binary alloy," *ISIJ international,* vol. 35, no. 12, pp. 1483-1488, 1995.

214 K. Matsuura and M. Kudoh, "Finite difference simulation of peritectic transformation in iron-carbon alloy," *Materials transactions, JIM,* vol. 39, no. 1, pp. 203-210, 1998.

215 N. Moelans, B. Blanpain, and P. Wollants, "An introduction to phase-field modeling of microstructure evolution," *Calphad,* vol. 32, no. 2, pp. 268-294, 2008.

216 N. Provatas and K. Elder, "Phase-field methods in materials science and engineering", in *WILEY-VCH Verlag GmbH, Weinheim, Germany, 2011.*

217 B. Nestler, H. Garcke, and B. Stinner, "Multicomponent alloy solidification: phase-field modeling and simulations," *Physical Review E,* vol. 71, no. 4, pp. 041609, 2005.

218 A. Karma and W.-J. Rappel, "Quantitative phase-field modeling of dendritic growth in two and three dimensions," *Physical Review E,* vol. 57, no. 4, pp. 4323, 1998.

219 M. Mamivand, M.A. Zaeem, and H. El Kadiri, "A review on phase field modeling of martensitic phase transformation," *Computational materials science,* vol. 77, no. pp. 304-311, 2013.

220 M. Ohno and K. Matsuura, "Motion and morphology of triple junction in peritectic reaction analyzed by quantitative phase-field model," *ISIJ international,* vol. 50, no. 12, pp. 1879-1885, 2010.

221 C.L.M. Alves, et al., "Quantitative isothermal phase-field simulations of peritectic phase transformation in FeMn system," *J. Mater. Res. Technol.,* vol. 5, no. 1, pp. 84-91, 2016.

222 M. Yoshiya, et al., "Concurrent γ-Phase Nucleation as a Possible Mechanism of δ-γ Massive-like Phase Transformation in Carbon Steel: Numerical Analysis Based on Effective Interface Energy", in *Materials transactions, 2015, Vol. 56, No. 9, pp. 1467-1474.*

223 M. Hillert, "Thermodynamics of the massive transformation," *Metallurgical Transactions A,* vol. 15, no. 3, pp. 411-419, 1984.

224 M. Plichta, W. Clark, and H. Aaronson, "The nucleation kinetics, crystallography, and mechanism of the massive transformation," *Metallurgical Transactions A,* vol. 15, no. 3, pp. 427-435, 1984.

225 E. Pereloma and D.V. Edmonds, "Phase transformations in steels: fundamentals and diffusion-controlled transformations", in *Woodhead Publishing Limited, Cambridge, Uk, 2012.* .

226 E. Wilson, "γ→ α transformation in Fe, Fe–Ni, and Fe–Cr alloys," *Metal Science,* vol. 18, no. 10, pp. 471-484, 1984.

227 T. Massalski, "Massive transformations revisited," *Metallurgical and Materials Transactions A,* vol. 33, no. 8, pp. 2277-2283, 2002.

228 M. Hillert, "Nature of massive transformation," *Metallurgical and Materials Transactions A,* vol. 35, no. 1, pp. 351-352, 2004.

229 H. Fredriksson and J. Stjerndahl, "Solidification of iron-base alloys," *Metal Science,* vol. 16, no. 12, pp. 575-586, 1982.

230 M. Yoshiya, et al. "Impacts of Interface Energies and Transformation Strain from BCC to FCC on Massive-like δ-γ Transformation in Steel," *in IOP Conference Series: Materials Science and Engineering. 2015*. IOP Publishing.

231 S.C. Moon, R. Dippenaar, and S.-Y. Kim, "The peritectic phase transition of steel during the initial stages of solidification in the mold", in *AISTech Conference, Cleveland, Ohio, 2015.*

232 M.M. WOLF, "A review of published work on the solidification control of steel in continuous casting moulds by heat flux measurement," *Transactions of the Iron and Steel Institute of Japan,* vol. 20, no. 10, pp. 718-724, 1980.

233 W.H. Emling, "Breakout prevention," *Iron and Steelmaker.,* vol. no. 5, pp. 50, 1994.

234 B.G. Thomas, in *Brimacombe Continuous Casting Course, Vancouver, Canada, 2018*

235 J. Guo, et al., "A novel approach for evaluating the contraction of hypo-peritectic steels during initial solidification by surface roughness," *Materials,* vol. 11, no. 4, pp. 571, 2018.

236 H. Cui, et al., "Formation of Surface Depression during Continuous Casting of High-Al TRIP Steel," *Metals,* vol. 9, no. 2, pp. 204, 2019.

237 D. Pu, et al., "Study of the Effect of Carbon on the Contraction of Hypo-Peritectic Steels during Initial Solidification by Surface Roughness," *Metals,* vol. 8, no. 12, pp. 982, 2018.

238 "S. Dong, E. Niyama, K. Anzai, Free deformation of initial solid shell of Fe-C alloys", in *ISIJ Int., 1995, 35 (6), pp. 730-36.*

239 K. Harste and K. Schwerdtfeger, "Shrinkage of round iron-carbon ingots during solidification and subsequent cooling," *ISIJ international,* vol. 43, no. 7, pp. 1011-1020, 2003.

240 A. Jablonka, K. Harste, and K. Schwerdtfeger, "Thermomechanical properties of iron and iron-carbon alloys: density and thermal contraction," *Steel research,* vol. 62, no. 1, pp. 24-33, 1991.

241 C. Bernhard, H. Hiebler, and M. Wolf, "How fast can we cast?," *Ironmaking & steelmaking,* vol. 27, no. 6, pp. 450-454, 2000.

242 C. Bernhard and G. Xia, "Influence of alloying elements on the thermal contraction of peritectic steels during initial solidification," *Ironmak. Steelmak.,* vol. 33, no. 1, pp. 52-56, 2006.

243 R.V.K. L.-G. Zhu, "Shrinkage of carbon steel by thermal contraction and phase transformation during solidification," *Ironmaking & steelmaking,* vol. 34, no. 1, pp. 71-75, 2007.

244 M. Wolf, in *personal communication, Lintz, Austria,1999.* .

245 "M. L. Zappulla, L. C. Hibbeler, B. G. Thomas, Effect of Grade on Thermal–Mechanical Behavior of Steel During Initial Solidification," *Metall. Mater. Trans. A,* vol. 48, no. 8, pp. 3777-3793, 2017.

246 P. Wray, "Mechanical, physical and thermal data for modeling the solidification processing of steels," *Modeling of Casting and Welding Processes,* vol. no. pp. 245-257, 1980.

247 B. Thomas and J. Parkman, "Simulation of thermal distortion of a steel droplet solidifying on a copper chill", in *The Minerals, Metals, and Materials Society, Warrendale, PA,pp 509-520, 1998.*

248 B. Thomas, J. Brimacombe, and I. Samarasekera, "The formation of panel cracks in steel ingots: a state-of-the-art review," *ISS Transactions,* vol. 7, no. 10, pp. 7-20, 1986.

249 B. Mintz and D. Crowther, "Hot ductility of steels and its relationship to the problem of transverse cracking in continuous casting," *International Materials Reviews,* vol. 55, no. 3, pp. 168-196, 2010.

250 B. Mintz, S. Yue, and J. Jonas, "Hot ductility of steels and its relationship to the problem of transverse cracking during continuous casting," *International Materials Reviews,* vol. 36, no. 1, pp. 187-220, 1991.

251 A. Yamanaka, K. Nakajima, and K. Okamura, "Critical strain for internal crack formation in continuous casting," *Ironmaking and steelmaking,* vol. 22, no. 6, pp. 508-512, 1995.

252 "Y.M. Won, K.H. Kim, T.J. Yeo, and K.H. Oh, Effect of cooling rate on ZST, LIT and ZDT of carbon steels near melting point, ISIJ int., 1998, 38(10), p.1093-1099.," vol. no.,

253 N. Pradhan, et al., "Control of transverse cracking in special quality slabs," *Ironmaking & steelmaking,* vol. 28, no. 4, pp. 305-311, 2001.

254 B. Mintz, "The influence of composition on the hot ductility of steels and to the problem of transverse cracking," *ISIJ international,* vol. 39, no. 9, pp. 833-855, 1999.

255 B. Mintz and J. Arrowsmith, "Hot-ductility behaviour of C–Mn–Nb–Al steels and its relationship to crack propagation during the straightening of continuously cast strand," *Metals technology,* vol. 6, no. 1, pp. 24-32, 1979.

256 H.G. Suzuki, S. Nishimura, and Y. NAKAMURA, "Improvement of hot ductility of continuously cast carbon steels," *Transactions of the Iron and Steel Institute of Japan,* vol. 24, no. 1, pp. 54-59, 1984.

257 C. Ouchi and K. Matsumoto, "Hot ductility in Nb-bearing high-strength low-alloy steels," *Transactions of the Iron and Steel Institute of Japan,* vol. 22, no. 3, pp. 181-189, 1982.

258 S.K. Kim, J.S. Kim, and N.J. Kim, "Effect of boron on the hot ductility of Nb-containing steel," *Metallurgical and Materials Transactions,* vol. 33, no. 3, pp. 701, 2002.

259 Y. MAEHARA, et al., "Effect of carbon on hot ductility of as-cast low alloy steels," *Tetsu-to-Hagané,* vol. 71, no. 11, pp. 1534-1541, 1985.

260 K.-h. Kim, et al., "Effect of carbon and sulfur in continuously cast strand on longitudinal surface cracks," *ISIJ international,* vol. 36, no. 3, pp. 284-289, 1996.

261 J. Miyazaki, K. Narita, and T. Nozaki, "On the internal cracks caused by the bending test of small ingot," *Trans ISIJ*, vol. 21, no. pp. B210, 1981.

262 T. MATSUMIYA, et al., "An evaluation of critical strain for internal crack formation in continuously cast slabs," *Transactions of the Iron and Steel Institute of Japan*, vol. 26, no. 6, pp. 540-546, 1986.

263 K. Wünnenberg and R. Flender, "Investigation of internal-crack formation in continuous casting using a hot model," *Ironmaking & steelmaking*, vol. 12, no. 1, pp. 22-29, 1985.

264 T. KOHNO, et al., "The Metallographical Characteristics and the Formation Mechanism of Longitudinal Surface Cracks in CC Slabs," *Tetsu-to-Hagané*, vol. 68, no. 13, pp. 1764-1772, 1982.

265 M. Suzuki, et al., "In-situ measurement of fracture strength of solidifying steel shells to predict upper limit of casting speed in continuous caster with oscillating mold," *ISIJ international*, vol. 37, no. 4, pp. 375-382, 1997.

266 H. Hiebler, et al. "Inner crack formation in continuous casting: Stress or strain criterion?," *in Steelmaking Conference. 1994*.

267 K. Wünnenberg and R. Flender, *Investigation of internal-crack formation in continuous-casting, using a hot model*. 1985: Mannesmann-Forschungsinst.

268 S. NAGATA, et al., "Estimation of critical strain for internal crack formation in continuously cast slabs," *Tetsu-to-Hagané*, vol. 76, no. 2, pp. 214-221, 1990.

269 J. Kristiansson, "Thermomechanical behavior of the solidifying shell within continuous-casting billet molds-a numerical approach," *Journal of Thermal Stresses*, vol. 7, no. 3-4, pp. 209-226, 1984.

270 K. Sorimachi and J. Brimacombe, "Improvements in mathematical modelling of stresses in continuous casting of steel," *Ironmaking Steelmaking*, vol. 4, no. 4, pp. 240-245, 1977.

271 M. El-Bealy and H. Fredriksson, "Modeling of the peritectic reaction and macro-segregation in casting of low carbon steel," *Metallurgical and Materials Transactions B*, vol. 27, no. 6, pp. 999-1014, 1996.

272 C. Li and B. G. Thomas, "Thermomechanical finite-element model of shell behavior in continuous casting of steel," *Metall. Mater. Trans. B*, vol. 35, no. 6, pp. 1151-1172, 2004.

273 J.-O. Kristiansson, "Thermal stresses in the early stage of solidification of steel," *Journal of Thermal Stresses*, vol. 5, no. 3-4, pp. 315-330, 1982.

274 B. Thomas, A. Moitra, and H. Zhu, "Coupled thermo-mechanical model of solidifying steel shell applied to depression defects in continuous-cast slabs", in *Modeling of Casting, Welding, and Advanced Solidification Processes VII, London, England, 241-248, Sept. 10-15, 1995*.

275 B.G. Thomas, A. Moitra, and R. McDavid, "Simulation of longitudinal off-corner depressions in continuously cast steel slabs," *Iron and Steelmaker(USA),* vol. 23, no. 4, pp. 57-70, 1996.

276 B. Thomas, I. Samarasekera, and J. Brimacombe, "Mathematical model of the thermal processing of steel ingots: Part II. Stress model," *Metallurgical Transactions B,* vol. 18, no. 1, pp. 131, 1987.

277 M. Rowan, et al., "Measuring mechanical behavior of steel during solidification: modeling the SSCC test," *Metallurgical and Materials Transactions B,* vol. 42, no. 4, pp. 837-851, 2011.

278 J. Kelly, et al., "Initial development of thermal and stress fields in continuously cast steel billets," *Metallurgical Transactions A,* vol. 19, no. 10, pp. 2589-2602, 1988.

279 B. Korojy, H. Nassar, and H. Fredriksson, "Hot crack formation during peritectic reaction in steels," *Ironmaking & steelmaking,* vol. 37, no. 1, pp. 63-72, 2010.

280 C. Bernhard, et al., "Experimental characterization of crack sensitivity under continuous casting conditions*",* in *Continuous-Casting Innovation Session - Paper No. 06.03, Linz, Austria, June 2004.* . p. 14-15.

281 Y.M. Won, et al., "Analysis of solidification cracking using the specific crack susceptibility," *ISIJ international,* vol. 40, no. 2, pp. 129-136, 2000.

282 M.H. Trejo, et al., "Effect of solidification path and contraction on the cracking susceptibility of carbon peritectic steels," *metals and materials international,* vol. 16, no. 5, pp. 731-737, 2010.

283 W. Irving, A. Perkins, and R. Gray, "EFFECT OF STEEL CHEMISTRY AND OPERATING PARAMETERS ON SURFACE-DEFECTS IN CONTINUOUSLY CAST SLABS," *Ironmaking & steelmaking,* vol. 11, no. 3, pp. 146-151, 1984.

284 E.A. López, et al., "Effect of C and Mn variations upon the solidification mode and surface cracking susceptibility of peritectic steels," *ISIJ international,* vol. 49, no. 6, pp. 851-858, 2009.

285 H. Mizukami, A. Yamanaka, and T. Watanabe, "Prediction of density of carbon steels," *ISIJ international,* vol. 42, no. 4, pp. 375-384, 2002.

286 D. Crowther and B. Mintz, "Influence of grain size on hot ductility of plain C–Mn steels," *Materials science and technology,* vol. 2, no. 9, pp. 951-955, 1986.

287 Y. Kobayashi, et al., "Evolution of Columnar γ Grain in Low Carbon Steel and Its Refinement by Additional Elements in Thin Slab Casting Simulator," *ISIJ international,* vol. 48, no. 3, pp. 344-349, 2008.

288 K. Xu and B.G. Thomas. "Prediction of Grain Size, Precipitation and Crack Susceptibility in Continuous Casting," *in AISTech 2009 Steelmaking Conference Proc.,(St. Louis, MO. 2009*. Citeseer.

289 S. Tsuchiya, et al., "Formation mechanism of coarse columnar γ grains in as-cast hyperperitectic carbon steels," *Acta materialia,* vol. 59, no. 9, pp. 3334-3342, 2011.

290 R. Dippenaar, et al., "Austenite Grain Growth and the Surface Quality of Continuously Cast Steel," *Metallurgical and Materials Transactions B,* vol. 45, no. 2, pp. 409-418, 2014.

291 L. Schmidt and A. Josefsson, "On the formation and avoidance of transverse cracks in continuously cast slabs from curved mould machines," *Iron and Steel Society/AIME, Continuous Casting,* vol. 8, no. pp. 49-55, 1997.

292 G. Alvarez de Toledo, A. Arteaga, and J. Laraudogoitia. "Continuous casting of microalloyed steels. Influence of composition and operational parameters in billet surface cracking," *in Materials Science Forum. 2005*. Trans Tech Publ.

293 R.J. Dippenaar, S.-C. Moon, and E.S. Szekeres, "Strand surface cracks-the role of abnormally large prior Austenite Grains," vol. no., 2006.

294 K. YASUMOTO, et al., "Effects of alloying elements and cooling rate on austenite grain growth in solidification and the subsequent cooling processes of low alloy steels," *Tetsu-to-Hagané,* vol. 73, no. 14, pp. 1738-1745, 1987.

295 C. Bernhard, J. Reiter, and H. Presslinger, "A model for predicting the austenite grain size at the surface of continuously-cast slabs," *Metallurgical and Materials Transactions B,* vol. 39, no. 6, pp. 885-895, 2008.

296 N. YOSHIDA, Y. KOBAYASHI, and K. NAGAI, "Prediction of as-cast austenite grain size for near-net-shape CC," *Tetsu-to-Hagané,* vol. 90, no. 4, pp. 198-205, 2004.

297 N.S. POttore, C.I. Garcia, and A.J. DeArdo, "Interrupted and Isothermal Solidification Studies of Low and Medium Carbon Steels," *Metallurgical Transactions A,* vol. 22, no. 8, pp. 1871-1880, 1991.

298 "Y. Maehara, K. Yasumoto, H. Tomono, T. Nagamichi, Y. Ohmori, Surface cracking mechanism of continuously cast low carbon low alloy steel slabs," *Mater. Sci. Tech. ,* vol. 6, no. 9, pp. 793-806, 1990.

299 N. Yoshida, O. Umezawa, and K. Nagai, "Analysis on refinement of columnar γ grain by phosphorus in continuously cast 0.1 mass% carbon steel," *ISIJ international,* vol. 44, no. 3, pp. 547-555, 2004.

300 H.S. Kim, Y. Kobayashi, and K. Nagai, "Simulation of the influence of phosphorus on the prior austenite grain size of high-impurity steels," *Acta materialia,* vol. 54, no. 9, pp. 2441-2449, 2006.

301 J. Reiter, C. Bernhard, and H. Presslinger, "Determination and Prediction of austenite grain size in relation to product quality of the continuous casting process," *MATERIALS SCIENCE AND TECHNOLOGY-ASSOCIATION FOR IRON AND STEEL TECHNOLOGY-,* vol. 5, no. pp. 805, 2006.

302 J. Reiter, C. Bernhard, and H. Presslinger, "Austenite grain size in the continuous casting process: Metallographic methods and evaluation," *Materials Characterization,* vol. 59, no. 6, pp. 737-746, 2008.

303 Y. Ohba, S.-i. Kitade, and I. Takasu, "Austenite grain refining of as-cast bloom surface by reduction of oscillation mark depth," *ISIJ international,* vol. 48, no. 3, pp. 350-354, 2008.

304 J. Konishi, et al., "Modeling the formation of longitudinal facial cracks during continuous casting of hypoperitectic steel," *Metall. Mater. Trans. B,* vol. 33, no. 3, pp. 413-423, 2002.

305 H. Zhao, et al. "Experimental Studies on Flow Field and Particle Mixing Rate in a Sudden Expansion Combustor," *in 3rd National Conf. on Fluid Mech. 1985*. Changsha, China.

306 S.H. K. H. Kim, T. J. Yeo, K. H. Oh, D. N. Lee, " Effect of carbon and sulfur in continuously cast strand on longitudinal surface cracks," *ISIJ Int.,* vol. 36, no. 3, pp. 284-289, 1996.

307 G. Azizi, B. G. Thomas, and M. Asle Zaeem, "Review of Peritectic Solidification Mechanisms and Effects in Steel Casting," *Metall. Materi. Trans. B,* vol. 51, no. 5, pp. 1875-1903, 2020.

308 Y. M. Won, et al., " A new criterion for internal crack formation in continuously cast steels," *Metall. Mater. Trans. B,* vol. 31, no. 4, pp. 779-794, 2000.

309 G. Xia, et al., " A study about the influence of carbon content in the steel on the casting behavior," *steel Res. Int. ,* vol. 82, no. 3, pp. 230-236, 2011.

310 M. Suzuki, et al., "Origin of heat transfer anomaly and solidifying shell deformation of peritectic steels in continuous casting," *ISIJ Int.,* vol. 36, no. Suppl, pp. S171-S174, 1996.

311 C. Bernhard and G. Xia, "Influence of alloying elements on the thermal contraction of peritectic steels during initial solidification," *Ironmak. Steelmak.,* vol. 33, no. 1, pp. 52-56, 2006.

312 C. Bernhard, J. Reiter, and H. Presslinger, "A model for predicting the austenite grain size at the surface of continuously-cast slabs," *Metall. Mater. Trans. B,* vol. 39, no. 6, pp. 885-895, 2008.

313 A. Badri, et al., "A mold simulator for the continuous casting of steel: part I. The development of a simulator," *Metall. Mater. Trans. B,* vol. 36, no. 3, pp. 355-371, 2005.

314 L. G. Zhu and R.V. Kumar, "Shrinkage of carbon steel by thermal contraction and phase transformation during solidification," *Ironmak. Steelmak.,* vol. 34, no. 1, pp. 71-75, 2007.

315 P. E. Ramirez-Lopez, P. D. Lee, and K. C. Mills, "Explicit modelling of slag infiltration and shell formation during mould oscillation in continuous casting," *ISIJ Int.*, vol. 50, no. 3, pp. 425-434, 2010.

316 C. Perrot, et al., "Several slag rims and lubrication behaviours in slab casting," *Metall. Res. Tech.*, vol. 102, no. 12, pp. 887-896, 2005.

317 B. G. Thomas and F. M. Najjar, "Finite element modelling of turbulent fluid flow and heat transfer in continuous casting," *App. Math. model.*, vol. 15, no. 5, pp. 226-243, 1991.

318 J. Sengupta, C. Ojeda, and B. G. Thomas, "Thermal-mechanical behaviour during initial solidification in continuous casting: steel grade effects," *Int. J. Cast Met. Res.*, vol. 22, no. 1-4, pp. 8-14, 2009.

319 S. Harada, et al., "A formation mechanism of transverse cracks on CC slab surface," *ISIJ Int.*, vol. 30, no. 4, pp. 310-316, 1990.

320 K. Mukai and M. Zeze, "Motion of fine particles under interfacial tension gradient in relation to continuous casting process," *steel Res. Int.*, vol. 74, no. 3, pp. 131-138, 2003.

321 D. Balogun, et al., "Shell Measurements and Mold Thermal Mapping Approach to Characterize Steel Shell Formation in Peritectic Grade Steels," *steel Res. Int.*, vol. 93, no. 1, pp. 2100455, 2022.

322 S. Dong, et al., "Free deformation of the initial solid layer of some non-ferrous alloys," *Tetsu-to-Hagané*, vol. 79, no. 9, pp. 1060-1066, 1993.

323 S. Dong, E. Niyama, and K Anzai, "Free deformation of initial solid shell of Fe-C alloys," *ISIJ Int.*, vol. 35, no. 6, pp. 730-736, 1995.

324 S. Dong, "Thesis for Doctor Degree, Tohoku University". 1995.

325 B. G. Thomas and H. Zhu. "Thermal Distortion of solidifying shell near meniscus in continuous casting of steel," *in Proceedings of the International Symposia on Advanced Materials and Technology for the 21st Century, JIM/TMS. 1995*. Citeseer.

326 B. G. Thomas and J. T. Parkman, "Simulation of thermal distortion of a steel droplet solidifying on a copper chill," *In TMS Annual Meeting, Warrendale, PA.*, vol. no. pp. 509-520, 1998.

327 M. Vynnycky, "On the onset of air-gap formation in vertical continuous casting with superheat," *Int. J. Mech. Sci.*, vol. 73, no. pp. 69-76, 2013.

328 B. J. Florio, et al., "Mould-taper asymptotics and air gap formation in continuous casting," *Appl. Math. Comput.*, vol. 268, no. pp. 1122-1139, 2015.

329 Z. Niu, Z. Cai, and M. Zhu, "Dynamic distributions of mold flux and air gap in slab continuous casting mold," *ISIJ Int.*, vol. 59, no. 2, pp. 283-292, 2019.

330 T. M. Wang, et al., "Continuous casting mould for square steel billet optimised by solidification shrinkage simulation," *Ironmak. Steelmak.*, vol. 37, no. 5, pp. 341-346, 2010.

331 B. J. Florio, et al., "On the interactive effects of mould taper and superheat on air gaps in continuous casting," *Acta Mech.*, vol. 228, no. 1, pp. 233-254, 2017.

332 Z. Z. Cai and M. Y. Zhu, "Simulation of air gap formation in slab continuous casting mould," *Ironmak. Steelmak.*, vol. 41, no. 6, pp. 435-446, 2014.

333 Z. Cai and M. Zhu, "Simulation of Heat Transfer in Slab Continuous Casting Mold and New Formation Mechanism of Shell Hot Spots", in *CFD Modeling and Simulation in Materials Processing*. 2016, Springer. p. 43-49.

334 J. C. Alvarez Hostos, E. S. Puchi Cabrera, and A. D. Bencomo, "Stress Analysis of a Continuous Casting Process, on the Basis of the Element-Free Galerkin Formulation," *steel Res. Int.*, vol. 88, no. 2, pp. 1600019, 2017.

335 M. L. Zappulla, L. C. Hibbeler, and B. G. Thomas, "Effect of Grade on Thermal–Mechanical Behavior of Steel During Initial Solidification," *Metall. Mater. Trans. A*, vol. 48, no. 8, pp. 3777-3793, 2017.

336 J. K. Park, B. G. Thomas, and I. V. Samarasekera, "Analysis of thermomechanical behaviour in billet casting with different mould corner radii," *Ironmak. Steelmak.*, vol. 29, no. 5, pp. 359-375, 2002.

337 B. G. Thomas, A. Moitra, and R. McDavid, "Simulation of longitudinal off-corner depressions in continuously cast steel slabs," *Iron Steelmak.*, vol. 23, no. 4, pp. 57-70, 1996.

338 Z. Niu, Z. Cai, and M. Zhu, "Formation Mechanism of a Wide-Face Longitudinal Off-Corner Depression During Thick Slab Continuous Casting," *Metall. Mater. Trans. B*, vol. 52, no. 4, pp. 2737-2752, 2021.

339 J. M. Risso, A. E. Huespe, and A. Cardona, "Thermal stress evaluation in the steel continuous casting process," *Int. J. Numer. Methods Eng.*, vol. 65, no. 9, pp. 1355-1377, 2006.

340 J. O. Kristiansson, "Thermal stresses in the early stage of solidification of steel," *J. Therm. Stresses*, vol. 5, no. 3-4, pp. 315-330, 1982.

341 X. J. Zuo, et al., "Formation of Initial Defects at Meniscus in Oscillating Mold," *steel Res. Int.*, vol. 87, no. 4, pp. 413-423, 2016.

342 Y. Hebi, et al., "3D stress model with friction in and of mould for round billet continuous casting," *ISIJ Int.*, vol. 46, no. 4, pp. 546-552, 2006.

343 Z.Z. Cai and M. Y. Zhu, "Thermo-mechanical behavior of peritectic steel solidifying in slab continuous casting mold and a new mold taper design," *ISIJ Int.*, vol. 53, no. 10, pp. 1818-1827, 2013.

344 B. G. Thomas and C. Ojeda, "Ideal taper prediction for slab casting", in *In ISSTech Steelmaking Conference, Indianapolis, IN, USA*. 2003. p. 295-308.

345 K. Saito and M. Tate, "Solidification and strand guidance of slabs at high casting speeds", in *In Open Hearth Furnace Proceedings, Cleveland, OH*. 1973. p. 238-268.

346 P. F. Kozlowski, et al., " Simple constitutive equations for steel at high temperature," *Metall. Mater. Trans. A*, vol. 23, no. 3, pp. 903, 1992.

347 A. Jablonka, K. Harste, and K. Schwerdtfeger, "Thermomechanical properties of iron and iron-carbon alloys: density and thermal contraction," *Steel Res.*, vol. 62, no. 1, pp. 24-33, 1991.

348 I. Jimbo and A. W. Cramb, "The density of liquid iron-carbon alloys," *Metall. Trans. B*, vol. 24, no. 1, pp. 5-10, 1993.

349 I. Sawada, H. Tanaka, and I. Takigawa, "Numerical Study of Fluid Flow in the Continuous Casting Mold", in *In The Sixth International Iron and Steel Congress, Nagoya, Japan*. 1990. p. 334-347.

350 S.K. Saxena, et al., "Mechanism of Clogging of Tundish Nozzle during Continuous Casting of Aluminium-killed Steel," *Scand. J. Metall.*, vol. 7, no. pp. 126-133, 1978.

351 J. H. Weiner and B. A. Boley, "Elasto-plastic thermal stresses in a solidifying body," *J. Mech. Phys. Solids*, vol. 11, no. 3, pp. 145-154, 1963.

352 P. J. Wray, "Tensile failure behavior of plain carbon steels at elevated temperatures," *Metall. Trans. A*, vol. 15, no. 11, pp. 2059-2073, 1984.

353 R. Trivedi, "Effects of anisotropy properties on interface pattern formation," vol. no., 1990.

354 J. Rahman, "Atomistic Simulations for computing solid liquid interface properties of the Al-Mg system". 2009.

355 S. Plimpton, "Fast parallel algorithms for short-range molecular dynamics," *Journal of computational physics*, vol. 117, no. 1, pp. 1-19, 1995.

356 A. Mahata and M.A. Zaeem, "Effects of solidification defects on nanoscale mechanical properties of rapid directionally solidified Al-Cu Alloy: A large scale molecular dynamics study," *Journal of crystal growth*, vol. 527, no. pp. 125255, 2019.

357 A. Mahata, M. Asle Zaeem, and M.I. Baskes, "Understanding homogeneous nucleation in solidification of aluminum by molecular dynamics simulations," *Modelling and Simulation in Materials Science and Engineering*, vol. 26, no. 2, pp. 025007, 2018.

358 A. Mahata and M. Asle Zaeem, "Size effect in molecular dynamics simulation of nucleation process during solidification of pure metals: investigating modified embedded

atom method interatomic potentials," *Modelling and Simulation in Materials Science and Engineering*, vol. 27, no. 8, pp. 085015, 2019.

359 J. Eiken, B. Böttger, and I. Steinbach, "Multiphase-field approach for multicomponent alloys with extrapolation scheme for numerical application," *Physical Review E*, vol. 73, no. 6, pp. 066122, 2006.

360 E. Asadi, et al., "Quantitative modeling of the equilibration of two-phase solid-liquid Fe by atomistic simulations on diffusive time scales," *Physical Review B*, vol. 91, no. 2, pp. 024105, 2015.

361 J. Eiken, "Phase-field simulation of microstructure formation in technical magnesium alloys," *International journal of materials research*, vol. 101, no. 4, pp. 503-509, 2010.

362 B. Böttger, J. Eiken, and I. Steinbach, "Phase field simulation of equiaxed solidification in technical alloys," *Acta materialia*, vol. 54, no. 10, pp. 2697-2704, 2006.

363 M. Gündüz and J. Hunt, "The measurement of solid-liquid surface energies in the Al-Cu, Al-Si and Pb-Sn systems," *Acta Metallurgica*, vol. 33, no. 9, pp. 1651-1672, 1985.

364 V. Kokotin and U. Hecht, "Molecular dynamics simulations of Al–Al2Cu phase boundaries," *Computational materials science*, vol. 86, no. pp. 30-37, 2014.

365 J. Eiken. "Numerical solution of the phase-field equation with minimized discretization error," *in IOP Conference Series Materials Science and Engineering. 2012*.

366 A. Carré, B. Böttger, and M. Apel, "Implementation of an antitrapping current for a multicomponent multiphase-field ansatz," *Journal of crystal growth*, vol. 380, no. pp. 5-13, 2013.

367 M. Leitner, et al., "Thermophysical properties of liquid aluminum," *Metallurgical and Materials Transactions A*, vol. 48, no. 6, pp. 3036-3045, 2017.

368 S. Choi, H. Cho, and S. Kumai, "Effect of the precipitation of secondary phases on the thermal diffusivity and thermal conductivity of Al-4.5 Cu alloy," *Journal of alloys and compounds*, vol. 688, no. pp. 897-902, 2016.

369 J. Zhao, Y. Yuan, and F. Cui, "Relationship between the Cu content and thermal properties of Al–Cu alloys for latent heat energy storage," *Journal of Thermal Analysis and Calorimetry*, vol. 129, no. 1, pp. 109-115, 2017.

370 D. Du, H. Zhang, and D.J. Srolovitz, "Properties and determination of the interface stiffness," *Acta materialia*, vol. 55, no. 2, pp. 467-471, 2007.

371 https://micress.rwth-aachen.de/files/documentation/Vol2_Running_MICRESS.pdf.

372 A.S. Barros, et al., "Measurements of microhardness during transient horizontal directional solidification of Al-Rich Al-Cu alloys: Effect of thermal parameters, primary dendrite arm

spacing and Al 2 Cu intermetallic phase," *metals and materials international,* vol. 21, no. 3, pp. 429-439, 2015.

373 K. Young and D. Kerkwood, "The dendrite arm spacings of aluminum-copper alloys solidified under steady-state conditions," *Metallurgical Transactions A,* vol. 6, no. 1, pp. 197-205, 1975.

374 J. Sarreal and G. Abbaschian, "The effect of solidification rate on microsegregation," *Metallurgical Transactions A,* vol. 17, no. 11, pp. 2063-2073, 1986.

375 M. Gündüz and E. Çadırlı, "Directional solidification of aluminium–copper alloys," *Materials Science and Engineering: A,* vol. 327, no. 2, pp. 167-185, 2002.

376 E.S. Meza, et al., "The effect of the growth rate on microsegregation: Experimental investigation in hypoeutectic Al–Fe and Al–Cu alloys directionally solidified," *Journal of alloys and compounds,* vol. 561, no. pp. 193-200, 2013.

377 X. Lin, et al., "History-dependent selection of primary cellular/dendritic spacing during unidirectional solidification in aluminum alloys," *Acta materialia,* vol. 47, no. 11, pp. 3271-3280, 1999.

378 J. Kaneko, "Dendrite coarsening during solidification of hypo-and hyper-eutectic Al-Cu alloys," *Journal of materials science,* vol. 12, no. 7, pp. 1392-1400, 1977.

379 J. Hunt, "Solidification and casting of metals," *The Metal Society, London,* vol. 3, no., 1979.

380 W. Kurz and D. Fisher, "Dendrite growth at the limit of stability: tip radius and spacing," *Acta Metallurgica,* vol. 29, no. 1, pp. 11-20, 1981.

381 Y. Wang, et al., "Effect of cooling rates on the dendritic morphology transition of Mg–6Gd alloy by in situ X-ray radiography," *Journal of materials science & technology,* vol. 34, no. 7, pp. 1142-1148, 2018.

382 M. Amoorezaei, S. Gurevich, and N. Provatas, "Spacing characterization in Al–Cu alloys directionally solidified under transient growth conditions," *Acta materialia,* vol. 58, no. 18, pp. 6115-6124, 2010.

383 M.A. Tschopp, et al., "Characterizing the local primary dendrite arm spacing in directionally solidified dendritic microstructures," *Metallurgical and Materials Transactions A,* vol. 45, no. 1, pp. 426-437, 2014.

384 D. McCartney and J. Hunt, "Measurements of cell and primary dendrite arm spacings in directionally solidified aluminium alloys," *Acta Metallurgica,* vol. 29, no. 11, pp. 1851-1863, 1981.

385 J. Hunt and S.-Z. Lu, "Numerical modeling of cellular/dendritic array growth: spacing and structure predictions," *Metallurgical and Materials Transactions A,* vol. 27, no. 3, pp. 611-623, 1996.

386 V. Laxmanan, "Cellular and primary dendritic spacings in directionally solidified alloys," *Scripta materialia,* vol. 38, no. 8, pp. 1289-1297, 1998.

387 Q. Li and C. Beckermann, "Evolution of the sidebranch structure in free dendritic growth," *Acta materialia,* vol. 47, no. 8, pp. 2345-2356, 1999.

388 D. Eskin, et al., "Experimental study of structure formation in binary Al–Cu alloys at different cooling rates," *Materials Science and Engineering: A,* vol. 405, no. 1-2, pp. 1-10, 2005.

389 J.M. Quaresma, C.A. Santos, and A. Garcia, "Correlation between unsteady-state solidification conditions, dendrite spacings, and mechanical properties of Al-Cu alloys," *Metallurgical and Materials Transactions A,* vol. 31, no. 12, pp. 3167-3178, 2000.

390 D. Liu, et al., "Assessment of atomic mobilities of Al and Cu in fcc Al–Cu alloys," *Calphad,* vol. 33, no. 4, pp. 761-768, 2009.

391 W. Kurz and J. Fisher, "Fundamentals of Solidification, ed," *Trans Tech Publications Ltd., Uetikon-Zuerich, Switzerland,* vol. no., 1998.

392 D. Bouchard and J.S. Kirkaldy, "Prediction of dendrite arm spacings in unsteady-and steady-state heat flow of unidirectionally solidified binary alloys," *Metallurgical and Materials Transactions B,* vol. 28, no. 4, pp. 651-663, 1997.

393 V. Ronté and A. RoÓlSz, "The effect of cooling rate and composition on the secondary dendrite arm spacing during solidification. Part I: Al-Cu-Si alloys," *International Journal of cast metals research,* vol. 13, no. 6, pp. 337-342, 2001.

394 S. Sahoo and S. Ghosh, "Microstructure evolution of eutectic Al–Cu strips by high-speed twin-roll strip casting process," *Applied Physics A,* vol. 121, no. 1, pp. 45-50, 2015.

395 Q. Lei, J. Wang, and A. Misra, "Mechanical Behavior of Al–Al2Cu–Si and Al–Al2Cu Eutectic Alloys," *Crystals,* vol. 11, no. 2, pp. 194, 2021.

396 A.B. Michael and M.B. Bever, "Solidification of aluminum-rich aluminum-copper alloys," *JOM,* vol. 6, no. 1, pp. 47-56, 1954.

397 J.-L. Fattebert, M. Wickett, and P. Turchi, "Phase-field modeling of coring during solidification of Au–Ni alloy using quaternions and CALPHAD input," *Acta materialia,* vol. 62, no. pp. 89-104, 2014.

398 B. Utter, R. Ragnarsson, and E. Bodenschatz, "Alternating tip splitting in directional solidification," *Physical review letters,* vol. 86, no. 20, pp. 4604, 2001.

399 S.-C. Huang and M. Glicksman, "Overview 12: fundamentals of dendritic solidification—II development of sidebranch structure," *Acta Metallurgica*, vol. 29, no. 5, pp. 717-734, 1981.

400 E. Ben-Jacob, et al., "Formation of a dense branching morphology in interfacial growth," *Physical review letters*, vol. 57, no. 15, pp. 1903, 1986.